

Universidade do Minho
Escola de Ciências

Marcelo Silva Barreiro

Exciton generation by inelastic tunneling in heterostructures with two-dimensional semiconductors

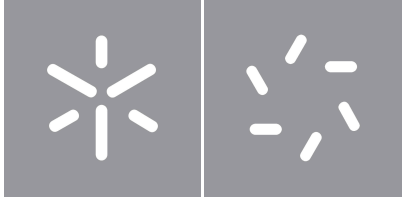
april 2024



Exciton generation by inelastic tunneling in heterostructures with two-dimensional semiconductors

Marcelo Silva Barreiro

UMinho | 2024



University of Minho
School of Sciences

Marcelo Silva Barreiro

Exciton generation by inelastic tunneling in heterostructures with two-dimensional semiconductors

Masters Dissertation
Physics

Dissertation supervised by
Doctor Bruno Amorim
Doctor Mikhail I. Vasilevskiy

april 2024

Copyright and Terms of Use for Third Party Work

This dissertation reports on academic work that can be used by third parties as long as the internationally accepted standards and good practices are respected concerning copyright and related rights.

This work can thereafter be used under the terms established in the license below.

Readers needing authorization conditions not provided for in the indicated licensing should contact the author through the RepositóriUM of the University of Minho.

License granted to users of this work:



CC BY-NC-SA

https://creativecommons.org/licenses/by-nc-sa/4.0/

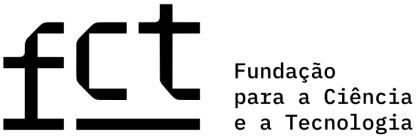
Agradecimentos

Em primeiro lugar, gostaria de agradecer aos meus orientadores, Professores Bruno Amorim e Mikhail Vasilevskiy, pela excelente orientação que me deram nesta tese. Foram de facto espetaculares, tanto a nível académico por demonstrarem ter um imenso conhecimento científico, pela paciência e afabilidade que tiveram para comigo, como também a nível pessoal pelo apoio e compreensão que tiveram em alturas menos boas deste percurso. São professores como estes que me motivam a querer seguir um percurso tão adverso mas tão estimulante como o da física teórica. Agradeço também à Universidade do Minho, em particular ao Departamento de Física e aos professores que a personificam, pelo apoio institucional e académico que me deram ao longo destes anos.

De seguida, quero mencionar a minha gratidão para com os meus colegas de curso, especialmente aos meus amigos Tiago Antão e Francisco Lobo, por todas as frutíferas discussões e pelos bons momentos que partilhamos, mas também por estarem presentes nos maus momentos.

Gostaria também de agradecer à minha família pelo apoio que me deu ao longo destes anos, em especial aos meus pais e aos meus padrinhos. Aos meus padrinhos, por me terem ajudado inúmeras vezes e por no fundo terem sido os meus segundos pais. Ao meu pai, por tudo aquilo que me ensinou ao longo da vida e por me ter mostrado como ser resiliente mesmo quando tudo parece perdido. À minha mãe por ter sido o meu porto de abrigo em todos os momentos da minha vida. Sem ela, eu nunca estaria onde estou hoje.

Este trabalho foi financiado por fundos nacionais através da FCT – Fundação para a Ciência e a Tecnologia, I.P., no âmbito do projeto EXPL/FIS-MAC/0953/2021.





Statement of Integrity

I hereby declare having conducted this academic work with integrity.

I confirm that I have not used plagiarism or any form of undue use of information or falsification of results along the process leading to its elaboration.

I further declare that I have fully acknowledged the Code of Ethical Conduct of the University of Minho.

University of Minho, Braga, may 2024

Marcelo Silva Barreiro

Exciton generation by inelastic tunneling in heterostructures with two-dimensional semiconductors

Abstract

In this thesis, we study the emission of excitons via inelastic tunneling in mesoscopic devices with two electrodes separated by a non-conductive material, subjected to a biased electrostatic potential. We study this problem applying both a simplified toy model and a detailed model for a graphene/hexagonal boron nitride/graphene (gr-hBN-gr) van der Waals (vdW) heterostructure. Specifically, we focus on the corrections to the current arising from the interaction between the tunneling electrons and the two-dimensional excitons hosted by a transition metal dichalcogenide (TMD) layer placed a few nanometers apart.

To this end, we start by applying the non-equilibrium Green's function (NEGF) technique to a generalized transport problem for a two-contact mesoscopic system with general electron-boson interactions, thus obtaining analytic expressions for the non-interacting elastic current - the Landauer formula - written as the energy integral of the contact's occupied levels and the transmission function, which is related to the probability of an electron with a given energy to tunnel through the device. Treating the electron-boson interaction as a perturbation, we also obtain the second order corrections that these interactions introduce, separating the cases of elastic and inelastic processes.

In order to gain insight about the general features that arise in the electron tunneling problem, we apply these generic results to a one-dimensional toy-model at zero temperature and calculate both the transmission functions and the I-V curves for this idealized system. Although simple in its nature, it is sufficient to capture the phenomena of inelastic tunneling assisted by the emission of a bosonic excitation. As such, it captures some of the essential features of the more complex vdW device. We are able to show that, when accounting for interactions up to the second order, there is an increase in the total current for bias voltages in resonance with the model sample, while for voltages exceeding this threshold there is a suppression in the total current dominated by the elastic correction, even though its inelastic counterpart contributes with a small increase. Additionally, we also show that these interactions open new tunneling channels that depend on boson's energy.

Finally, we tackle the problem of finding the exciton-assisted inelastic tunneling current flowing in the vdW heterostructure, electromagnetically coupled to the excitonic layer (TMD). To do so, we calculate the matrix element for the electron-exciton interaction, mediated by the emission and absorption of virtual

photons, in a second order perturbation theory and use it to obtain the transition rate from Fermi's golden rule, from which we are able to find the inelastic current flowing through the system and the corresponding rate of generation of excitons in the TMD layer.

Keywords: non-equilibrium Green's functions, inelastic tunneling, excitons, van der Waals heterostructures, electroluminescence.

Geração de excitões por tunelamento inelástico em heteroestruturas com semicondutores bi-dimensionais

Resumo

Nesta tese, estudamos a emissão de excitões por tunelamento inelástico em dispositivos mesoscópicos com dois eletrodos separados por um material isolador, sujeito a um potencial eletrostático. Abordamos este problema aplicando tanto um modelo simplificado e um modelo detalhado para uma heteroestrutura de van der Waals de grafeno/nitreto de boro hexagonal/grafeno. Em especial, focamo-nos nas correções à corrente que advém de interações entre os eletrões em tunelamento e os excitões bi-dimensionais presentes numa camada de um dicalcogeneto de metais de transição colocada a uma distância de alguns nanómetros.

Para tal, começamos por aplicar a técnica de funções de Green fora de equilíbrio a um problema de transporte genérico num sistema mesoscópico de dois contactos com interações eletrão-bosão genéricas, obtendo assim expressões analíticas para a corrente elástica não interatuante - a fórmula de Landauer - escrita como o integral de energia dos níveis de ocupação dos contactos e a função de transmissão, que está relacionada com a probabilidade de um eletrão com uma dada energia transitar através do dispositivo. Tratando a interação eletrão-bosão como uma perturbação, também obtemos as correções de segunda ordem que essas interações introduzem, separando os casos de processos elásticos e inelásticos.

De modo a ganhar experiência sobre as características gerais de problemas de tunelamento de eletrões, aplicamos estes resultados genéricos a um modelo uni-dimensional simplificado a temperatura zero e calculamos tanto as funções de transmissão como as curvas I-V para este sistema idealizado. Embora de natureza simplista, é suficiente para capturar os fenómenos de tunelamento inelástico assistido pela emissão de uma excitação bosónica. Como tal, este captura algumas das características essenciais de dispositivos vdW mais complexos. Mostramos que, tendo em conta interações até segunda ordem, se verifica um aumento da corrente total para voltagens em ressonância com a amostra do dispositivo, enquanto que para voltagens superiores a este limite há uma diminuição da corrente total dominada pela correção elástica, apesar da correção inelástica contribuir para um ligeiro aumento. Além disso, também mostramos que estas interações abrem novos canais de tunelamento que dependem da energia do bosão.

Por último, abordamos o problema de obter a corrente que flui na heteroestrutura de vdW por tu-

nelamento inelástico assistido por excitões, acoplada eletromagneticamente aos excitões da camada de TMD. Para isso, calculamos o elemento de matriz para a interação eletrão-excitão, mediada pela emissão e absorção de fotões virtuais, em teoria de perturbações de segunda ordem e usamos-o para obter a taxa de transição a partir da regra de ouro de Fermi, através da qual se obtém a corrente inelástica que flui no sistema e a correspondente taxa de geração de excitões na camada de TMD.

Palavras-chave: Funções de Green fora do equilíbrio, tunelamento inelástico, excitões. heteroestruturas de van der Waals, eletroluminescência.

Contents

1 Introduction **1**

1.1 Novel nearly 2D materials for optoelectronics and photonics . . . 1

1.2 Scope and objectives of this work . . . 4

1.3 Structure of this thesis . . . 8

2 NEGF formalism for mesoscopic transport **10**

2.1 Description of the problem and setup . . . 10

2.2 Equation of motion for the current operator . . . 13

2.3 Integrating out the contacts . . . 15

2.4 Current in the stationary limit . . . 17

2.5 Non-interacting case: the Landauer formula . . . 19

2.6 Elastic and inelastic current in the presence of interactions . . . 20

2.6.1 Electron-boson interaction . . . 22

2.6.2 Elastic current up to second order in M_λ . . . 23

2.6.3 Inelastic current up to second order in M_λ . . . 26

3 Application to an one-dimensional toy-model **30**

3.1 Introduction to the model . . . 30

3.1.1 The 1D model Hamiltonian . . . 30

3.1.2 Green's function for the leads . . . 33

3.1.3 Level width functions . . . 38

3.1.4 Central region's Green's Function . . . 38

3.2 Lowest order elastic transport (without perturbation) . . . 39

3.2.1 Elastic transmission function $\mathcal{T}_{\text{el}}^{(0)}$ . . . 40

3.2.2 Elastic current $J_{\text{el}}^{(0)}$ . . . 41

3.3 Second order correction to the elastic transport . . . 44

3.3.1 Correction to the elastic transmission function $\mathcal{T}_{\text{el}}^{(2)}$ . . . 44
3.3.2 Correction to the elastic current $J_{\text{el}}^{(2)}$ . . . 49
3.4 Inelastic transport up to second order in M_λ . . . 51
3.4.1 Inelastic transmission function $\mathcal{T}_{\text{inel}}^{(2)}$ . . . 51
3.4.2 Lowest order inelastic current $J_{\text{inel}}^{(2)}$ . . . 53
3.5 Discussion . . . 60

4 Second-order perturbation theory for the 3D device 65
4.1 Microscopic processes and Hamiltonians . . . 65
4.1.1 Preliminary remarks . . . 65
4.1.2 Electron-photon interaction Hamiltonian $H_{\text{e-ph}}$ . . . 67
4.1.3 Exciton-photon interaction Hamiltonian $H_{\text{ph-ex}}$ . . . 68
4.1.4 Description of the states . . . 69
4.2 Calculation of the second-order matrix element $M_{i\to f}$ . . . 71
4.2.1 Direct process, M_1 . . . 71
4.2.2 Inverse process, M_2 . . . 75
4.2.3 Total matrix element M_{if} . . . 75
4.2.4 Integration in q_z . . . 77
4.3 Fermi's Golden Rule and inelastic current . . . 79

5 Conclusion and Outlook 81

Appendices 100

A Brief introduction to non-equilibrium Green's functions 101
A.1 Time dependent perturbation theory and contour ordering . . . 101
A.2 Contour ordered Green's functions . . . 104
A.3 Langreth's rules . . . 108
A.4 Fock diagram for the electron-boson interaction . . . 109

B Electronic wave-function in graphene 113
B.1 In-plane wave-function . . . 114
B.2 Out-of-plane wave-function . . . 116

Chapter 1

Introduction

1.1 Novel nearly 2D materials for optoelectronics and photonics

In the past century, the human species have witnessed huge advancements in the creation and development of electronic technologies. These technologies completely changed the way that humans communicate with each other, access information, work, travel and socially interact, having profound impacts world-wide in virtually every aspect of human society.

In 1965, Gordon Moore [1] has predicted that every two years the number of components in each integrated circuit would double. This prediction of exponential growth turned out to be true and since 1975 it has been regarded as a "law". However, nowadays there is some debate wether Moore's law is still valid or not [2, 3]. With the increase in shrinking of electronic components, modern day technology have reached such a miniaturization scale that the laws of classical physics no longer suffice, being imperative to take into account effects stemming from quantum mechanics [4]. With technological research increasingly turning to the quantum world, new forms of electronic devices were proposed where quantum effects are harnessed. These devices include quantum dots [5, 6], quantum cascade lasers [7], single-electron transistors [8], superconducting quantum interference devices [9], quantum computing devices [10], spintronic devices [11], among others.

In more recent years, a new potential basis for the development of these devices has emerged in the form of the so called van der Waals (vdW) heterostructures [12, 13, 14], which basically consist on stacks of multiple nearly 2D materials of equal or different type, held together by van der Waals forces (hence the name of these structures) in order to harness the properties of all constituent materials. Typical materials used in vdW heterostructures are graphene, hexagonal Boron-Nitride (hBN) and transition metal dichalcogenides (TMDs), among many others [15].

Graphene was the first 2D atomic crystal to be experimentally obtained [16] and paved the way for the world of 2D materials (with thickness of one atom) to be explored, which lead to the 2010 Nobel Prize in Physics being awarded "for groundbreaking experiments regarding the two-dimensional material graphene" [17]. Since this discovery, a huge amount of research was devoted to characterize graphene, develop fabrication techniques and applications, both theoretic and experimentally [18]. Graphene is composed of carbon atoms arranged in a hexagonal honeycomb lattice and is known for exhibiting uniquely combined features [19] such as extreme mechanical strength, elasticity and flexibility [20, 21, 22], high electronic [23, 24, 25, 26, 27] and thermal [28, 29, 30, 31, 32, 33] conductivities, chemical stability [34, 21, 20] and unique optical properties such as transparency to radiation in the visible spectrum [35, 36, 37, 38], anomalous optical absorption [39, 40, 41, 42] and strong light-matter interactions [43, 44, 45, 46, 47]. These properties make graphene an excellent candidate to be used in vdW heterostructures [48, 49, 50, 51, 52], typically playing the role of electric contact. However, the properties of graphene can be negatively affected if the wrong substrate is used [53, 54]. This problem can be overcome by using hBN since that, with this particular substrate, the properties of graphene were shown to be enhanced [49, 26, 55, 50].

Hexagonal Boron-Nitride (hBN), also known as "white graphene" due to their structural similarity, is an insulating isomorph of graphene that instead of carbon atoms is composed of boron and nitrogen atoms also arranged in a honeycomb lattice, with a 1.8% lattice mismatch with respect to graphene [49]. While being an insulator with a large band-gap [56, 57], hBN is frequently combined with graphene in vdW devices [58] due to its atomically planar surfaces, mechanical robustness, thermal stability and being relatively inert, thus acting as a very good substrate [48, 38, 55, 59, 60] and also as a shield from environmental degradation. It can also be used as a tunneling barrier since it can be fabricated as thin as a single monolayer [61, 60, 55, 62, 26]; as a decoupling layer for graphene due to its reduced substrate induced strain, thus preserving its electronic properties [63]; it can be used to enhance the already formidable optical properties of graphene [64, 65, 66, 67, 68]; one can also engineer a moiré superlattice formed between these two materials, thus introducing a periodic modulation in the electronic density of states that can be used to form additional electronic states and electron correlation phenomena, or even to create and tune a band gap in graphene [69, 49, 70, 71, 62].

Other 2D materials that are also the focus of much investigation are semiconducting transition metal dichalcogenides [72]. These are semiconductors of the type MX_2, where M stands for transition metal (typically of 4-7 group of the periodic table) and X for chalcogenide (group 16 of the periodic table, although the nomenclature typically does not include oxides). Some of the most commonly studied semiconducting

TMDs are MoS_2, $MoSe_2$, WS_2 and WSe_2 [73, 74, 75]. TMDs can exist in either bulk or monolayer form [76, 77] and their electronic, optical and mechanical properties differ considerably between the two forms. Since bulk TMDs have strong covalent intralayer bounds and weak vdW interlayer bounds, it becomes relatively easy to synthesize monolayer TMDs from their bulk counterparts by means of several exfoliation or vapor deposition techniques [78, 79, 80]. One of the most striking differences when comparing bulk and monolayer TMDs is the fact that, even though in bulk they feature indirect bandgaps, TMDs in monolayer form have a direct electronic bandgap [81, 82, 83] that makes photo-induced electronic transitions feasible [84, 85]. This leads to strong absorption and photoluminescence properties [86, 87, 88], some of them in the visible spectrum, making monolayer TMDs excellent candidates for optoelectronic applications [89, 90, 91].

The enhancement of the photoluminescence properties in monolayer TMDs is mainly caused by excitons [92, 93], a bosonic quasiparticle composed by an electron that is excited from the valence band and the positively charged hole (vacancy) that it left in the valence band, bound together via Coulomb interactions [94, 95]. Excitons are not exclusive of TMDs, they are common quasi-particles that are formed in gapped materials (insulators and semiconductors), both in bulk or monolayer form. However, the fact that monolayer TMDs have reduced dielectric screening (due to the low dimensionality) means that excitons in these materials have enhanced binding energies and small radius, leading to a lot of attention being drawn to them [96, 97, 98]. The two body system that the bond state between the electron and the hole forms can be regarded as an analog of the hydrogen atom with a smaller effective mass [99, 100]. The excitonic bound energy states are also analogous to the hydrogen atom and lie inside the bandgap of the material, highly affecting the optical properties of the material [101, 102, 103]. For example, we can promote a direct electronic transition by using photons (making use of the monolayer's direct bandgap), where the excited electron interacts with the hole left behind and decays to a bound state inside the gap, thus forming an exciton that later recombines by emitting a photon with a different frequency than the initial photon, thus creating a process that can be used in a range of different photonic and optoelectronic applications [104, 105].

In addition to the direct bandgap and excitonic effects, an enhanced spin-orbit coupling arises in monolayer TMDs [106, 107] due to the strong electron confinement in one direction and the presence of heavy atoms (the M atoms), leading to spin-orbit splitting of hundreds of meV in the valence band [108]. This splitting can be harnessed in spintronic applications, along with the fact that monolayer TMDs have no inversion center, which provides the electrons with an extra degree of freedom - the valley index - that can be used in many applications falling under the new field of valleytronics [109, 110]. This spin-orbit

splitting originates two series of excitons [111] - A and B - that differ in the position of the hole in the two branches - up or down, respectively - of the valence band. Such discrepancy can be distinguished in photoluminescence and reflectivity measurements using circularly polarized light [112, 113] because the excitons of each series have different optical gaps (difference between the electronic gap and the exciton's binding energy) and spins.

1.2 Scope and objectives of this work

This thesis is devoted to some theoretical aspects of the usage of the novel nearly 2D materials in optoelectronic devices, in particular, those capable of generation of light by electric currents, based on the phenomenon of electroluminescence.

Now that the individual components of the system to be considered in this thesis have been introduced, we present in Fig. 1 the specific vdW heterostructure that we are interested in. This consists in two

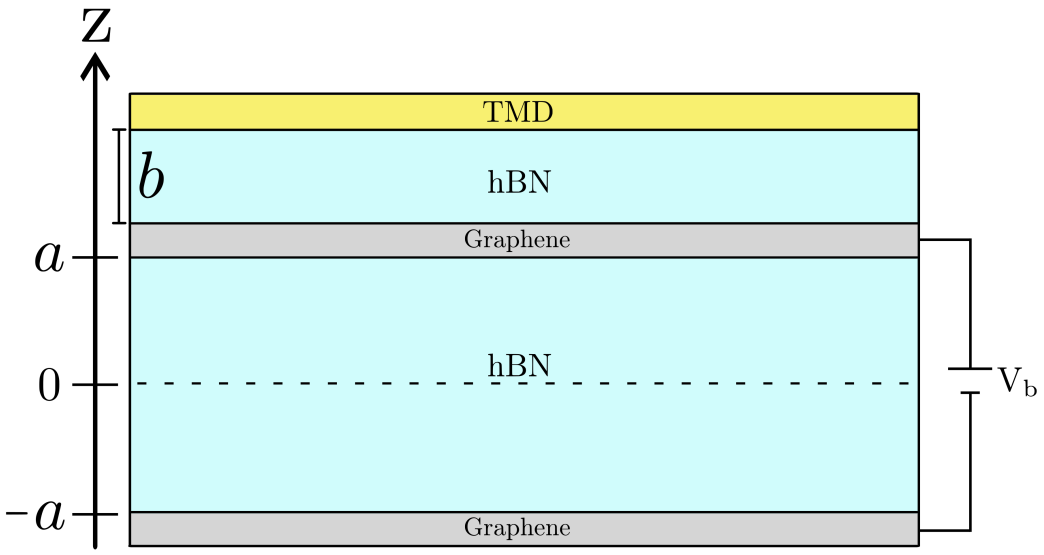


Figure 1: Scheme of the device in study. It is composed by two graphene sheets (gray) acting as electric contacts, separated by a dielectric spacer (blue) of thickness $2a$ (typically in the order of a few nanometers) composed by $\mathcal{N}$ layers of hBN. The origin of the z axis is set at the geometric center of this hBN slab. At $z = a + b$ is placed a single layer of a 2D TMD (yellow), separated from the top graphene layer by an additional hBN spacer (smaller blue rectangle) of thickness b. A bias voltage V_b is applied between the graphene sheets so that the hBN slab in-between acts as a tunneling barrier for the flow of electrons from one graphene to the other.

graphene sheets separated from each other by a slab of hBN with $\mathcal{N}$ layers, with a bias voltage applied across the structure. Additionally, on top of one of the graphene sheets is also a TMD monolayer. The graphene/hexagonal Boron Nitride/graphene (gr-hBN-gr) heterostructure has been widely studied [114, 115, 116, 117, 118] due to the unique features that the combination of the two materials show, with the reason for this being the lattice matching [49], mechanical stability [119], reduced dimensionality, weak vdW bonding between layers, enhancement of graphene's properties [120, 121], tunable graphene's gap [122] and spin-orbit coupling, to mention some, which in practice offers a wide range of potential applications [123, 124, 125, 126, 127].

For our purposes, we regard this heterostructure as a tunneling device, where the graphene sheets serve as electrical contacts (making use of its high carrier mobility) and the hBN as the tunneling barrier (since it has a large gap around 6eV). It has been shown that the tunneling currents flowing through this device highly depend on the thickness of the tunneling barrier [114, 128], which is relatively easy to manipulate up to the atomic scale (few nanometers) by controlling the number of layers $\mathcal{N}$ of the hBN slab. We are particularly interested in the introduction of a TMD into the system, specifically with the fact that it is a host for excitons that are accessible with light and can be detected even at room temperature [96]. The potential presence of these quasiparticles in the system, although not directly within the tunneling path of the electron, can induce the opening of inelastic tunneling channels via electron-exciton interactions, and even open possible new channels for the elastic current that already flows in the gr-hBN-gr system without the TMD [128]. This effect is depicted in Fig. 2, reproduced from Ref. [129], where although one of the contacts of the tunneling junction is made of gold instead of graphene, the change in the tunneling current by the introduction of the a TMD layer is clearly seen by the presence of a peak in the I-V curve, resonant with the exciton's energy, that is otherwise absent in the I-V curve for the tunneling junction alone. By harnessing the process of exciton recombination in the TMD, which are created by the tunneling electrons, electrically pumped light sources and eventually single-photon emitters are possible applications of this device. Additionally, we remark that the phonon assisted inelastic current in resonant tunneling devices has been also widely studied [130, 131, 132] and even phonon assisted tunneling in gr-hBN-gr has been observed [118], providing a solid foundation for the study of exciton assisted tunneling in the gr-hBN-gr+TMD device. Additionally, the study of direct photon emission in related devices is addressed in Ref. [133]. Therefore, we aim to theoretically describe the influence that electron-exciton interaction has in the tunneling current, which was already experimentally measured by Wang *et al.* [129] in the I-V characteristic curves and Pommier *et al.* [93] by means of electroluminescence measurements.

The phenomenon of electroluminescence consists in the emission of light by a system to which is being

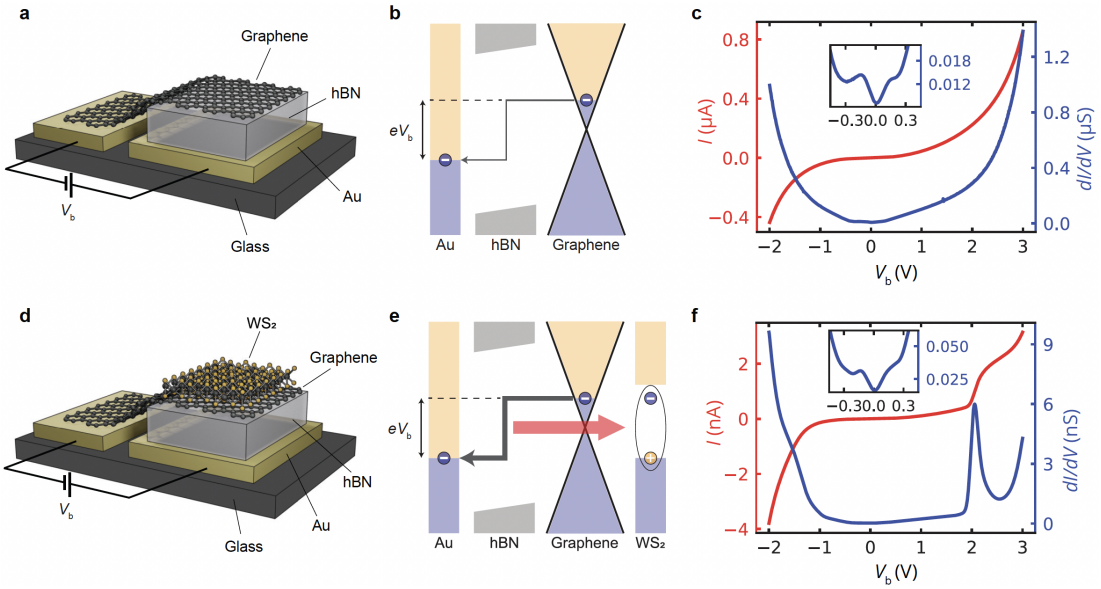


Figure 2: Reproduced from Ref. [129]. **Device schematics, band diagrams, and I–V characteristics. a)** Illustration of a graphene/hBN/Au tunneling device. The device is protected by a top hBN layer (not shown for better visibility). A bias voltage V_b applied between the graphene and gold electrodes gives rise to a tunneling current through the hBN spacer. **b)** Band diagram of the device for positive V_b. Electrons tunnel from graphene to Au both elastically (not shown) and inelastically (kinked arrow). **c)** Recorded I–V (red) and dI/dV (blue) curves at room temperature from the device in a). No distinctive features are observed besides an overall asymmetry due to the electronic DOS in Au. Inset: Zoom into the low-bias region displaying phonon-assisted resonances. **d)** Illustration of a WS_2/graphene/hBN/Au tunnel device, including a protecting top hBN layer (not shown). **e)** Band diagram of the device at a positive bias. Electron tunneling can be mediated by the creation of excitons (encircled electron-hole pair) in WS_2, as indicated by the red arrow. **f)** Recorded I–V (red) and dI/dV (blue) curves at room temperature from the device in d. A new feature appears near $V_\mathrm{b} = 2.05V$. Inset: Zoom into the low-bias region displaying phonon-assisted resonances.

applied a voltage, which has many optoelectronic applications such as light emitting devices [134, 135, 136]. This process can be enabled from several underlying mechanisms, but the one that we are interested in is when it is mediated by excitons [137, 104]. The idea is that the electrons that participate in the flow of current through the system (tunneling device) undergoes an inelastic transition (in the tunneling process) and loses energy by emission of a resonant exciton (this can be achieved by direct impact excitation [138], Joule heating [139], carrier injection [140], and others[141, 123]). In turn, the exciton has a finite lifetime [142, 143] after which the electron and the hole recombine by emitting a photon [144, 145]. Thus, in practice what is experimentally verified is that for voltages higher than a specific threshold the device emits light with a narrow bandwidth and a specific wavelength [89, 90] (matching the exciton's energy), that can be controlled by, e.g., changing the excitonic host material (the TMD). The intensity of the emitted radiation is correlated with the intensity of the current (the more electrons decay, the more excitons are formed and thus more photons are emitted from their recombination).

In order to tackle this inherently complicated and inhomogeneous structure with an out-of-equilibrium character, we employ the so called Non-Equilibrium Green's Functions (NEGF) formalism (which is explained in more detail in Appendix A). Developed independently by Keldysh [146] and by Kadanoff and Baym [147] in the 1960's, it is a powerful technique that extends way outside of the limited applicability of Matsubara's formalism of imaginary time Green's functions or even linear response theory. Based on the idea of propagating the Green's functions over a time contour, it offers a systematic way of describing the dynamics of many-body systems far from equilibrium and to develop a perturbation approach to out-of-equilibrium systems. With this technique, one needs only to provide the Hamiltonian as an input, with which the Green's functions and the self-energies can be calculated, and from the formalism itself one can obtain all relevant quantities. This technique was already used in similar problems of inelastic tunneling assisted by phonons [130], where it proved to be a robust tool to study this type of phenomena.

Ideally, the objective of this thesis would be to use the NEGF formalism to describe the tunneling current flowing through the system depicted in Fig. 1 and the way that the excitons generated in the TMD influence this phenomena. In order to gain intuition regarding the role of exciton emission in the phenomena of tunneling currents, we considered first a one-dimensional toy model composed by two semi-infinite tight-binding chain of atoms connected to a single-level (that can be seen as an impurity of the otherwise infinite chain or a quantum dot) and subjected to a bias voltage. Additionally, in order to model the presence of the excitons in the TMD, we set the central region to be connected to a thermal bath of generic bosons. Such a toy-model is widely used in pedagogical introductions to the field of mesoscopic physics [148], and although very simple in its nature, it still captures the essential physics behind many

real systems. Even though we do not hope to obtain exact predictions with this model, we are interested to see how far it goes in qualitatively capturing major features that real mesoscopic devices such as the one in Fig. 1 display.

In the second part of the thesis, a more detailed model of the device of Fig. 1 is considered, with two graphene electrodes treated explicitly (within the Dirac cone approximation), as well as the TMD exciton considered within a 2D hydrogenic model. The interaction between the tunneling electron and exciton is described by quantum electrodynamics taking into account emission and absorption of virtual photons. We limit ourselves by calculating the probability of tunneling (assisted by the creation of an exciton) per unit time by employing Fermi's Golden Rule. This probability is directly related to the tunneling current density and the generation rate of TMD excitons.

1.3 Structure of this thesis

The thesis is organized as follows:

- In Chapter 2 we develop the NEGF formalism with a generic two-contact system driven out of equilibrium by a bias voltage. We start from the equation of motion for the current flowing in through the central region, where we arrive to an expression containing Green's functions for operators of different regions. In order to obtain the current from the point of view of the central region, we integrate out the contacts by expressing all contact related quantities as a contact induced self-energy. This way, we end up with an expression containing the Green's functions for the central region and the self-energies that arise due to its coupling with the leads. By neglecting transient dynamics, we focus in the stationary behavior, thus being able to express the current as an integral over energy of the central region's Green's functions and the contact's self-energies. Then we proceed by deriving a formula for the case when the central region is non-interacting - the Landauer formula - and we end the chapter by analyzing the case when we allow for interactions in the central region, treating them as a perturbation and thus obtaining an elastic and an inelastic correction for the current up to the second order in the electron-boson interaction.

- In Chapter 3 we use the results that we obtained in the previous chapter and apply them to the 1D toy-model. We start by introducing the model and the relevant quantities, such as the Green's functions for either the leads and the central region, and also the level-width function (related with the coupling between the contacts and the central region). With these quantities we are then able to calculate the transmission functions, which are related to the probability of an electron with a given

energy to cross the device, having obtained expressions when we neglect interactions and also for elastic and inelastic corrections up to second order in the interaction. We end the chapter by calculating the corresponding currents and interpret the results in light of what would be expected in real mesoscopic devices. We remark that in order to better compare our results with the literature, we need to find a suitable expression for the interaction matrix element since it is responsible for providing us with the magnitude of the effect of enabling interactions into the system. This is the topic of Chapter 4.

- In Chapter 4 we tackle the problem of finding an expression for the electron-exciton interaction matrix element by resorting to second order perturbation theory, so that we treat this interaction as a two step process (i) interaction between the electron with a virtual photon and (ii) between the virtual photon and an exciton, or *vice versa*. We start by stating the Hamiltonians responsible for these interactions, and then we use the standard expression for the interacting matrix element in second order perturbation theory, so that we obtain an explicit expression for this quantity. With this, we are able to calculate the probability of the electron to tunnel inelastically, assisted by the exciton, by using Fermi's Golden Rule.

- In Chapter 5 we conclude our study and mention our plans for future work.

Chapter 2

NEGF formalism for mesoscopic transport

In this chapter, we aim to apply the formalism of non-equilibrium Green's functions (NEGF) to mesoscopic systems that are driven out of equilibrium by a potential bias.

This derivation was based on Refs. [148, 149, 150, 151].

A good review on NEGF can be found in Refs. [152, 153, 154].

A more formal and deep book about non-equilibrium Green's functions is Ref. [155].

2.1 Description of the problem and setup

Consider a generic two-terminal device composed by a central region (C), which might support interactions (we consider this case in the final section of this chapter), and two metallic terminals, left (L) and right (R), which are assumed to be non-interacting.

As far as we are concerned, these terminals are disconnected from the central region for times $t < t_0$, where t_0 is the instant when the terminals are connected to the system, as shown in Fig. 3.

The contacts are subjected to a voltage difference V_b, which creates a potential imbalance $\mu_L - \mu_R$ between them. Once the terminals are connected to the central region at $t = t_0$, the potential imbalance

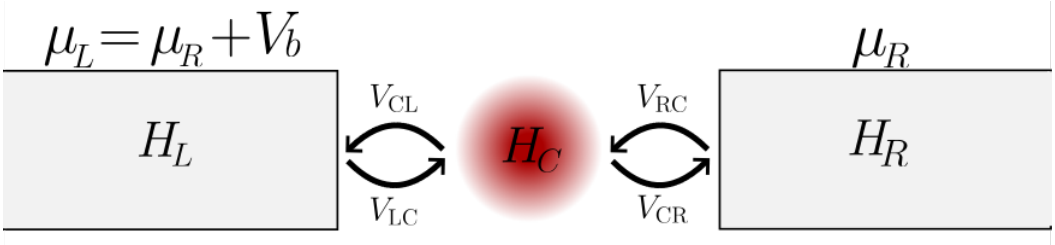


Figure 3: Scheme for a generic two-contact system. Two non-interacting contacts (L/R) are coupled to a central region (C) via the coupling terms $\boldsymbol{V}_{\ell C}/\boldsymbol{V}_{C\ell}$. A potential bias V_b is placed across the device, driving it out of equilibrium by altering the chemical potentials of the contacts such that $\mu_L = \mu_R + V_b$.

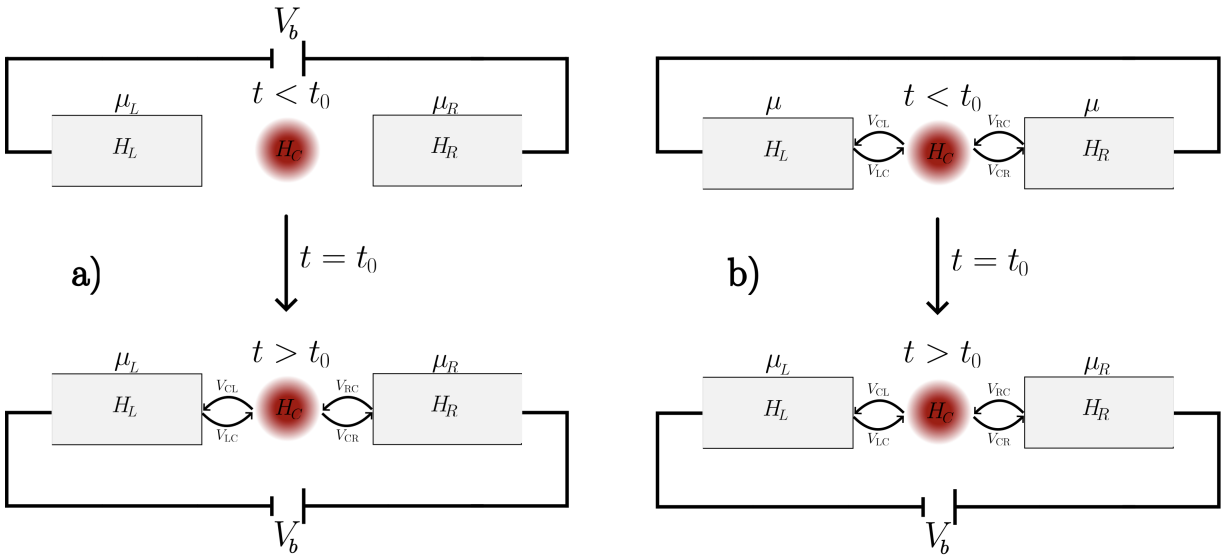


Figure 4: Scheme for the **a)** partition setup and the **b)** partition-free setup.

For the partition setup case in **a)** the contacts (L/R) have different chemical potentials μ_L and μ_R, being disconnected from the central region (C) for times $t < t_0$. Both the contacts and the central region are in local thermal equilibrium, that being, each individual component is in equilibrium within themselves. At $t = t_0$ the contacts are connected to the central region, driving the system out of equilibrium.

For the partition-free setup case in **b)** the contacts are connected to the central region at all times, so that for $t < t_0$ the whole system is in equilibrium, since there is no chemical potential imbalance ($\mu_L = \mu_R = \mu$). In contrast with the previous scenario where the terminals were put in contact with the central region, at $t = t_0$ the terminals are already coupled but what changes is that a potential bias is switched on, altering the chemical potentials of the contacts, thus driving the system out of equilibrium.

originates a current flowing through the system. We also assume that before the contacts were coupled to the central region, each part of this device was in a local thermodynamic equilibrium.

The assumption that the terminals were disconnected from the device and kept at different potentials for $t < t_0$ is called the *partitioned setup*, which is represented in Fig. 4**a)**.

Another possibility would be the *partion-free setup* (see e.g. Ref. [150]) illustrated in Fig. 4**b)**, in which the terminals and the central system are coupled and in equilibrium in the beginning. Then, at $t = t_0$, a voltage is applied across the contacts driving the system out of equilibrium, resulting into the flow of a current through the device. The difference between these two approaches lies in the transient regime, but, in the asymptotic stationary state in which we are interested in, they agree with each other [150].

With this being said, before we start with the application of the NEGF formalism for a generic two-

contact system, it is essential that we make a few comments about the notation employed throughout the text.

Although in Chapter 3 we reduce the complexity of the formalism by applying it to a 1D toy model, in this chapter we derive all results generally by not taking into account the dimensionality of the device (which is implicit in the quantities that we keep unspecified). In this way, we already have the formalism in the right notation if we actually apply it to the physical 3D system, as it is our intention for future works.

The total Hamiltonian for this system is simply given by

$$\boldsymbol{H} = \boldsymbol{H}_L + \boldsymbol{H}_C + \boldsymbol{H}_R + \sum_{\ell=L,R} (\boldsymbol{H}_{C\ell} + \boldsymbol{H}_{\ell C}) \tag{2.1}$$

where $\boldsymbol{H}_x$ with $x = L, C, R$ is the non-interacting Hamiltonian for the x region and $\boldsymbol{H}_{C\ell}/\boldsymbol{H}_{\ell C}$ is the interacting Hamiltonian between the lead ℓ and the central region C, with $H_{\ell C} = H_{C\ell}^{\dagger}$.

We write the generic Hamiltonian for any component of this system as

$$\boldsymbol{H}_x = \sum_{\alpha\beta} H_x^{\alpha\beta} c_\alpha^{x\dagger} c_\beta^x$$

where the label $x = L, C, R$ defines the region being described by $H_x^{\alpha\beta}$, where $\alpha,\ \beta$ are the state labels of the subsystem x and c^x $\left(c^{x\dagger}\right)$ is the electronic annhilation (creation) operator for the region x, which obey the following fermionic anti-commutations relations

$$\left\{c_\alpha^{x\dagger}, c_\beta^{y\dagger}\right\} = 0 \tag{2.2}$$

$$\left\{c_\alpha^{x}, c_\beta^{y}\right\} = 0 \tag{2.3}$$

$$\left\{c_\alpha^{x\dagger}, c_\beta^{y}\right\} = \delta_{\alpha,\beta}\delta_{x,y} \tag{2.4}$$

The Hamiltonian describing the hopping of electrons from the central region to the contact $\ell = L, R$, which is switched on at the time $t = t_0$, is given by

$$\boldsymbol{H}_{C\ell} = \sum_{\alpha\beta} V_{C\ell}^{\alpha\beta} c_\alpha^{C\dagger} c_\beta^{\ell} \tag{2.5}$$

with $V_{\ell C}^{\beta\alpha} = \left[V_{C\ell}^{\alpha\beta}\right]^{\dagger}$.

We also remark that the Hamiltonian H_C for the central region might include interactions, which will be the topic of discussion in section 2.6.

2.2 Equation of motion for the current operator

The current flowing from the ℓ contact to the central region is measured by the rate that the number of electrons in the ℓ contact changes over time, which is formulated as

$$I_{\ell \to C} = -q_e \frac{d\boldsymbol{N}_\ell}{dt} \tag{2.6}$$

where $\boldsymbol{N}_\ell$ is the electron number operator for the ℓ contact, defined as

$$\boldsymbol{N}_\ell = \sum_\beta c_\beta^{\ell\dagger} c_\beta^\ell \tag{2.7}$$

and q_e is the electron's charge.

The time derivative of $\boldsymbol{N}_\ell$ can be evaluated through the operator's equation of motion method, so that we start with Heisenberg's equation

$$\frac{d\boldsymbol{N}_\ell}{dt} = \frac{i}{\hbar} [\boldsymbol{H}, \boldsymbol{N}_\ell] \tag{2.8}$$

where the total Hamiltonian $\boldsymbol{H}$ is given by Eq. 2.1.

Since $[H_m, N_\ell] = 0$ with $m \neq \ell$, this last expression can be simplified by including only the Hamiltonians present in Eq. 2.1 that are related to the ℓ region, so that we have

$$\begin{aligned} \frac{d\boldsymbol{N}_\ell}{dt} &= \frac{i}{\hbar} [\boldsymbol{H}, \boldsymbol{N}_\ell] \\ &= \frac{i}{\hbar} \left([\boldsymbol{H}_\ell, \boldsymbol{N}_\ell] + [\boldsymbol{H}_{C\ell}, \boldsymbol{N}_\ell] + [\boldsymbol{H}_{\ell C}, \boldsymbol{N}_\ell] \right) \end{aligned} \tag{2.9}$$

Since $[\boldsymbol{H}_\ell, \boldsymbol{N}_\ell]$ is also zero, Eq. 2.9 becomes

$$\begin{aligned} \frac{d\boldsymbol{N}_\ell}{dt} &= \frac{i}{\hbar} \left[(\boldsymbol{H}_{C\ell} + \boldsymbol{H}_{\ell C}), N_\ell \right] \\ &= \frac{i}{\hbar} \sum_{\alpha\beta\gamma} \left(V_{C\ell}^{\alpha\beta} \left[c_\alpha^{C\dagger} c_\beta^\ell, c_\gamma^{\ell\dagger} c_\gamma^\ell \right] + V_{\ell C}^{\beta\alpha} \left[c_\beta^{\ell\dagger} c_\alpha^C, c_\gamma^{\ell\dagger} c_\gamma^\ell \right] \right) \end{aligned} \tag{2.10}$$

where we still need to calculate $\left[c_\alpha^{C\dagger} c_\beta^\ell, c_\gamma^{\ell\dagger} c_\gamma^\ell \right]$ and $\left[c_\beta^{\ell\dagger} c_\alpha^C, c_\gamma^{\ell\dagger} c_\gamma^\ell \right]$.

Using the properties

$$[AB, C] = A\,[B, C] + [A, C]\,B \tag{2.11}$$

$$[AB, C] = A\,\{B, C\} - \{A, C\}\,B \tag{2.12}$$

and by replacing the anti-commutators with Eqs. 2.4 and simplifying, we obtain

$$\frac{d\boldsymbol{N}_\ell}{dt} = \frac{i}{\hbar}\sum_{\alpha\beta}\left[V_{C\ell}^{\alpha\beta}c_\alpha^{C\dagger}c_\beta^\ell - V_{\ell C}^{\beta\alpha}c_\beta^{\ell\dagger}c_\alpha^C\right] \tag{2.13}$$

From this, the expectation value of the current given by equation 2.6 is

$$\begin{aligned}\langle I_{\ell\to C}\rangle(t) &= -q_e\left\langle\frac{d\boldsymbol{N}_\ell}{dt}\right\rangle(t)\\ &= -q_e\frac{i}{\hbar}\sum_{\alpha\beta}\left[V_{C\ell}^{\alpha\beta}\left\langle c_\alpha^{C\dagger}(t)\,c_\beta^\ell(t)\right\rangle - V_{\ell C}^{\beta\alpha}\left\langle c_\beta^{\ell\dagger}(t)\,c_\alpha^C(t)\right\rangle\right]\\ &= -q_e\sum_{\alpha\beta}\left[V_{C\ell}^{\alpha\beta}G^<_{\ell C;\beta\alpha}(t,t) - V_{\ell C}^{\beta\alpha}G^<_{C\ell;\alpha\beta}(t,t)\right]\end{aligned} \tag{2.14}$$

where the $G^<$ is the so called lesser Green's function (GF) (also called correlator or propagator) for the electrons (fermions), which is defined as

$$G^<_{xy;\beta\alpha}(t,t') = \frac{i}{\hbar}\left\langle c_\alpha^{x\dagger}(t)\,c_\beta^y(t')\right\rangle \tag{2.15}$$

where $x,\ y$ are generic labels for the regions.

Since these will be needed later on, we also introduce the greater GF $G^>$ defined as

$$G^>_{xy;\alpha\beta}(t,t') = -\frac{i}{\hbar}\left\langle c_\alpha^x(t)\,c_\beta^{y\dagger}(t')\right\rangle, \tag{2.16}$$

the retarded GF G^R as

$$G^R_{xy;\alpha\beta}(t,t') = -\frac{i}{\hbar}\Theta(t-t')\left\langle\left\{c_\alpha^x(t), c_\beta^{y\dagger}(t')\right\}\right\rangle \tag{2.17}$$

and the advanced GF G^A as

$$G^A_{xy;\alpha\beta}(t,t') = \frac{i}{\hbar}\Theta(t'-t)\left\langle\left\{c_\alpha^x(t), c_\beta^{y\dagger}(t')\right\}\right\rangle \tag{2.18}$$

where all these GF's are related to each other via the following equation

$$G^R_{xy;\alpha\beta}(t,t') - G^A_{xy;\alpha\beta}(t,t') = G^>_{xy;\alpha\beta}(t,t') - G^<_{xy;\alpha\beta}(t,t') \tag{2.19}$$

Using a matrix notation for the indices α,β, we can write it as

$$\langle I_{\ell\to C}\rangle(t) = -q_e\left(\mathrm{Tr}\left[\boldsymbol{V}_{C\ell}\cdot\boldsymbol{G}^<_{\ell C}(t,t)\right] - \mathrm{Tr}\left[\boldsymbol{V}_{\ell C}\cdot\boldsymbol{G}^<_{C\ell}(t,t)\right]\right) \tag{2.20}$$

where the bold quantities are matrices of the type

$$\boldsymbol{M}_{xy} = \begin{pmatrix} M_{xy}^{11} & M_{xy}^{12} & M_{xy}^{13} & \cdots\\ M_{xy}^{21} & M_{xy}^{22} & M_{xy}^{23} & \cdots\\ M_{xy}^{31} & M_{xy}^{32} & M_{xy}^{33} & \cdots\\ \vdots & \vdots & \vdots & \ddots\end{pmatrix}$$

with each matrix element encoding the indices α, β , the symbol " $\cdot$ " corresponds to the standard matrix multiplication, x, y are the region labels and the trace is applied over the α, β labels in order to obtain the exact same summation as in Eq. 2.14.

Notice that the GFs in Eq. 2.20 are "mixed", that being, these GFs contain electron operators for both the ℓ contact and the central region. However, our goal is to obtain an expression for the current from the "point of view" of the central region and treat the contacts as perturbations, which can be done by assuming that the contacts are non-interacting (they only exist as electrons reservoirs and only weakly interact with the central region). This separation can be performed by "integrating out" the leads, which means that we basically isolate the contact operators from the central region operators, thus appearing "pure" GFs ("pure" meaning that its operators are from only one of the regions). In order to do that, we need to obtain the expressions for $\boldsymbol{G}^{<}_{\ell C}$ and $\boldsymbol{G}^{<}_{C\ell}$, which is the scope of the next section.

2.3 Integrating out the contacts

In the previous section, we arrived at a expression for the current flowing from the contact ℓ to the central region, present in Eq. 2.20. The GFs present in this equation contain electron operators for both regions, namely $\boldsymbol{G}^{<}_{\ell C}(t,t)$ and $\boldsymbol{G}^{<}_{C\ell}(t,t)$, from which we want to integrate out the leads.

In order to achieve that, we can modify Eq. 2.20 by replacing those GFs by their corresponding Dyson equation, which can be obtained by applying the Langreth's rule for the convolution (present in Eq. A.46 of the Appendix A.3) to the contour ordered Dyson equation present in Eq. A.38 (only considering the term with the single-particle potential V since there is no self-energy for the lead-central region coupling) for $\boldsymbol{G}_{\ell C}(s,s')$, so that

$$\boldsymbol{G}^{<}_{\ell C}(t,t') = \int dt_1 \left[\boldsymbol{g}^{<}_{\ell\ell}(t,t_1)\cdot\boldsymbol{V}_{\ell C}\cdot\boldsymbol{G}^{A}_{CC}(t_1,t') + \boldsymbol{g}^{R}_{\ell\ell}(t,t_1)\cdot\boldsymbol{V}_{\ell C}\cdot\boldsymbol{G}^{<}_{CC}(t_1,t')\right] \tag{2.21}$$

and that

$$\boldsymbol{G}^{<}_{C\ell}(t,t') = \int dt_1 \left[\boldsymbol{G}^{<}_{CC}(t,t_1)\cdot\boldsymbol{V}_{C\ell}\cdot\boldsymbol{g}^{A}_{\ell\ell}(t_1,t') + \boldsymbol{G}^{R}_{CC}(t,t_1)\cdot\boldsymbol{V}_{C\ell}\cdot\boldsymbol{g}^{<}_{\ell\ell}(t_1,t')\right] \tag{2.22}$$

where the GF's with lowercase g are the bare GFs, which do not take into account interactions, and the GF's with uppercase G are the dressed GF's that do take into account interactions.

Plugging Eqs. 2.21 and 2.22 into Eq. 2.20 leads to

$$\begin{aligned}\langle I_{\ell\to C}\rangle(t) = -q_e\int_{t_0}^{t} dt_1 \mathrm{Tr}\left[\boldsymbol{V}_{C\ell}\cdot\boldsymbol{g}^{<}_{\ell\ell}(t,t_1)\cdot\boldsymbol{V}_{\ell C}\cdot\boldsymbol{G}^{A}_{CC}(t_1,t) + \boldsymbol{V}_{C\ell}\cdot\boldsymbol{g}^{R}_{\ell\ell}(t,t_1)\cdot\boldsymbol{V}_{\ell C}\cdot\boldsymbol{G}^{<}_{CC}(t_1,t)\right] \\ + q_e\int_{t_0}^{t} dt_1 \mathrm{Tr}\left[\boldsymbol{V}_{\ell C}\cdot\boldsymbol{G}^{<}_{CC}(t,t_1)\cdot\boldsymbol{V}_{C\ell}\cdot\boldsymbol{g}^{A}_{\ell\ell}(t_1,t) + \boldsymbol{V}_{\ell C}\cdot\boldsymbol{G}^{R}_{CC}(t,t_1)\cdot\boldsymbol{V}_{C\ell}\cdot\boldsymbol{g}^{<}_{\ell\ell}(t_1,t)\right]\end{aligned} \tag{2.23}$$

We can rearrange the third and fourth terms of this expression using the cyclic property of the trace, which gives

$$\begin{aligned}\langle I_{\ell\to C}\rangle(t) = -q_e\int_{t_0}^{t} dt_1 \mathrm{Tr}\left[\boldsymbol{V}_{C\ell}\cdot\boldsymbol{g}^{<}_{\ell\ell}(t,t_1)\cdot\boldsymbol{V}_{\ell C}\cdot\boldsymbol{G}^{A}_{CC}(t_1,t) + \boldsymbol{V}_{C\ell}\cdot\boldsymbol{g}^{R}_{\ell\ell}(t,t_1)\cdot\boldsymbol{V}_{\ell C}\cdot\boldsymbol{G}^{<}_{CC}(t_1,t)\right] \\ + q_e\int_{t_0}^{t} dt_1 \mathrm{Tr}\left[\boldsymbol{G}^{<}_{CC}(t,t_1)\cdot\boldsymbol{V}_{C\ell}\cdot\boldsymbol{g}^{A}_{\ell\ell}(t_1,t)\cdot\boldsymbol{V}_{\ell C} + \boldsymbol{G}^{R}_{CC}(t,t_1)\cdot\boldsymbol{V}_{C\ell}\cdot\boldsymbol{g}^{<}_{\ell\ell}(t_1,t)\cdot\boldsymbol{V}_{\ell C}\right]\end{aligned} \tag{2.24}$$

where we can identify the lesser/retarded/advanced self-energy for the central region due to the coupling to the ℓ contact as

$$\boldsymbol{\Sigma}^{</R/A}_{\ell}(t,t') = \boldsymbol{V}_{C\ell}\cdot\boldsymbol{g}^{</R/A}_{\ell\ell}(t,t')\cdot\boldsymbol{V}_{\ell C} \tag{2.25}$$

allowing us to write $\langle I_{\ell\to C}\rangle$ as

$$\langle I_{\ell\to C}\rangle(t) = -q_e\int_{t_0}^{t} dt_1 \mathrm{Tr}\left[\boldsymbol{\Sigma}^{<}_{\ell}(t,t_1)\cdot\boldsymbol{G}^{A}_{CC}(t_1,t) + \boldsymbol{\Sigma}^{R}_{\ell}(t,t_1)\cdot\boldsymbol{G}^{<}_{CC}(t_1,t)\right] \tag{2.26}$$

$$+ q_e\int_{t_0}^{t} dt_1 \mathrm{Tr}\left[\boldsymbol{G}^{<}_{CC}(t,t_1)\cdot\boldsymbol{\Sigma}^{A}_{\ell}(t_1,t) + \boldsymbol{G}^{R}_{CC}(t,t_1)\cdot\boldsymbol{\Sigma}^{<}_{\ell}(t_1,t)\right] \tag{2.27}$$

Now, we use the following relations

$$\boldsymbol{G}^{R}(t,t') = \Theta(t-t')\left[\boldsymbol{G}^{>}(t,t') - \boldsymbol{G}^{<}(t,t')\right] \tag{2.28}$$

$$\boldsymbol{G}^{A}(t,t') = -\Theta(t'-t)\left[\boldsymbol{G}^{>}(t,t') - \boldsymbol{G}^{<}(t,t')\right] \tag{2.29}$$

to express $\boldsymbol{\Sigma}^{R/A}_{\ell}$ as

$$\begin{aligned}\boldsymbol{\Sigma}^{R}_{\ell}(t,t') &= \boldsymbol{V}_{C\ell}\cdot\left\{\Theta(t-t')\left[\boldsymbol{g}^{>}_{\ell\ell}(t,t') - \boldsymbol{g}^{<}_{\ell\ell}(t,t')\right]\right\}\cdot\boldsymbol{V}_{\ell C} \\ &= \Theta(t-t')\left[\boldsymbol{V}_{C\ell}\cdot\boldsymbol{g}^{>}_{\ell\ell}(t,t')\cdot\boldsymbol{V}_{\ell C} - \boldsymbol{V}_{C\ell}\cdot\boldsymbol{g}^{<}_{\ell\ell}(t,t')\cdot\boldsymbol{V}_{\ell C}\right] \\ &= \Theta(t-t')\left[\boldsymbol{\Sigma}^{>}_{\ell}(t,t') - \boldsymbol{\Sigma}^{<}_{\ell}(t,t')\right]\end{aligned} \tag{2.30}$$

$$\boldsymbol{\Sigma}_{\ell}^{A}(t,t') = -\Theta(t'-t)\left[\boldsymbol{\Sigma}_{\ell}^{>}(t,t') - \boldsymbol{\Sigma}_{\ell}^{<}(t,t')\right] \tag{2.31}$$

allowing us to write Eq. 2.26 as

$$\begin{aligned}\langle I_{\ell\to C}\rangle(t) = -q_e\int_{t_0}^{t} dt_1 \left(\mathrm{Tr}\left[\boldsymbol{G}_{CC}^{<}(t,t_1)\cdot\boldsymbol{\Sigma}_{\ell}^{>}(t_1,t)\right] - \mathrm{Tr}\left[\boldsymbol{\Sigma}_{\ell}^{<}(t,t_1)\cdot\boldsymbol{G}_{CC}^{>}(t_1,t)\right]\right)\\ - q_e\int_{t_0}^{t} dt_1 \left(\mathrm{Tr}\left[\boldsymbol{\Sigma}_{\ell}^{>}(t,t_1)\cdot\boldsymbol{G}_{CC}^{<}(t_1,t)\right] - \mathrm{Tr}\left[\boldsymbol{G}_{CC}^{>}(t,t_1)\cdot\boldsymbol{\Sigma}_{\ell}^{<}(t_1,t)\right]\right)\end{aligned} \tag{2.32}$$

Note that in this expression there are only "pure" GFs/self-energies, so that the current is obtained from the "perspective" of the central region (encoded by $\boldsymbol{G}_{CC}^{\lessgtr}$). The coupling to the contacts is encoded in the self energies $\boldsymbol{\Sigma}_{\ell}^{\lessgtr}$, which in the next sections are going to be treated as perturbations to the central region. We remark that $\boldsymbol{\Sigma}_{\ell}^{\lessgtr}$ correspond to the self-energy of the isolated lead, hence the term "integrating out the leads".

2.4 Current in the stationary limit

In this section, we assume that given enough time, the system will stabilize to a stationary regime where the current does not change with time, meaning that the system acquires time translation symmetry.

Therefore, we aim to obtain the expression for the current that flows in this stationary regime, that being, at times much larger than the initial time t_0 when the system has been taken out of equilibrium (long after the contacts have been coupled to the central region). We remark that with this approach we are in fact neglecting the transient phenomena that occur shortly after the perturbation being switched on.

Mathematically speaking, when this stationary behavior is achieved, all generic functions (here denoted by $\boldsymbol{F}$) have their arguments changed as follows

$$\boldsymbol{F}(t_1,t_2) \to \boldsymbol{F}(t_1-t_2) \tag{2.33}$$

which is equivalent to taking the limit $t-t_0\to\infty$ so that all two-time quantities become only dependent on the difference between those two times.

Therefore, in the stationary limit Eq. 2.32 becomes

$$\begin{aligned}\langle I_{\ell\to C}\rangle(t) = -q_e\int_{t_0}^{t} dt_1 \left(\mathrm{Tr}\left[\boldsymbol{G}_{CC}^{<}(t-t_1)\cdot\boldsymbol{\Sigma}_{\ell}^{>}(t_1-t)\right] - \mathrm{Tr}\left[\boldsymbol{\Sigma}_{\ell}^{<}(t-t_1)\cdot\boldsymbol{G}_{CC}^{>}(t_1-t)\right]\right)\\ - q_e\int_{t_0}^{t} dt_1 \left(\mathrm{Tr}\left[\boldsymbol{\Sigma}_{\ell}^{>}(t-t_1)\cdot\boldsymbol{G}_{CC}^{<}(t_1-t)\right] - \mathrm{Tr}\left[\boldsymbol{G}_{CC}^{>}(t-t_1)\cdot\boldsymbol{\Sigma}_{\ell}^{<}(t_1-t)\right]\right)\end{aligned} \tag{2.34}$$

Going to the frequency domain, the stationary condition means that all two-time quantities can be written as a Fourier transform in time

$$\begin{aligned} F(t_1, t_2) &\to F(t_1 - t_2) \\ &= \int \frac{d\omega}{2\pi} F(\omega)\, e^{-i\omega(t_1 - t_2)} \end{aligned} \tag{2.35}$$

Thus, we can replace $\boldsymbol{G}^{\gtrless}_{CC}$ and $\boldsymbol{\Sigma}^{\gtrless}_{\ell}$ in Eq. 2.32 by their corresponding Fourier transforms present in the last couple of equations, and by using the cyclic property of the trace and manipulating a little we obtain

$$\begin{aligned} \langle I_{\ell\to C}\rangle(t) = q_e \int \frac{d\omega}{2\pi} \int \frac{d\omega'}{2\pi} \int_{t_0}^{t} dt_1 2\cos\left[(\omega-\omega')(t_1 - t)\right] \mathrm{Tr}\left[\boldsymbol{G}^{>}_{CC}(\omega)\cdot\boldsymbol{\Sigma}^{<}_{\ell}(\omega')\right] \\ - q_e \int \frac{d\omega}{2\pi} \int \frac{d\omega'}{2\pi} \int_{t_0}^{t} dt_1 2\cos\left[(\omega-\omega')(t_1 - t)\right] \mathrm{Tr}\left[\boldsymbol{\Sigma}^{>}_{\ell}(\omega')\cdot\boldsymbol{G}^{<}_{CC}(\omega)\right] \end{aligned} \tag{2.36}$$

The time integral can be evaluated as follows

$$2\int_{t_0}^{t} dt_1 \cos\left[(\omega-\omega')(t_1 - t)\right] = \frac{2}{(\omega-\omega')} \sin\left[(\omega-\omega')(t - t_0)\right] \tag{2.37}$$

such that the current becomes

$$\begin{aligned} \langle I_{\ell\to C}\rangle(t) =& q_e \int \frac{d\omega}{2\pi} \int \frac{d\omega'}{2\pi} \frac{2\sin\left[(\omega-\omega')(t - t_0)\right]}{(\omega-\omega')} \\ & \mathrm{Tr}\left[\boldsymbol{G}^{>}_{CC}(\omega)\cdot\boldsymbol{\Sigma}^{<}_{\ell}(\omega')\right] - \mathrm{Tr}\left[\boldsymbol{\Sigma}^{>}_{\ell}(\omega')\cdot\boldsymbol{G}^{<}_{CC}(\omega)\right] \end{aligned} \tag{2.38}$$

The mathematical assumption made for the the stationary limit is that $t - t_0 \to \infty$, meaning that in this regime we can take the following limit

$$\lim_{t-t_0\to\infty} \frac{2\sin\left[(\omega-\omega')(t - t_0)\right]}{(\omega-\omega')} = 2\pi\delta(\omega-\omega') \tag{2.39}$$

and the expression for the current is then found to be

$$\begin{aligned} J_{\ell\to C} &= \lim_{t-t_0\to\infty} \langle I_{\ell\to C}\rangle(t) \\ &= q_e \int \frac{d\omega}{2\pi} \left(\mathrm{Tr}\left[\boldsymbol{G}^{>}_{CC}(\omega)\cdot\boldsymbol{\Sigma}^{<}_{\ell}(\omega)\right] - \mathrm{Tr}\left[\boldsymbol{\Sigma}^{>}_{\ell}(\omega)\cdot\boldsymbol{G}^{<}_{CC}(\omega)\right]\right) \end{aligned} \tag{2.40}$$

We have arrived to the key equation that will be used for the rest of our endeavor. In the next sections we further develop it by making assumptions about $\boldsymbol{G}$ and $\boldsymbol{\Sigma}$. Firstly, we study the non-interacting case, where we assume that the self-energy $\boldsymbol{\Sigma}$ of the central system arises solely from the coupling with the leads, thus neglecting any interaction. Such interactions between the electrons and bosons are then considered, where we will employ a perturbative scheme to obtain corrections to the current, up to second order in the interaction. In both of these cases Eq. 2.40 is the start point.

2.5 Non-interacting case: the Landauer formula

Before we consider the possible interactions that can occur in the central system, which will be the topic of the next section, it is insightful to explore the case where we neglect any kind of interactions.

In order to apply the ballistic transport assumption, we take the Keldysh equation, derived in Eq. A.44 of Appendix A.2, which in frequency domain is given by

$$\boldsymbol{G}_{CC}^{\lessgtr}(\omega) = \boldsymbol{G}_{CC}^{R}(\omega) \cdot \boldsymbol{\Sigma}_{CC}^{\lessgtr}(\omega) \cdot \boldsymbol{G}_{CC}^{A}(\omega) \tag{2.41}$$

and we assume that the self-energy $\boldsymbol{\Sigma}_{CC}^{\lessgtr}$ for the central region has only contributions from the coupling with the leads (thus neglecting any other interactions in the central region) so that

$$\boldsymbol{\Sigma}_{CC}^{\lessgtr}(\omega) = \boldsymbol{\Sigma}_{L}^{\lessgtr}(\omega) + \boldsymbol{\Sigma}_{R}^{\lessgtr}(\omega) \tag{2.42}$$

Plugging these last two equations into Eq. 2.40 leads to

$$\begin{aligned} J_{\ell\to C} = q_e \int \frac{d\omega}{2\pi} \Big(&\mathrm{Tr}\left[\boldsymbol{\Sigma}_{\ell}^{>}(\omega) \cdot \boldsymbol{G}_{CC}^{R}(\omega) \cdot \boldsymbol{\Sigma}_{\ell'}^{<}(\omega) \cdot \boldsymbol{G}_{CC}^{A}(\omega)\right] - \\ &-\mathrm{Tr}\left[\boldsymbol{\Sigma}_{\ell}^{<}(\omega) \cdot \boldsymbol{G}_{CC}^{R}(\omega) \cdot \boldsymbol{\Sigma}_{\ell'}^{>}(\omega) \cdot \boldsymbol{G}_{CC}^{A}(\omega)\right]\Big) \end{aligned} \tag{2.43}$$

We notice that in the definition for $\boldsymbol{\Sigma}_{\ell}^{\lessgtr}$ present in Eq. 2.25 we have $\boldsymbol{g}_{\ell\ell}^{\lessgtr}$ which is the lead's "free" GF, that being, the GF for the lead when it was disconnected from the rest of the system. Thus, we can write $\boldsymbol{g}_{\ell\ell}^{\lessgtr}$ in equilibrium [156] by using the fluctuation-dissipation theorem as

$$\boldsymbol{g}_{\ell\ell}^{<}(\omega) = i f_{\ell}(\omega)\, i\left[\boldsymbol{g}_{\ell\ell}^{R}(\omega) - \boldsymbol{g}_{\ell\ell}^{A}(\omega)\right] \tag{2.44}$$

$$\boldsymbol{g}_{\ell\ell}^{>}(\omega) = -i\left(1 - f_{\ell}(\omega)\right) i\left[\boldsymbol{g}_{\ell\ell}^{R}(\omega) - \boldsymbol{g}_{\ell\ell}^{A}(\omega)\right] \tag{2.45}$$

so that by plugging these expressions into Eq. 2.25 we end up with

$$\boldsymbol{\Sigma}_{\ell}^{<}(\omega) = i f_{\ell}(\omega)\, \boldsymbol{\Gamma}_{\ell}(\omega) \tag{2.46}$$

and

$$\boldsymbol{\Sigma}_{\ell}^{>}(\omega) = -i\left(1 - f_{\ell}(\omega)\right) \boldsymbol{\Gamma}_{\ell}(\omega) \tag{2.47}$$

where we have introduced the so called level width function $\boldsymbol{\Gamma}_{\ell}(\omega)$, which is defined as

$$\begin{aligned} \boldsymbol{\Gamma}_{\ell}(\omega) &= i\left[\boldsymbol{\Sigma}_{\ell}^{R}(\omega) - \boldsymbol{\Sigma}_{\ell}^{A}(\omega)\right] \\ &= i\boldsymbol{V}_{C\ell} \cdot \left[\boldsymbol{g}_{\ell\ell}^{R}(\omega) - \boldsymbol{g}_{\ell\ell}^{A}(\omega)\right] \cdot \boldsymbol{V}_{\ell C} \end{aligned} \tag{2.48}$$

and also the Fermi-Dirac distribution $f_\ell(\omega)$, defined as

$$f_\ell(\omega) = \frac{1}{e^{(\hbar\omega - \mu_\ell)/k_B T} + 1} \tag{2.49}$$

Therefore, choosing the $L \to R$ direction for the current, we can rewrite Eq. 2.43 as

$$J_{L\to C} = q_e \int \frac{d\omega}{2\pi} \left[f_R(\omega) - f_L(\omega)\right] \mathcal{T}(\omega) \tag{2.50}$$

which is commonly known as the Landauer formula, where we have defined the elastic transmission function $\mathcal{T}(\omega)$ as

$$\mathcal{T}(\omega) = \mathrm{Tr}\left[\boldsymbol{\Gamma}_L(\omega) \cdot \boldsymbol{G}^R_{CC}(\omega) \cdot \boldsymbol{\Gamma}_R(\omega) \cdot \boldsymbol{G}^A_{CC}(\omega)\right] \tag{2.51}$$

also known as the Caroli formula.

Historically, Landauer derived a formula [157] for the current at the expense of a transmission function, where the last one was described via transmission/reflection coefficients (and not via GFs). On the other hand, Caroli was the first to use NEGF in mesoscopic transport in a series of 4 papers [151, 158, 159, 160]. Usually, in the context of mesoscopic transport, a "*Landauer-like*" formula is any expression that relates the current with the integral of the difference of two Fermi distributions and a quantity that can be seen as a transmission function. However, since Caroli was pioneer in using NEGF in this context, some authors also call these results a Caroli formula, specially when the transmission function is related to GFs. Because of this, among other reasons, the nomenclature is still not well established in the field, meaning that the same expression can sometimes be either called Caroli formula or Landauer formula, depending on the source.

We also remark that this result was obtained by assuming that the system was non-interacting. In the next section, we investigate the case where the central region supports interactions with a thermal bath of bosons.

2.6 Elastic and inelastic current in the presence of interactions

Until now, we have only considered the Hamiltonian in Eq. 2.1 where the electrons in the central region are taken to be non-interacting.

In this section we consider the case where there are interactions in the central region. In order to account such interaction, we introduce the Hamiltonian $\boldsymbol{H}_{\text{int}}$ (left unspecified for now) into the central

region, so that the total Hamiltonian for that sub-system is now $\boldsymbol{H}_C + \boldsymbol{H}_b + \boldsymbol{H}_{\text{int}}$, with $\boldsymbol{H}_b$ being the independent particle Hamiltonian for the bosons.

Introducing $\boldsymbol{H}_{\text{int}}$ to the problem means that the self-energy expressed in Eq. 2.42 gets an additional term $\boldsymbol{\Sigma}_{\text{int}}$, so that

$$\boldsymbol{\Sigma}^{\lessgtr}_{CC}(\omega) = \boldsymbol{\Sigma}^{\lessgtr}_{L}(\omega) + \boldsymbol{\Sigma}^{\lessgtr}_{R}(\omega) + \boldsymbol{\Sigma}^{\lessgtr}_{\text{int}}(\omega) \tag{2.52}$$

which leads to the rise of an additional contribution to the current due to the scattering of the electrons with the bosons in the central region. Throughout this work, we shall treat this interacting contribution perturbatively, focusing on low order terms. As we will show later in this work, higher order terms are small enough so that we can safely discard them.

Nonetheless, as we show below, the total current flowing through the device can be written as having two contributions: the elastic and the inelastic currents. The elastic current arises solely from the fact that the contacts have different chemical potentials, which naturally leads to the flow of a current where the energy of the flowing electrons does not change. However, the introduction of the interacting Hamiltonian $\boldsymbol{H}_{\text{int}}$ also leads to the re-normalization of the elastic current, which we discuss further below on this section. In order to split the current into its elastic/inelastic contributions, we start by replacing $\boldsymbol{G}^{\lessgtr}_{CC}$ in Eq. 2.40 by the Keldysh equation given by Eq. A.44 (in frequency domain and stationary limit) so that the current becomes

$$\begin{aligned} J_{L\to C} &= q_e \int \frac{d\omega}{2\pi} \left(\text{Tr}\left[\boldsymbol{\Sigma}^{<}_{L}(\omega)\cdot\boldsymbol{G}^{>}_{CC}(\omega)\right] - \text{Tr}\left[\boldsymbol{\Sigma}^{>}_{L}(\omega)\cdot\boldsymbol{G}^{<}_{CC}(\omega)\right]\right) \\ &= q_e \int \frac{d\omega}{2\pi} \left(\text{Tr}\left[\boldsymbol{\Sigma}^{<}_{L}\cdot\boldsymbol{G}^{R}_{CC}\cdot\boldsymbol{\Sigma}^{>}_{CC}\cdot\boldsymbol{G}^{A}_{CC}\right] - \text{Tr}\left[\boldsymbol{\Sigma}^{>}_{L}\cdot\boldsymbol{G}^{R}_{CC}\cdot\boldsymbol{\Sigma}^{<}_{CC}\cdot\boldsymbol{G}^{A}_{CC}\right]\right) \end{aligned} \tag{2.53}$$

where we have hidden the frequency dependency of all quantities for simplicity.

We proceed by splitting $\boldsymbol{\Sigma}^{\lessgtr}_{CC}$ in Eq. 2.52 into a elastic contribution given by

$$\boldsymbol{\Sigma}^{\lessgtr}_{\text{el}} = \boldsymbol{\Sigma}^{\lessgtr}_{L} + \boldsymbol{\Sigma}^{\lessgtr}_{R} \tag{2.54}$$

which was the self-energy that we used in the previous subsection for the non-interacting case, and an inelastic contribution such as

$$\boldsymbol{\Sigma}^{\lessgtr}_{\text{inel}} = \boldsymbol{\Sigma}^{\lessgtr}_{\text{int}} \tag{2.55}$$

Therefore, we can write the current as having elastic and inelastic contributions as

$$J_{L\to C} = J^{\text{el}}_{L\to C} + J^{\text{inel}}_{L\to C} \tag{2.56}$$

with

$$J^{\text{el}}_{L\to C} = q_e \int \frac{d\omega}{2\pi} \left(\text{Tr}\left[\boldsymbol{\Sigma}^{<}_{L} \cdot \boldsymbol{G}^{R}_{CC} \cdot \boldsymbol{\Sigma}^{>}_{\text{el}} \cdot \boldsymbol{G}^{A}_{CC} \right] - \text{Tr}\left[\boldsymbol{\Sigma}^{>}_{L} \cdot \boldsymbol{G}^{R}_{CC} \cdot \boldsymbol{\Sigma}^{<}_{\text{el}} \cdot \boldsymbol{G}^{A}_{CC} \right] \right) \tag{2.57}$$

and

$$J^{\text{inel}}_{L\to C} = q_e \int \frac{d\omega}{2\pi} \left(\text{Tr}\left[\boldsymbol{\Sigma}^{<}_{L} \cdot \boldsymbol{G}^{R}_{CC} \cdot \boldsymbol{\Sigma}^{>}_{\text{int}} \cdot \boldsymbol{G}^{A}_{CC} \right] - \text{Tr}\left[\boldsymbol{\Sigma}^{>}_{L} \cdot \boldsymbol{G}^{R}_{CC} \cdot \boldsymbol{\Sigma}^{<}_{\text{int}} \cdot \boldsymbol{G}^{A}_{CC} \right] \right) \tag{2.58}$$

Now, in order to further develop these expressions we need to find an explicit form for $\boldsymbol{\Sigma}_{\text{int}}$. For that, we start by describing the interaction between the electrons and bosons.

2.6.1 Electron-boson interaction

In order to tackle the problem of finding the expression for $\boldsymbol{\Sigma}_{\text{int}}$, we need to introduce either the Hamiltonian $\boldsymbol{H}_b$ for the free bosons, which is given by

$$\boldsymbol{H}_b = \sum_{\lambda} \hbar\omega_\lambda a^\dagger_\lambda a_\lambda \tag{2.59}$$

and the Hamiltonian $\boldsymbol{H}_{\text{int}}$ for the electron-boson interaction that reads

$$\begin{aligned} \boldsymbol{H}_{\text{int}} &= \sum_{\alpha\beta\lambda} M_{\alpha\beta}(\lambda)\, c^\dagger_\alpha c_\beta \phi_\lambda \\ &= \sum_{\lambda} \boldsymbol{c}^\dagger \cdot \boldsymbol{M}_\lambda \cdot \boldsymbol{c}\phi_\lambda \end{aligned} \tag{2.60}$$

where a_λ $\left(a^\dagger_\lambda\right)$ is the annihilation (creation) operator of a boson in the state λ with energy $\hbar\omega_\lambda$, $\phi_\lambda = \left(a_\lambda + a^\dagger_\lambda\right)/\sqrt{2}$ is a bosonic field operator and $\boldsymbol{M}_\lambda$ (for now left unspecified) is the matrix that couples the electrons to the state λ boson.

We are interested in performing a perturbative expansion on the interaction up to second order in $\boldsymbol{M}_\lambda$. Up to this order, the relevant contributions are the Hartree and the Fock diagrams. However, we can neglect the Hartree term since it originates a self-energy of the type

$$\boldsymbol{\Sigma}^{\text{H}}(t_1, t_2) \propto \delta(t_1 - t_2) \tag{2.61}$$

that is diagonal in time, giving rise to a retarded/advanced contribution to the self-energy but not to a greater/lesser contribution, which in turn are the ones directly linked into the kinetic properties (currents, particle densities...) [148]. As a matter of fact, for the cases where the interacting Hamiltonian is of the form $\sum_{\boldsymbol{k},\boldsymbol{q}} M_q c^\dagger_{\boldsymbol{k}+\boldsymbol{q}} c_{\boldsymbol{k}} \phi_{\boldsymbol{q}}$ with $M_{q=0} = 0$ (e.g. electron-phonon interaction), the Hartree diagram does not appear at all.

Therefore, we focus on the Fock contribution for $\boldsymbol{\Sigma}_{\text{int}}$, which in the contour ordered time domain (derived in Eq. A.66 of Appendix A.4) is given by

$$\boldsymbol{\Sigma}_{\text{int}}(s,s') = i\sum_{\lambda_1\lambda_2} \boldsymbol{M}_{\lambda_1}\cdot\boldsymbol{G}_{CC}(s,s')\cdot\boldsymbol{M}_{\lambda_2} D_{\lambda_1\lambda_2}(s,s') \tag{2.62}$$

where $D_{\lambda_1\lambda_2}(s,s')$ is the contour-ordered bosonic GF.

From the formalism that is derived in this section, we are able to tackle the interaction of the electrons in the central system with any type of bosons, such as phonons, excitons, plasmons, etc..., being only a matter of specifying the bosonic Hamiltonian $\boldsymbol{H}_b$ and the electron-boson interaction $\boldsymbol{H}_{\text{int}}$.

We now proceed to obtain the desired expressions for either $\boldsymbol{J}^{\text{el}}_{L\to C}$ and $\boldsymbol{J}^{\text{inel}}_{L\to C}$ by performing a perturbative expansion on $\boldsymbol{\Sigma}_{\text{int}}$ to retain terms up to $|\boldsymbol{M}_\lambda|^2$.

2.6.2 Elastic current up to second order in M_λ

In order to obtain an explicit expression for the elastic current, we take Eq. 2.57 and replace $\boldsymbol{\Sigma}^{\lessgtr}_{\text{el}}$ by Eq. 2.54, which in turn we replace $\boldsymbol{\Sigma}^{\lessgtr}_{\ell}$ by Eqs. 2.46 and 2.47, so that we obtain

$$J^{\text{el}}_{L\to C} = q_e\int\frac{d\omega}{2\pi}(f_L - f_R)\,\mathcal{T}_{\text{el}} \tag{2.63}$$

with the transmission function $\mathcal{T}_{\text{el}}$ given by

$$\mathcal{T}_{\text{el}} = \text{Tr}\left[\boldsymbol{\Gamma}_L\cdot\boldsymbol{G}^R_{CC}\cdot\boldsymbol{\Gamma}_R\cdot\boldsymbol{G}^A_{CC}\right] \tag{2.64}$$

where $\boldsymbol{G}^{R/A}$ are the fully dressed electronic GFs for the central region. These obey the Dyson equation

$$\boldsymbol{G}^{R/A}_{CC}(\omega) = \boldsymbol{g}^{R/A}_{CC}(\omega) + \boldsymbol{g}^{R/A}_{CC}(\omega)\cdot\boldsymbol{\Sigma}^{R/A}_{\text{int}}(\omega)\cdot\boldsymbol{G}^{R/A}_{CC}(\omega) \tag{2.65}$$

where $\boldsymbol{g}^{R/A}_{CC}$ only takes into account the effect of the leads and not of the interactions.

In order to break the self-consistency of the Dyson equation, we iterate it once and keep only linear terms in $\boldsymbol{\Sigma}_{\text{int}}$ (which in turn is quadratic in $\boldsymbol{M}_\alpha$) as follows

$$\boldsymbol{G}^{R/A}_{CC}(\omega) \simeq \boldsymbol{g}^{R/A}_{CC}(\omega) + \boldsymbol{g}^{R/A}_{CC}(\omega)\cdot\boldsymbol{\Sigma}^{R/A;(2)}_{\text{int}}(\omega)\cdot\boldsymbol{g}^{R/A}_{CC}(\omega) \tag{2.66}$$

where $\boldsymbol{\Sigma}^{R/A;(2)}_{\text{int}}(\omega)$ can be obtained from the contour-ordered self-energy $\boldsymbol{\Sigma}^{(2)}_{\text{int}}$ up to second order, which is given by

$$\boldsymbol{\Sigma}^{(2)}_{\text{int}}(s,s') = i\sum_{\lambda_1\lambda_2}\boldsymbol{M}_{\lambda_1}\cdot\boldsymbol{g}_{CC}(s,s')\cdot\boldsymbol{M}_{\lambda_2}D_{\lambda_1\lambda_2}(s,s')$$

by applying the Langreth rule in Eq. A.50 of Appendix A.3 and Fourier transforming (as is done below).

Introducing this approximation into Eq. 2.64 we obtain

$$\begin{aligned}\mathcal{T}_{\text{el}} &= \text{Tr}\left[\boldsymbol{\Gamma}_L \cdot \boldsymbol{G}^R_{CC} \cdot \boldsymbol{\Gamma}_R \cdot \boldsymbol{G}^A_{CC}\right] \\ &\simeq \text{Tr}\left[\boldsymbol{\Gamma}_L \cdot \boldsymbol{g}^R_{CC} \cdot \boldsymbol{\Gamma}_R \cdot \boldsymbol{g}^A_{CC}\right] + \text{Tr}\left[\boldsymbol{\Gamma}_L \cdot \boldsymbol{g}^R_{CC} \cdot \boldsymbol{\Sigma}^{R;(2)}_{\text{int}} \cdot \boldsymbol{g}^R_{CC} \cdot \boldsymbol{\Gamma}_R \cdot \boldsymbol{g}^A_{CC}\right] \\ &+ \text{Tr}\left[\boldsymbol{\Gamma}_L \cdot \boldsymbol{g}^R_{CC} \cdot \boldsymbol{\Gamma}_R \cdot \boldsymbol{g}^A_{CC} \cdot \boldsymbol{\Sigma}^{A;(2)}_{\text{int}} \cdot \boldsymbol{g}^A_{CC}\right] + \text{Tr}\left[\boldsymbol{\Gamma}_L \cdot \boldsymbol{g}^R_{CC} \cdot \boldsymbol{\Sigma}^{R;(2)}_{\text{int}} \cdot \boldsymbol{g}^R_{CC} \cdot \boldsymbol{\Gamma}_R \cdot \boldsymbol{g}^A_{CC} \cdot \boldsymbol{\Sigma}^{A;(2)}_{\text{int}} \cdot \boldsymbol{g}^A_{CC}\right]\end{aligned} \tag{2.67}$$

The first term does not account for the interactions in the central region and leads to the following contribution to the elastic current

$$J^{\text{el},(0)}_{L\to C} = q_e \int \frac{d\omega}{2\pi} (f_L - f_R)\, \text{Tr}\left[\boldsymbol{\Gamma}_L \cdot \boldsymbol{g}^R_{CC} \cdot \boldsymbol{\Gamma}_R \cdot \boldsymbol{g}^A_{CC}\right] \tag{2.68}$$

Also, since we are only keeping linear terms in $\boldsymbol{\Sigma}^{R/A;(2)}_{\text{int}}$, we can discard the last term and only focus on the remaining two terms

$$\begin{aligned}\mathcal{T}^{(2)}_{\text{el}} &= \text{Tr}\left[\boldsymbol{\Gamma}_L \cdot \boldsymbol{g}^R_{CC} \cdot \boldsymbol{\Sigma}^{R;(2)}_{\text{int}} \cdot \boldsymbol{g}^R_{CC} \cdot \boldsymbol{\Gamma}_R \cdot \boldsymbol{g}^A_{CC}\right] \\ &+ \text{Tr}\left[\boldsymbol{\Gamma}_L \cdot \boldsymbol{g}^R_{CC} \cdot \boldsymbol{\Gamma}_R \cdot \boldsymbol{g}^A_{CC} \cdot \boldsymbol{\Sigma}^{A;(2)}_{\text{int}} \cdot \boldsymbol{g}^A_{CC}\right]\end{aligned} \tag{2.69}$$

Therefore, the first order correction to the elastic current that arises from the electron-boson interaction is given by

$$\begin{aligned}J^{\text{el},(2)}_{L\to C} &= q_e \int \frac{d\omega}{2\pi} (f_L - f_R)\, \mathcal{T}^{(2)}_{\text{el}} \\ &= q_e \int \frac{d\omega}{2\pi} (f_L - f_R)\, \text{Tr}\left[\boldsymbol{\Gamma}_L \cdot \boldsymbol{g}^R_{CC} \cdot \boldsymbol{\Sigma}^{R;(2)}_{\text{int}} \cdot \boldsymbol{g}^R_{CC} \cdot \boldsymbol{\Gamma}_R \cdot \boldsymbol{g}^A_{CC}\right] \\ &+ q_e \int \frac{d\omega}{2\pi} (f_L - f_R)\, \text{Tr}\left[\boldsymbol{\Gamma}_L \cdot \boldsymbol{g}^R_{CC} \cdot \boldsymbol{\Gamma}_R \cdot \boldsymbol{g}^A_{CC} \cdot \boldsymbol{\Sigma}^{A;(2)}_{\text{int}} \cdot \boldsymbol{g}^A_{CC}\right]\end{aligned} \tag{2.70}$$

where we need to find the explicit expression for $\boldsymbol{\Sigma}^{R/A;(2)}_{\text{int}}$. In order to do that we apply the Langreth's rule for the retarded/advanced component of a parallel product (Eq. A.50 of Appendix A.3) into $\boldsymbol{\Sigma}_{\text{int}}(s, s')$ and Fourier transform while assuming the stationary limit so that

$$\boldsymbol{\Sigma}^R_{\text{int}}(\omega) = i \sum_{\lambda_1\lambda_2} \int \frac{d\nu}{2\pi} \left[\boldsymbol{M}_{\lambda_1} \cdot \boldsymbol{G}^<_{CC}(\omega - \nu) \cdot \boldsymbol{M}_{\lambda_2} D^R_{\lambda_1\lambda_2}(\nu) + \boldsymbol{M}_{\lambda_1} \cdot \boldsymbol{G}^R_{CC}(\omega - \nu) \cdot \boldsymbol{M}_{\lambda_2} D^>_{\lambda_1\lambda_2}(\nu)\right] \tag{2.71}$$

Furthermore, we assume that the system that hosts the bosons is in thermal equilibrium and that the interaction with the electrons does not affect its equilibrium properties. It can be seen as the system hosting the bosons being a thermal reservoir in which the central region is immersed in, so that we can

safely neglect the small perturbation that the bosons feel from the interaction with the electrons. This assumption allows us to take $D^R_{\lambda_1\lambda_2}(\nu)$ to be the independent bosonic GF, which then can be written as

$$D^R_{\lambda_1\lambda_2}(\nu) = \delta_{\lambda_1,\lambda_2}\left[\frac{1}{\nu-\omega_\lambda+i0^+} - \frac{1}{\nu+\omega_\lambda+i0^+}\right] \tag{2.72}$$

so that $\boldsymbol{\Sigma}^R_{\text{int}}(\omega)$ becomes

$$\begin{aligned}\boldsymbol{\Sigma}^R_{\text{int}}(\omega) = i\sum_\lambda \int \frac{d\nu}{2\pi}\boldsymbol{M}_{\lambda_1}\cdot\boldsymbol{G}^<_{CC}(\omega-\nu)\cdot\boldsymbol{M}_{\lambda_2}\left[\frac{1}{\nu-\omega_\lambda+i0^+} - \frac{1}{\nu+\omega_\lambda+i0^+}\right] \\ - i\sum_\lambda \int \frac{d\nu}{2\pi}\boldsymbol{M}_{\lambda_1}\cdot\boldsymbol{G}^R_{CC}(\omega-\nu)\cdot\boldsymbol{M}_{\lambda_2}2\pi i\left[(1+b(\omega_\lambda))\,\delta(\nu-\omega_\lambda)+b(\omega_\lambda)\,\delta(\nu+\omega_\lambda)\right]\end{aligned} \tag{2.73}$$

where we have used Eq. 2.82.

If we work at $T=0$K, the Bose-Einstein distribution $b(x)$ present in Eq. 2.84 behaves as

$$\lim_{T\to 0} b(x) = -\Theta(-x) \tag{2.74}$$

and assuming $\omega_\lambda > 0$, we have that $b(\omega_\alpha) \overset{T=0\text{K}}{=} 0$, which simplifies the expression for $\boldsymbol{\Sigma}^R_{\text{int}}$ as

$$\begin{aligned}\boldsymbol{\Sigma}^R_{\text{int}}(\omega) = i\sum_\lambda \int \frac{d\nu}{2\pi}\boldsymbol{M}_{\lambda_1}\cdot\boldsymbol{G}^<_{CC}(\omega-\nu)\cdot\boldsymbol{M}_{\lambda_2}\left[\frac{1}{\nu-\omega_\lambda+i0^+} - \frac{1}{\nu+\omega_\lambda+i0^+}\right] \\ + \sum_\lambda \boldsymbol{M}_{\lambda_1}\cdot\boldsymbol{G}^R_{CC}(\omega-\omega_\lambda)\cdot\boldsymbol{M}_{\lambda_2}\end{aligned} \tag{2.75}$$

Additionally, by using the Keldysh equation for $\boldsymbol{G}^<$ we obtain

$$\begin{aligned}\boldsymbol{\Sigma}^R_{\text{int}}(\omega) = \sum_\lambda \boldsymbol{M}_{\lambda_1}\cdot\boldsymbol{G}^R_{CC}(\omega-\omega_\lambda)\cdot\boldsymbol{M}_{\lambda_2} + \\ + i\sum_\lambda \int \frac{d\nu}{2\pi}\boldsymbol{M}_{\lambda_1}\cdot\boldsymbol{G}^R_{CC}(\omega-\nu)\cdot\boldsymbol{\Sigma}^<_{CC}(\omega-\nu)\cdot\boldsymbol{G}^A_{CC}(\omega-\nu)\cdot \\ \cdot\boldsymbol{M}_{\lambda_2}\left[\frac{1}{\nu-\omega_\lambda+i0^+} - \frac{1}{\nu+\omega_\lambda+i0^+}\right]\end{aligned} \tag{2.76}$$

Since that we only seek terms up to $|M_\lambda|^2$, we can replace the full GFs $\boldsymbol{G}^{R/A}_{CC}$ present in the right hand side by the bare GFs $g^{R/A}_{CC}$ and also replace $\boldsymbol{\Sigma}^<_{CC} = \boldsymbol{\Sigma}^<_L + \boldsymbol{\Sigma}^<_R$to obtain

$$\boldsymbol{\Sigma}_{\text{int}}^{R;(2)}(\omega) = \sum_{\lambda} \boldsymbol{M}_{\lambda_1} \cdot \boldsymbol{g}_{CC}^{R}(\omega - \omega_\lambda) \cdot \boldsymbol{M}_{\lambda_2} + \\ + i \sum_{\lambda} \int \frac{d\nu}{2\pi} \boldsymbol{M}_{\lambda_1} \cdot \boldsymbol{g}_{CC}^{R}(\omega - \nu) \cdot \left[\boldsymbol{\Sigma}_{L}^{<}(\omega - \nu) + \boldsymbol{\Sigma}_{R}^{<}(\omega - \nu)\right] \cdot \\ \cdot \boldsymbol{g}^{A}(\omega - \nu) \cdot \boldsymbol{M}_{\lambda_2} \left[\frac{1}{\nu - \omega_\lambda + i0^+} - \frac{1}{\nu + \omega_\lambda + i0^+}\right] \tag{2.77}$$

Since we consider both leads to be identical we can assume that $\boldsymbol{\Gamma}_L = \boldsymbol{\Gamma}_R = \boldsymbol{\Gamma}$, so that by using Eq. 2.46 in this expression we obtain

$$\boldsymbol{\Sigma}_{\text{int}}^{R;(2)}(\omega) = \sum_{\lambda} \boldsymbol{M}_{\lambda_1} \cdot \boldsymbol{g}_{CC}^{R}(\omega - \omega_\lambda) \cdot \boldsymbol{M}_{\lambda_2} + \\ + i \sum_{\lambda} \int \frac{d\nu}{2\pi} \boldsymbol{M}_{\lambda_1} \cdot \boldsymbol{g}_{CC}^{R}(\omega - \nu) \cdot 2\boldsymbol{\Gamma}(\omega - \nu) \cdot \boldsymbol{g}_{CC}^{A}(\omega - \nu) \cdot \\ \cdot \boldsymbol{M}_{\lambda_2} \left[f_L(\omega - \nu) + f_R(\omega - \nu)\right] \left[\frac{1}{\nu - \omega_\lambda + i0^+} - \frac{1}{\nu + \omega_\lambda + i0^+}\right] \tag{2.78}$$

To further elaborate this expression one needs to calculate the integral in the second term. For that, it is necessary to specify the analytic expressions of the quantities ($\boldsymbol{g}^{R/A}$, $\boldsymbol{\Gamma}$, $\boldsymbol{M}_\alpha$ and f_ℓ) present in this equation, that being, one needs to provide a specific system to work on, so that these quantities can be calculated for that specific system and then replaced in Eq. 2.78.

2.6.3 Inelastic current up to second order in M_λ

For the inelastic contribution, we use Eqs. 2.46 and 2.47 so that Eq. 2.58 becomes

$$J_{L\to C}^{\text{inel}} = iq_e \int \frac{d\omega}{2\pi} f_L \text{Tr}\left[\boldsymbol{\Gamma}_L \cdot \boldsymbol{G}_{CC}^{R} \cdot \boldsymbol{\Sigma}_{\text{int}}^{>} \cdot \boldsymbol{G}_{CC}^{A}\right] \\ + iq_e \int \frac{d\omega}{2\pi} (1 - f_L) \text{Tr}\left[\boldsymbol{\Gamma}_L \cdot \boldsymbol{G}_{CC}^{R} \cdot \boldsymbol{\Sigma}_{\text{int}}^{<} \cdot \boldsymbol{G}_{CC}^{A}\right] \tag{2.79}$$

where $\boldsymbol{\Sigma}_{\text{int}}^{<}$ is given by Eq. 2.87.

In the lowest order in $\boldsymbol{M}_\lambda$, the last equation is given by

$$J_{L\to C}^{\text{inel};(2)} = iq_e \int \frac{d\omega}{2\pi} f_L \text{Tr}\left[\boldsymbol{\Gamma}_L \cdot \boldsymbol{g}_{CC}^{R} \cdot \boldsymbol{\Sigma}_{\text{int}}^{(2);>} \cdot \boldsymbol{g}_{CC}^{A}\right] \\ + iq_e \int \frac{d\omega}{2\pi} (1 - f_L) \text{Tr}\left[\boldsymbol{\Gamma}_L \cdot \boldsymbol{g}_{CC}^{R} \cdot \boldsymbol{\Sigma}_{\text{int}}^{(2);<} \cdot \boldsymbol{g}_{CC}^{A}\right] \tag{2.80}$$

where we need to find the explicit expression for $\boldsymbol{\Sigma}_{\text{int}}^{(2);\lessgtr}$.

For that, we apply the Langreth's rule (present in Eq. A.49 of Appendix A.3) for the parallel product to Eq. 2.62 and Fourier transform it (once again using the stationary limit condition) so that

$$\boldsymbol{\Sigma}^{\lessgtr}_{\text{int}}(\omega) = i\sum_{\alpha_1\alpha_2}\int\frac{d\nu}{2\pi}\boldsymbol{M}_{\alpha_1}\cdot\boldsymbol{G}^{\lessgtr}_{CC}(\omega-\nu)\cdot\boldsymbol{M}_{\alpha_2}D^{\lessgtr}_{\alpha_1\alpha_2}(\nu) \tag{2.81}$$

As we have already mentioned, if we assume that the bosons are in thermal equilibrium, $D^{\lessgtr}_{\lambda_1\lambda_2}(\nu)$ can be written as

$$D^{\lessgtr}_{\lambda_1\lambda_2}(\nu) = \mp i2\pi b(\pm\nu)\,2\omega_{\lambda_1}\text{sgn}(\nu)\,\delta_{\lambda_1,\lambda_2}\delta\left(\nu^2-\omega^2_{\lambda_1}\right) \tag{2.82}$$

and by plugging this in Eq. 2.81 we obtain

$$\begin{aligned}\boldsymbol{\Sigma}^{\lessgtr}_{\text{int}}(\omega) &= i\sum_{\lambda_1\lambda_2}\int\frac{d\nu}{2\pi}\boldsymbol{M}_{\lambda_1}\cdot\boldsymbol{G}^{\lessgtr}_{CC}(\omega-\nu)\cdot\boldsymbol{M}_{\lambda_2}\left[\mp i2\pi b(\pm\nu)\,2\omega_{\lambda_1}\text{sgn}(\nu)\,\delta_{\lambda_1,\lambda_2}\delta\left(\nu^2-\omega^2_{\lambda_1}\right)\right]\\ &= \pm\sum_{\lambda,s=\pm1}\left[\pm sb(\pm s\omega_\lambda)\right]\boldsymbol{M}_\lambda\cdot\boldsymbol{G}^{\lessgtr}_{CC}(\omega-s\omega_\lambda)\cdot\boldsymbol{M}_\lambda\end{aligned} \tag{2.83}$$

where $b(\omega)$ is the Bose-Einstein distribution, defined as

$$b(\omega) = \frac{1}{e^{\hbar\omega/k_BT}-1} \tag{2.84}$$

Focusing on the lesser component, if we replace $\boldsymbol{G}^<$ by its Keldysh Equation then $\boldsymbol{\Sigma}^<_{\text{int}}$ becomes

$$\boldsymbol{\Sigma}^<_{\text{int}}(\omega) = \sum_{\lambda,s=\pm1}\left[sb(s\omega_\lambda)\right]\boldsymbol{M}_\lambda\cdot\boldsymbol{G}^R_{CC}(\omega-s\omega_\lambda)\cdot\boldsymbol{\Sigma}^<_{CC}(\omega-s\omega_\lambda)\cdot\boldsymbol{G}^A_{CC}(\omega-s\omega_\lambda)\cdot\boldsymbol{M}_\lambda \tag{2.85}$$

From Eq. 2.46, Eq. 2.52 can be written as

$$\boldsymbol{\Sigma}^<_{CC} = if_L\boldsymbol{\Gamma}_L + if_R\boldsymbol{\Gamma}_R + \boldsymbol{\Sigma}^<_{\text{int}} \tag{2.86}$$

and by inserting it in Eq.2.85 we obtain

$$\begin{aligned}\boldsymbol{\Sigma}^<_{\text{int}}(\omega) = &\sum_{\lambda,s=\pm1} if_L(\omega-s\omega_\lambda)\left[sb(s\omega_\lambda)\right]\boldsymbol{M}_\lambda\cdot\boldsymbol{G}^R_{CC}(\omega-s\omega_\lambda)\cdot\boldsymbol{\Gamma}_L(\omega-s\omega_\lambda)\cdot\boldsymbol{G}^A_{CC}(\omega-s\omega_\lambda)\cdot\boldsymbol{M}_\lambda\\ &+\sum_{\lambda,s=\pm1} if_R(\omega-s\omega_\lambda)\left[sb(s\omega_\lambda)\right]\boldsymbol{M}_\lambda\cdot\boldsymbol{G}^R_{CC}(\omega-s\omega_\lambda)\cdot\boldsymbol{\Gamma}_R(\omega-s\omega_\lambda)\cdot\boldsymbol{G}^A_{CC}(\omega-s\omega_\lambda)\cdot\boldsymbol{M}_\lambda\\ &+\sum_{\lambda,s=\pm1}\left[sb(s\omega_\lambda)\right]\boldsymbol{M}_\lambda\cdot\boldsymbol{G}^R_{CC}(\omega-s\omega_\lambda)\cdot\boldsymbol{\Sigma}^<_{\text{int}}(\omega-s\omega_\lambda)\cdot\boldsymbol{G}^A_{CC}(\omega-s\omega_\lambda)\cdot\boldsymbol{M}_\lambda\end{aligned} \tag{2.87}$$

We remark that Eq. 2.87 is a self-consistent equation. Since all terms in Eq. 2.87 are already quadratic in $\boldsymbol{M}_\lambda$, iterating it once will generate terms with $|\boldsymbol{M}_\lambda|^4$ that can be already discarded. Therefore,

in lowest order in the electron-boson interaction we can neglect the last term with $\boldsymbol{\Sigma}_{\text{int}}^{<}$ and replace $\boldsymbol{G}_{CC}^{R/A}$ by $\boldsymbol{g}_{CC}^{R/A}$ so that Eq. 2.87 becomes

$$\begin{aligned}
&\boldsymbol{\Sigma}_{\text{int}}^{(2);<}(\omega) \\
&= \sum_{\lambda,s=\pm 1} i f_L(\omega - s\omega_\lambda)\left[sb(s\omega_\lambda)\right] \boldsymbol{M}_\lambda \cdot \boldsymbol{g}_{CC}^{R}(\omega - s\omega_\lambda) \cdot \boldsymbol{\Gamma}_L(\omega - s\omega_\lambda) \cdot \boldsymbol{g}_{CC}^{A}(\omega - s\omega_\lambda) \cdot \boldsymbol{M}_\lambda \\
&+ \sum_{\lambda,s=\pm 1} i f_R(\omega - s\omega_\lambda)\left[sb(s\omega_\lambda)\right] \boldsymbol{M}_\lambda \cdot \boldsymbol{g}_{CC}^{R}(\omega - s\omega_\lambda) \cdot \boldsymbol{\Gamma}_R(\omega - s\omega_\lambda) \cdot \boldsymbol{g}_{CC}^{A}(\omega - s\omega_\lambda) \cdot \boldsymbol{M}_\lambda
\end{aligned} \tag{2.88}$$

where the greater interacting self-energy $\boldsymbol{\Sigma}_{\text{int}}^{>}$ can be obtained by replacing $f_\ell \to 1 - f_\ell$ and $b(s\omega_\alpha) \to b(-s\omega_\alpha)$ in the previous equation, so that

$$\begin{aligned}
&\boldsymbol{\Sigma}_{\text{int}}^{(2);>}(\omega) \\
&= \sum_{\lambda,s=\pm 1} i\left[1 - f_L(\omega - s\omega_\lambda)\right]\left[sb(-s\omega_\lambda)\right] \boldsymbol{M}_\lambda \cdot \boldsymbol{g}_{CC}^{R}(\omega - s\omega_\lambda) \cdot \boldsymbol{\Gamma}_L(\omega - s\omega_\lambda) \cdot \boldsymbol{g}_{CC}^{A}(\omega - s\omega_\lambda) \cdot \boldsymbol{M}_\lambda \\
&+ \sum_{\lambda,s=\pm 1} i\left[1 - f_R(\omega - s\omega_\lambda)\right]\left[sb(-s\omega_\lambda)\right] \boldsymbol{M}_\lambda \cdot \boldsymbol{g}_{CC}^{R}(\omega - s\omega_\lambda) \cdot \boldsymbol{\Gamma}_R(\omega - s\omega_\lambda) \cdot \boldsymbol{g}_{CC}^{A}(\omega - s\omega_\lambda) \cdot \boldsymbol{M}_\lambda
\end{aligned} \tag{2.89}$$

Replacing $\boldsymbol{\Sigma}_{\text{int}}^{(2);\lessgtr}$ present in Eq.2.79 by the expressions obtained in Eqs. 2.88 and 2.89 leads to

$$\begin{aligned}
J_{L\to C}^{\text{inel},(2)}(\omega) = &- \sum_{\lambda,s=\pm 1} q_e \int \frac{d\omega}{2\pi} f_L(\omega)\left[1 - f_L(\omega - s\omega_\lambda)\right]\left[sb(-s\omega_\lambda)\right] \mathcal{T}_{L,L}^{(\lambda,s),(2)}(\omega) \\
&- \sum_{\lambda,s=\pm 1} q_e \int \frac{d\omega}{2\pi} f_L(\omega)\left[1 - f_R(\omega - s\omega_\lambda)\right]\left[sb(-s\omega_\lambda)\right] \mathcal{T}_{L,R}^{(\lambda,s),(2)}(\omega) \\
&- \sum_{\lambda,s=\pm 1} q_e \int \frac{d\omega}{2\pi}\left[1 - f_L(\omega)\right] f_L(\omega - s\omega_\lambda)\left[sb(s\omega_\lambda)\right] \mathcal{T}_{L,L}^{(\lambda,s),(2)}(\omega) \\
&- \sum_{\lambda,s=\pm 1} q_e \int \frac{d\omega}{2\pi}\left[1 - f_L(\omega)\right] f_R(\omega - s\omega_\lambda)\left[sb(s\omega_\lambda)\right] \mathcal{T}_{L,R}^{(\lambda,s),(2)}(\omega)
\end{aligned} \tag{2.90}$$

with the one-boson transmission function given by

$$\begin{aligned}
&\mathcal{T}_{\ell,\ell'}^{(\lambda,s),(2)}(\omega) \\
&= \text{Tr}\left[\boldsymbol{\Gamma}_\ell(\omega) \cdot \boldsymbol{g}_{CC}^{R}(\omega) \cdot \boldsymbol{M}_\lambda \cdot \boldsymbol{g}_{CC}^{R}(\omega - s\omega_\lambda) \cdot \boldsymbol{\Gamma}_{\ell'}(\omega - s\omega_\lambda) \cdot \boldsymbol{g}_{CC}^{A}(\omega - s\omega_\lambda) \cdot \boldsymbol{M}_\lambda \cdot \boldsymbol{g}_{CC}^{A}(\omega)\right]
\end{aligned} \tag{2.91}$$

Since

$$-f_L(\omega)\left[1 - f_L(\omega - s\omega_\lambda)\right]\left[sb(-s\omega_\lambda)\right] = \left[1 - f_L(\omega)\right] f_L(\omega - s\omega_\lambda)\left[sb(s\omega_\lambda)\right] \tag{2.92}$$

the terms proportional to $\mathcal{T}_{L,L}^{(\lambda,s),(1)}$ in Eq. 2.90 cancel with each other, leaving only the terms proportional to $\mathcal{T}_{L,R}^{(\lambda,s),(1)}$ so that

$$J_{\ell\to C}^{\text{inel},(2)}(\omega) = \sum_{\lambda,s=\pm1} q_e \int \frac{d\omega}{2\pi} f_\ell(\omega)\left[1-f_m(\omega-s\omega_\lambda)\right]\left[-sb(-s\omega_\lambda)\right]\mathcal{T}_{\ell,m}^{(\lambda,s),(2)}(\omega)$$
$$- \sum_{\lambda,s=\pm1} q_e \int \frac{d\omega}{2\pi}\left[1-f_\ell(\omega)\right] f_m(\omega-s\omega_\lambda)\left[sb(s\omega_\lambda)\right]\mathcal{T}_{\ell,m}^{(\lambda,s),(2)}(\omega) \tag{2.93}$$

The cancellation of terms that involve only the occupation factor of one contact must occur in order to be in agreement with the stationary regime. In this limit, the current that flows in one direction must be equal to minus the current flowing in the opposite direction, that being $I_{L\to R} = -I_{R\to L}$, since that in the steady state there cannot be any charge accumulation in the device.

We end here the general derivation of the NEGF formalism for mesoscopic transport. For one to further proceed in the calculations, a specific system must be introduced so that the quantities that were left unspecified gain form, allowing the development of the expressions. Therefore, in the next chapter we apply the results shown here to a specific system consisting of two semi-infinite one-dimensional tight-binding chain of atoms coupled to a single-level site.

Chapter 3

Application to an one-dimensional toy-model

In this chapter we apply the methods introduced in the last chapter in lowest order perturbation theory to an one-dimensional toy-model. This allow us to simplify the expressions in order to obtain the corresponding I-V curves. These curves show interesting features such as the opening of additional tunneling channels due to the interactions present in the central region, which in addition to introducing corrections to the elastic current, also give rise to the flow of an inelastic current.

3.1 Introduction to the model

3.1.1 The 1D model Hamiltonian

Now that we have established the theoretical foundations to obtain the current that arises in two-contact devices, we proceed to apply this formalism to a one dimensional toy-model. Although very simple in its nature, this model still captures most of the relevant physical properties that we are looking for in the 3D physical system. As a matter of fact, this model more directly corresponds to the double barrier heterostructure (DBHS) made of GaAs and AlGaAs, studied almost 40 years ago (see Ref. [161]), where resonant tunneling with and without emission of an optical phonon was observed. This structure and the I-V curves with phonon-assisted tunneling are shown in Fig. 5 reproduced from that same article.

Our toy model consists of two leads connected to a central system whose Hamiltonian is

$$H = H_C + \sum_{\ell=L,R} (H_\ell + H_{C\ell} + H_{\ell C}) \tag{3.1}$$

with H_ℓ being the Hamiltonian for a tight-binding chain of atoms

$$H_\ell = \sum_n \left(h c^\dagger_{\ell,n} c_{\ell,n} + t c^\dagger_{\ell,n} c_{\ell,n+1} + t c^\dagger_{\ell,n+1} c_{\ell,n} \right), \tag{3.2}$$

where n is the site label, h the on-site energy, t the nearest neighbor hopping potential and $H_{C\ell}/H_{\ell C}$

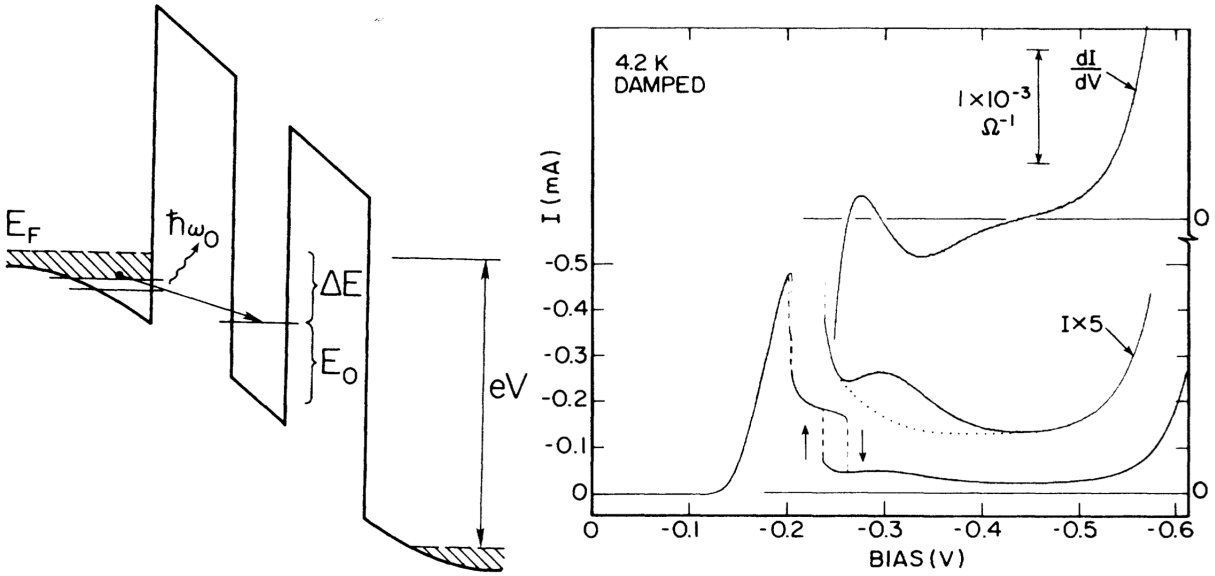


Figure 5: Images reproduced from [161]. **Left:** The conduction-band energy diagram of a DBHS under a bias voltage V. Shown schematically is a LO-phonon assisted tunneling event, where an electron in the left contact (filled up to the Fermi energy E_F) tunnels to the central region level E_0 by emitting a phonon with energy $\hbar\omega_0$. Subsequently, the electron leaves the well by tunneling through the collector barrier. **Right:** The I-V and dI/dV-V curves of the DBHS. The dashed vertical lines show the switching between the high and low current states [162]. The dotted line (drawn by hand) indicates the background current in the replica peak region.

being the Hamiltonian for the coupling between the central region and the first site of each chain

$$H_{C\ell} = V_{C\ell} c_C^\dagger c_{\ell,1}, \tag{3.3}$$

$$H_{\ell C} = V_{\ell C} c_{\ell,1}^\dagger c_C \tag{3.4}$$

with $V_{C\ell} = [V_{\ell C}]^\dagger$ being the hopping potential between the central site and the first site of the ℓ chain. Also, the Hamiltonian H_C for the central region is

$$H_C = H_C^0 + H_\text{b} + H_\text{int}$$

with the single-particle term given by

$$H_C^0 = \varepsilon_0 c^\dagger c,$$

where ε_0 is the energy of the single-level, the free boson term given by

$$H_b = \sum_\lambda \hbar\omega_\lambda a_\lambda^\dagger a_\lambda$$

where ω_λ is the energy of a boson in the λ-mode and the electron-boson interaction given by

$$H_\text{int} = \sum_\lambda M(\lambda)\, c_C^\dagger c_C \phi_\lambda$$

where $M_{\alpha\beta}(\lambda)$ is the interaction matrix that couples the electron operators with the bosonic field ϕ_λ.

The leads are modeled as being two semi-infinite 1D tight-binding chain of atoms and the central region is nothing more than a single-level quantum-dot, as depicted in Fig.6.

We also remark that the left and right leads have different chemical potentials, differing by an amount $V_\text{b} = \mu_L - \mu_R$. This can be understood as applying an external voltage difference V_b in our system, giving rise to a current flowing through the system. Additionally, we have introduced a generalized bosonic excitation in the central region, which can model excitations such as phonons, excitons, plasmons, etc... The interplay between all the energy levels is illustrated in Fig. 7.

As we will readily see, we can extract interesting physical aspects from this idealized system, with the advantage that this specific model allows us to simplify the previously derived expressions for both the transmission function $\mathcal{T}(\omega)$ and the current $J_{L,R}$. To evaluate these quantities, we start by obtaining the analytic expressions for the lead's independent GF $g_{\ell\ell}^R(\omega)$, the level width functions $\Gamma_\ell(\omega)$ and the central region GF $G_{CC}^R(\omega)$.

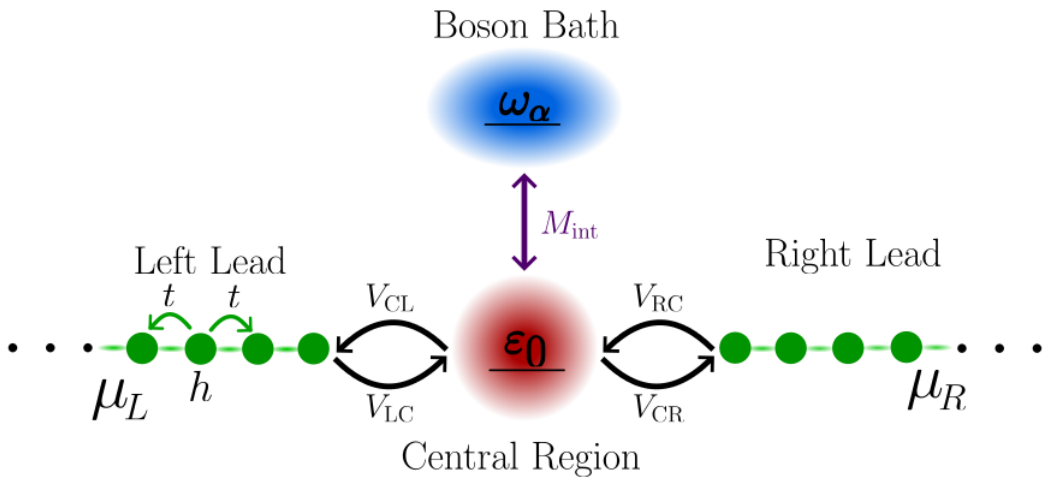


Figure 6: Two semi-infinite 1D tight-binding chains of atoms (green circles) connected to a single-level quantum-dot (red circle) that is in a thermal bath of bosons (blue region).

The atoms on the chains have on-site energies h and nearest neighbor hopping potential t. These chains serve as electrical contacts for the system and have chemical potentials μ_L and μ_R, with $\mu_L > \mu_R$. The leads are connected to the central region via the hopping potential $V_{C\ell}/V_{\ell C}$, with $\ell = L, R$.

The central region's quantum dot has a on-site energy given by ε_0, which is coupled to the bosonic bath via the interaction matrix element M_{int} (in purple).

3.1.2 Green's function for the leads

We start this analysis by obtaining an expression for $g^R_{\ell\ell}$, which is the GF for the isolated lead. For that, consider the Hamiltonian H_ℓ of a semi-infinite tight-binding chain

$$H_\ell = \begin{bmatrix} h & t & & \\ t^\dagger & h & t & \\ & t^\dagger & \ddots & \ddots \\ & & \ddots & \end{bmatrix} \tag{3.5}$$

We remark that so far the lower index ℓ in a function states which of the leads the function corresponds to. However, for this derivation the lower indexes correspond to the specific site of the semi-infinite chain, so that we write the retarded GF for this region simply as g^R. After this derivation is complete, we go back to the older notation where the lower indexes are label the region, such as in $g^R_{\ell\ell}$.

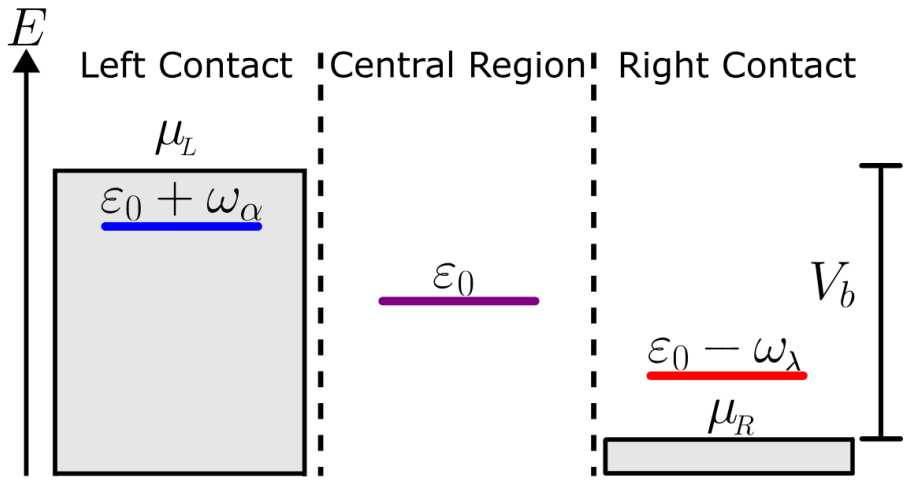


Figure 7: Diagram of the relevant energy levels. The left gray bar corresponds to the Fermi level of the left lead, μ_L, and the right bar to the Fermi level of the right lead, μ_R. These levels differ by an amount of V_b that corresponds to the applied bias voltage. In the middle of the two Fermi levels there is the energy level of central region ε_0 (purple). Additionally, due to the interactions that occur in the central region, which are going to be treated up to second order in perturbation theory, both an inelastic current and a second order correction to the elastic current arise. Thus, we have also included the levels $\varepsilon_0 \pm \omega_\lambda$ (in blue/red, respectively) in the left/right contacts since they have an important role for those contributions to the total current (up to second order). If we kept higher order terms more energy levels would become relevant.

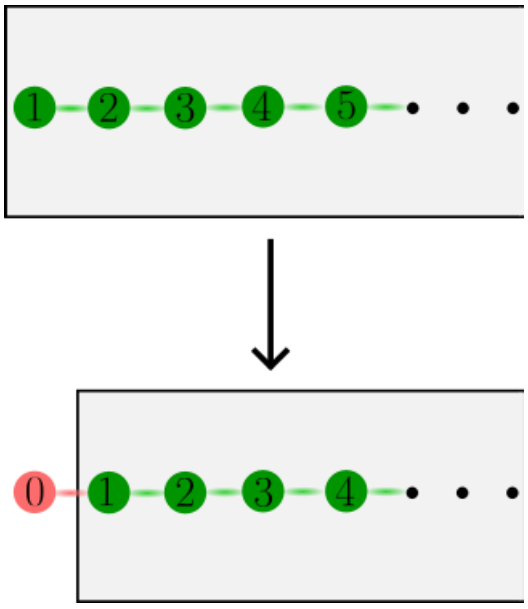


Figure 8: Scheme of a semi-infinite one-dimensional tight-binding chain of atoms (**top**) that we consider to be the contacts of our 1D two-contact device. Such structure can be seen as a single atom (labeled as 0) coupled to a similar semi-infinite chain (**bottom**).

By definition, the Green's function g^R is the solution of

$$\begin{bmatrix} \omega - h & -t & & \\ -t^\dagger & \omega - h & -t & \\ & -t^\dagger & \ddots & \ddots \\ & & \ddots & \end{bmatrix} \begin{bmatrix} g_{1,1} & g_{1,2} & g_{1,3} & \cdots \\ g_{2,1} & g_{2,2} & g_{2,3} & \cdots \\ g_{3,1} & g_{3,2} & g_{3,3} & \cdots \\ \vdots & \vdots & \vdots & \ddots \end{bmatrix} = \begin{bmatrix} 1 & & & \\ & 1 & & \\ & & 1 & \ddots \\ & & \ddots & \ddots \end{bmatrix} \tag{3.6}$$

where we simplified the notation as $g^{R/A}_{nm} \rightarrow g_{nm}$, with n, m being the site labels.

In order to continue the derivation, we note that this semi-infinite chain can be seen from a quite useful perspective. Lets imagine that we removed, say, the first site of the chain. Even so, we would still end up with a semi-infinite chain just like the previous one, the difference being that this new semi-infinite chain would have an extra site coupled to the first one, as depicted in Fig. 8.

Thus, if we treat the hopping between this spare site and the rest of the chain as a perturbation, we can obtain the following equations

$$g = g^0 + g^0 \cdot T \cdot g \tag{3.7}$$

$$g = g^0 + g \cdot T \cdot g^0 \tag{3.8}$$

where g^0 is the Green's functions of the system where the first site is disconnected from the rest of the chain

$$g^0 = \begin{bmatrix} \omega - h & 0 & & \\ 0 & \omega - h & -t & \\ & -t^\dagger & \ddots & \ddots \\ & & \ddots & \end{bmatrix}^{-1} \tag{3.9}$$

and

$$T = \begin{bmatrix} 0 & t & & \\ t^\dagger & 0 & 0 & \\ & 0 & 0 & \ddots \\ & & \ddots & \ddots \end{bmatrix} \tag{3.10}$$

which connects the first site to the rest of the chain.

From these we obtain the following relations

$$g_{1,1} = g^0_{1,1} + g^0_{1,1} \cdot T_{1,2} \cdot g_{2,1} \tag{3.11}$$

$$g_{2,1} = g^0_{2,2} \cdot T_{2,1} \cdot g_{1,1} \tag{3.12}$$

that we can combine, yielding

$$g_{1,1} = \left[\omega - h - t \cdot g^0_{2,2} \cdot t^\dagger\right]^{-1} \tag{3.13}$$

We have arrived to an expression for $g_{1,1}$ that depends on $g^0_{2,2}$. We can change this dependency by noticing that $g^0_{2,2}$ is the GF for the first site of the new semi-infinite chain, which is exactly the same GF as the one that we want to calculate, $g_{1,1}$. Therefore, we have have that $g_{2,2} = g_{1,1}$, such that we obtain the relation

$$|t|^2 \left[g_{1,1}\right]^2 - \left[\omega - h\right] g_{1,1} + 1 = 0 \tag{3.14}$$

where we have used the fact that all variables are scalars. This is only a quadratic equation, so the solutions are

$$g_{1,1} = \frac{1}{2t^2}\left[\omega \pm i0^+ - h \pm \sqrt{\left[\omega \pm i0^+ - h\right]^2 - 4t^2}\right] \tag{3.15}$$

where we performed an analytic continuation on ω. Since we are looking for g^R, we choose the solution that has a negative imaginary part so that we end up with

$$g^R_{1,1}(\omega) = \frac{1}{t}\left[\left(\frac{\omega + i0^+ - h}{2t}\right) - i\sqrt{1 - \left(\frac{\omega + i0^+ - h}{2t}\right)^2}\right] \tag{3.16}$$

which is depicted in Fig. 9 (top). [1]

[1] **Note:** Throughout this work, all plotted quantities are calculated with respect to the lead's hopping parameter t.

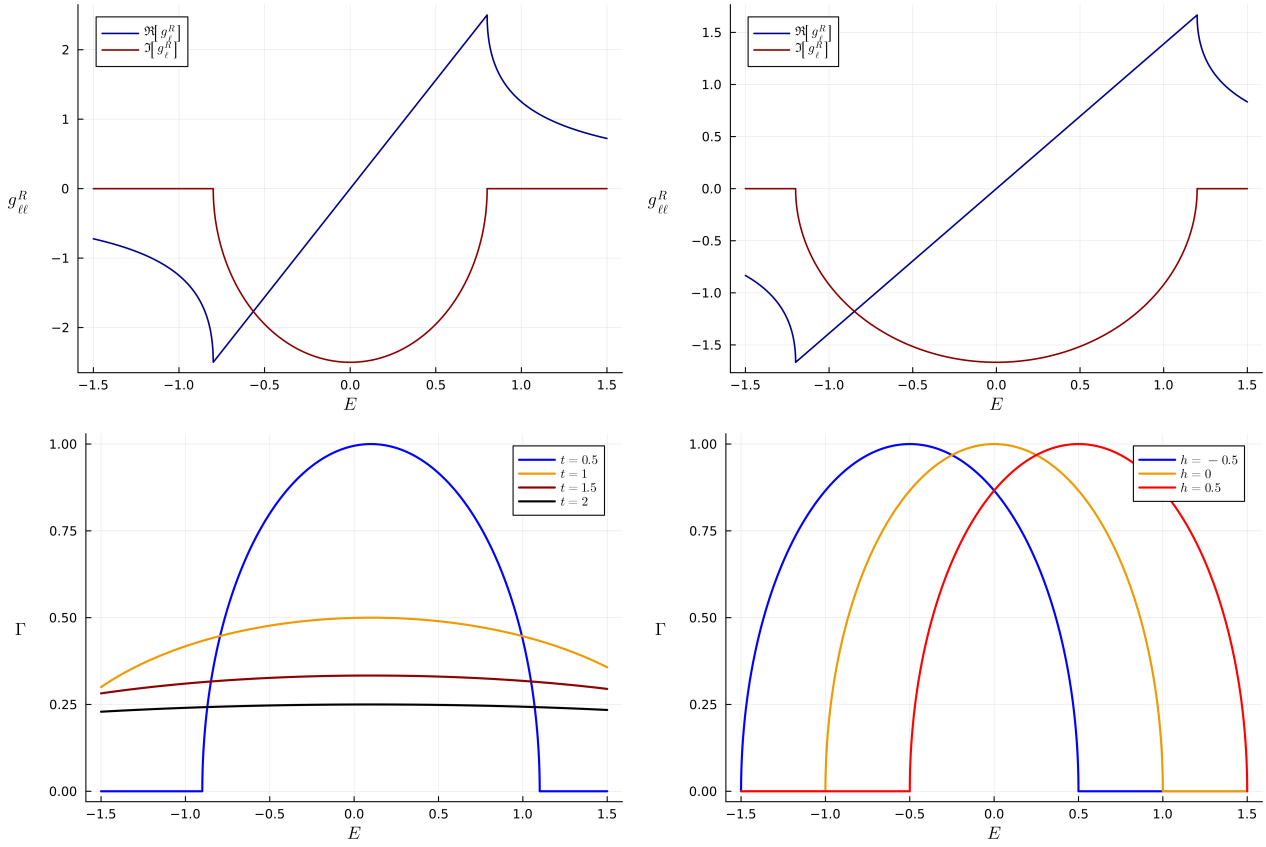


Figure 9: On the top line, the real (blue) and imaginary (red) parts of $g^R_{\ell\ell}$ are plotted for $t = 0.4$ (left) and $t = 0.6$ (right), with $h = 0$. Both real and imaginary parts change abruptly at $\omega = h \pm 2t$. For $|\omega - h| > 2t$ the real part smoothly decays to zero and the imaginary part goes abruptly to zero. On the bottom line, Γ_ℓ is plotted, where in the left we vary t (with $h = 0.1$ and $V_{C\ell} = 0.5$) and in the right we vary h (with $t = 0.5$ and $V_{C\ell} = 0.5$). For small enough t it can be seen that Γ_ℓ is truncated at $\omega = h \pm 2t$. As t increases, the curve gets smaller and broader, tending to a constant value (black curve). Varying h leads to a horizontal shift of the whole plot. All these features are inherited from $\Im\left[g^R_{\ell\ell}\right]$.

Thus the GF for the lead ℓ is

$$g^R_{\ell\ell}(\omega) = \frac{1}{t}\left[\left(\frac{\omega + i0^+ - h}{2t}\right) - i\sqrt{1 - \left(\frac{\omega + i0^+ - h}{2t}\right)^2}\right] \tag{3.17}$$

where we are back with the old notation where ℓ is the label for the lead.

3.1.3 Level width functions

Now we focus on the level width functions Γ_ℓ that we have already mentioned in Chapter 2. From Eqs. 2.46 and 2.47 we have that

$$\begin{aligned}\Gamma_\ell(\omega) &= i\left[\Sigma^>_\ell(\omega) - \Sigma^<_\ell(\omega)\right] \\ &= i\left[\Sigma^R_\ell(\omega) - \Sigma^A_\ell(\omega)\right]\end{aligned} \tag{3.18}$$

and since $\Sigma^A_\ell = \left[\Sigma^R_\ell\right]^\dagger$ (inherited from the same property of G^A) we have

$$\Gamma_\ell = -2\Im\left[\Sigma^R_\ell(\omega)\right] \tag{3.19}$$

Now, the lead induced self-energy Σ^R_ℓ is given by Eq. 2.25 as

$$\Sigma^R_\ell(\omega) = |V_{C\ell}|^2 g^R_{\ell\ell}(\omega) \tag{3.20}$$

so that we have

$$\Gamma_\ell = -2|V_{C\ell}|^2 \Im\left[g^R_{\ell\ell}(\omega)\right] \tag{3.21}$$

Plugging Eq. 3.17 we obtain

$$\Gamma_\ell = 2\frac{|V_{C\ell}|^2}{t}\Re\left\{\sqrt{1 - \left(\frac{\omega + i0^+ - h}{2t}\right)^2}\right\} \tag{3.22}$$

which is shown in Fig. 9 (bottom).

3.1.4 Central region's Green's Function

In order to obtain the Green's function for the central region G^R_{CC} (from which we can obtain G^A_{CC} since $G^A_{CC} = \left[G^R_{CC}\right]^\dagger$), we note that this GF obeys the Dyson equation, which states that

$$G^R_{CC}(\omega) = g^R_{CC}(\omega) + g^R_{CC}(\omega) \cdot \left[\Sigma^R_L(\omega) + \Sigma^R_R(\omega)\right] \cdot G^R_{CC}(\omega) \tag{3.23}$$

where g^R_{CC} is the the central region "bare" GF and Σ^R_ℓ takes into account the coupling with the leads.

We can rewrite this equation by left-multiplying with $\left[g^R_{CC}\right]^{-1}$ so that we obtain

$$G^R_{CC} = \frac{1}{\left[g^R_{CC}\right]^{-1} - \Sigma^R_L - \Sigma^R_R} \tag{3.24}$$

On the other hand, g^R_{CC} can be expressed as

$$g^R_{CC}(\omega) = \frac{1}{\omega\mathbb{I} - H_C} \tag{3.25}$$

which for this particular system we can simply write as

$$g^R_{CC} = \frac{1}{\omega - \varepsilon_0} \tag{3.26}$$

because the Hamiltonian of the central region for this particular system has the simple form

$$H_C = \varepsilon_0 c^\dagger c$$

where c ($c^\dagger$) is the electronic creation (annihilation) operator and ε_0 is the energy for the central region.

Therefore, the Green's function for the central region, plotted in Fig. 10 is

$$G^R_{CC}(\omega) = \frac{1}{\omega - \varepsilon_0 - \Sigma^R_L(\omega) - \Sigma^R_R(\omega)} \tag{3.27}$$

where Σ^R_ℓ $(\ell = L, R)$ is given by Eq.2.25 and accounts for the lead induced dissipation.

We are now equipped with the analytical background needed to further develop the expression for the elastic / inelastic transmission function, and from that the elastic / inelastic current.

3.2 Lowest order elastic transport (without perturbation)

Now that we have obtained the specific expressions of the several quantities for this 1D model, we can now proceed to simplify the perturbative results obtained in chapter 2 in order to get the final results for the transmission function and then the current flowing through this system. We begin by dealing with the elastic transmission in this section.

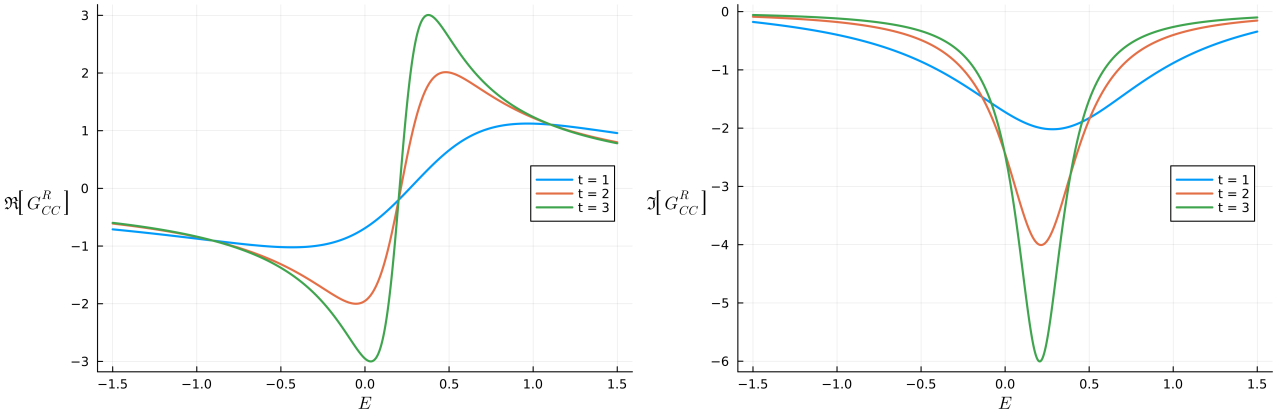


Figure 10: Plot of the real (left) and imaginary (right) parts of G^R_{CC} with $h = 0$, $V_{C\ell} = 0.5$, $\varepsilon_0 = 0.2$ for $t = 1, 2, 3$. These quantities display their relevant features around $\omega = \varepsilon_0$. It can also be seen that as t increases, both the real and imaginary parts are broadened and smoothed.

3.2.1 Elastic transmission function $\mathcal{T}^{(0)}_{\text{el}}$

We start by studying the lowest order elastic current, which was derived in Eq. 2.68, and the corresponding transmission function was given by

$$\mathcal{T}^{(0)}_{\text{el}} = \Gamma_L \cdot g^R_{CC} \cdot \Gamma_R \cdot g^A_{CC} \tag{3.28}$$

where we have suppressed the dependence in ω of the several quantities.

With these considerations, by using Eqs. 3.27 and 3.19 the analytical expression for $\mathcal{T}^{(0)}_{\text{el}}$ becomes

$$\mathcal{T}^{(0)}_{\text{el}} = \frac{\Gamma^2}{\left(\omega - \varepsilon_0 - 2\Re\left[\Sigma^R\right]\right)^2 + \left(2\Im\left[\Sigma^R\right]\right)^2} \tag{3.29}$$

which corresponds to a Lorentzian-like curve centered at $\varepsilon_0 + 2\Re\left[\Sigma^R\right]$ with width $2\Im\left[\Sigma^R\right]$, where we have used the fact that both leads are equivalent $\left(\Sigma^R_L = \Sigma^R_R\right)$, thus removing the region notation in Σ^R

We can further simplify this expression by employing the so called Wide Band Limit (WBL). This consists in neglecting the energy shift stemming from $\Re\left[\Sigma^R\right]$ and removing the dependence in ω of $\Im\left[\Sigma^R\right]$, so that the line width $\Gamma(\omega)$ becomes a constant γ [156]. This approximation is justified by the fact that we are interested in an interval of energies small enough such that we can say that these quantities are slow-varying throughout that same interval, as can be seen in the bottom-left panel of Fig. 9, where either the red and the black curves are close enough to a constant line. In addition to allowing considerable simplifications in the analytical expressions, it also leads to features that are actually close enough to those of real systems.

Therefore, employing the WBL allows us to simplify $\mathcal{T}^{(0)}_{\text{el}}$ as

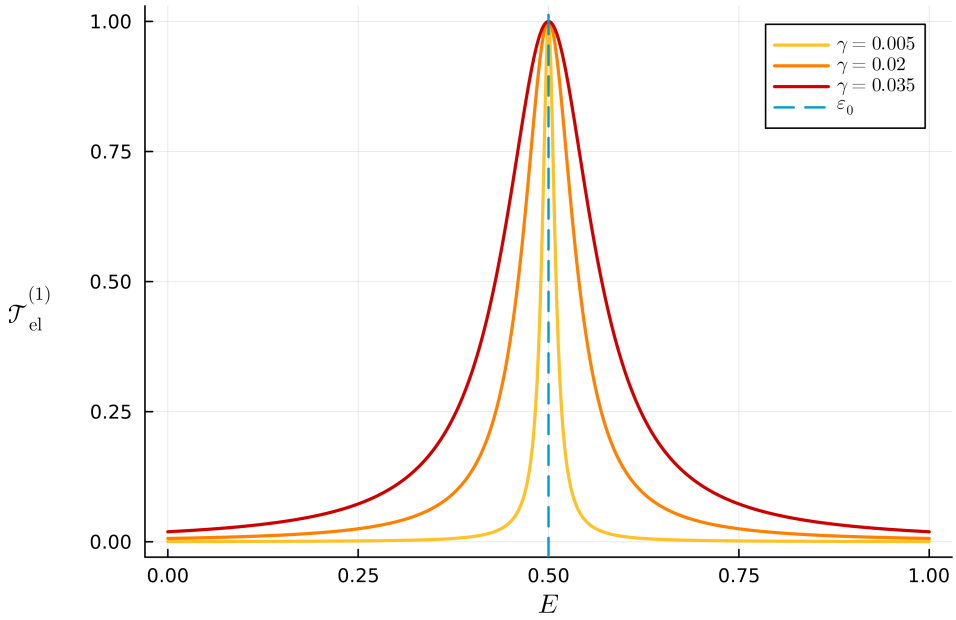


Figure 11: Plot of the elastic transmission function in the WBL regime, expressed in Eq.3.30, for $\gamma = 0.005,\ 0.025$ and 0.05. We remark that it displays a peak marked by a vertical line in blue at $\omega = \varepsilon_0 = 0.6$. Notice that for small γ it becomes very localized and it broadens with increasing γ.

$$\mathcal{T}_{\text{el}}^{(0)}(\omega) = \gamma \frac{\gamma}{(\omega - \varepsilon_0)^2 + \gamma^2} \tag{3.30}$$

with $\gamma = 2\Im\left[\Sigma_L^R\right] \approx$ const., consisting in a mere Lorentzian curve, now with a constant width (not varying with ω), which is plotted in Fig. 11.

3.2.2 Elastic current $J_{\text{el}}^{(0)}$

Now that we have obtained the final expression for $\mathcal{T}_{\text{el}}^{(0)}$, we are able to tackle the problem of finding the elastic current $J_{\text{el}}^{(0)}$ (neglecting interactions). The general expression for the current is given by Eq. 2.50 of the previous chapter as

$$J_{\text{el}} = q_e \int \frac{d\omega}{2\pi} \left\{ f_L(\omega) - f_R(\omega) \right\} \mathcal{T}_{\text{el}}(\omega) \tag{3.31}$$

We can start by simplifying the Fermi-Dirac distributions f_L and f_R by assuming that we are at $T = 0$ so that these distributions take the form of a Heaviside step function Θ as in Eq. 3.40. Therefore, the factor $f_L(\omega) - f_R(\omega)$ present in Eq.3.31 becomes

$$f_L(\omega) - f_R(\omega)\big|_{T=0\text{K}} = \begin{cases} 1 & \text{for } \mu_R < \omega < \mu_L \\ 0 & \text{otherwise} \end{cases}$$

which in practice only changes the limits of integration in Eq. 3.31 as follows

$$J_{\text{el}}^{(0)}\Big|_{T=0\text{K}} = q_e \int_{\mu_R}^{\mu_L} \frac{d\omega}{2\pi} \mathcal{T}_{\text{el}}^{(0)}(\omega) \tag{3.32}$$

where $\mathcal{T}_{\text{el}}^{(0)}$ is given by Eq. 3.30 (in the WBL). Therefore, we have

$$J_{\text{el}}^{(0)}\Big|_{T=0}^{\text{WBL}} = \frac{q_e}{2\pi} \int_{\mu_R}^{\mu_L} d\omega \frac{\gamma^2}{(\omega - \varepsilon_0)^2 + \gamma^2} \tag{3.33}$$

and is plotted in Fig.12.

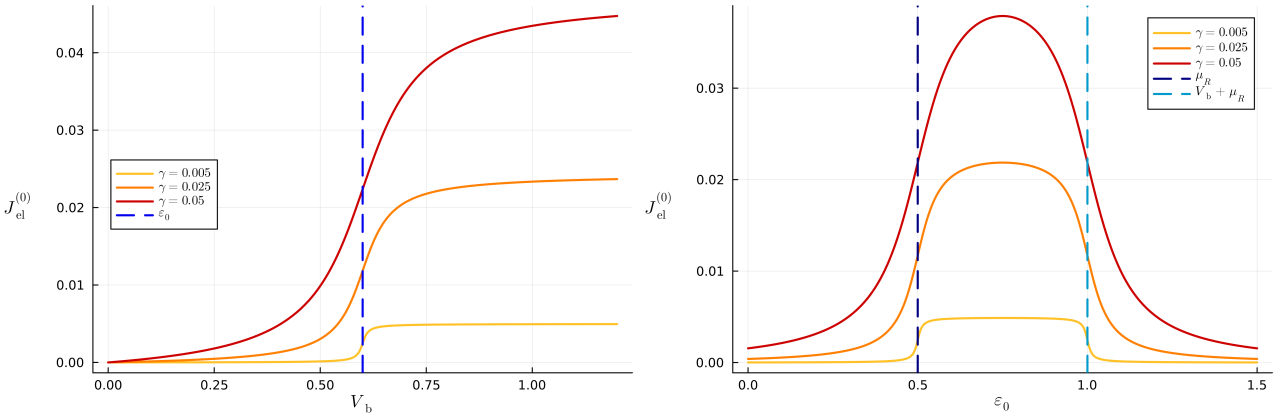


Figure 12: Plot of $J_{\text{el}}^{(0)}$ vs. V_{b} (left) and $J_{\text{el}}^{(0)}$ vs. ε_0 (right) at $T = 0$ in the WBL regime for $\gamma = 0.005,\ 0.025$ and 0.05. **Left:** The vertical blue line is plotted at $V_{\text{b}} = \varepsilon_0$ with $\varepsilon_0 = 0.6$ and $\mu_R = 0$. Notice that the vertical line corresponds to the region where the current increases abruptly, which gets broader with increasing γ. This is occurs because we are integrating $\mathcal{T}_{\text{el}}^{(0)}$ (Eq. 3.30) which displays a peak that is broadened with increasing γ. **Right:** For visual purposes we have set $\mu_R = 0.5$. For $\varepsilon_0 < \mu_R$ the current is zero, but, when ε_0 approaches μ_R it experiences an abrupt increase which is maintained in the region $\mu_R < \varepsilon_0 < \mu_R + V_{\text{b}}$. Then, at $\varepsilon_0 = \mu_R + V_{\text{b}}$ it experiences a sudden decrease and the current goes back to zero. The steepness of the increase/decrease is dictated by γ, which also sets the height of the curve.

In the left plot we have $J_{\text{el}}^{(0)}$ vs. V_{b}. It can be seen that for $V_{\text{b}} < \varepsilon_0$ the current is negligible, which happens because the electrons in the left lead have a lower energy than the one required to cross to the central region, as depicted in the left diagram of Fig. 13. Once V_{b} approaches ε_0 the transmission function $\mathcal{T}_{\text{el}}^{(0)}$ (Fig. 11) increases and the electrons now have the necessary energy to cross the junction, which translates to a drastic increase of the current. Then, for $V_{\text{b}} > \varepsilon_0$ the transmission goes to zero again, leading to a stabilization of the current into a plateau. If the central region had more energy levels (for example if we include interactions, as we will see later), we would see more increases in the current,

but since in this case ε_0 is the only relevant level, it stabilizes for $V_\text{b} > \varepsilon_0$. The right diagram of Fig. 13 illustrates the correct relative positions of μ_R, μ_L and ε_0 in order to have a current flowing through the system. We also remark that the level width γ plays a crucial role, both in magnitude and in the rate at which the current changes. A lower γ means that the central region is weakly coupled to the contacts, which leads to a smaller current but a swifter increase when V_b reaches ε_0. This happens because the weak coupling only allows a small interval around ε_0 to participate in the tunneling process. For higher values of γ the central system is more strongly coupled to the leads, leading to both a higher magnitude and a broader curve, which is the result of a larger region around ε_0 contributing to the transmission of electrons.

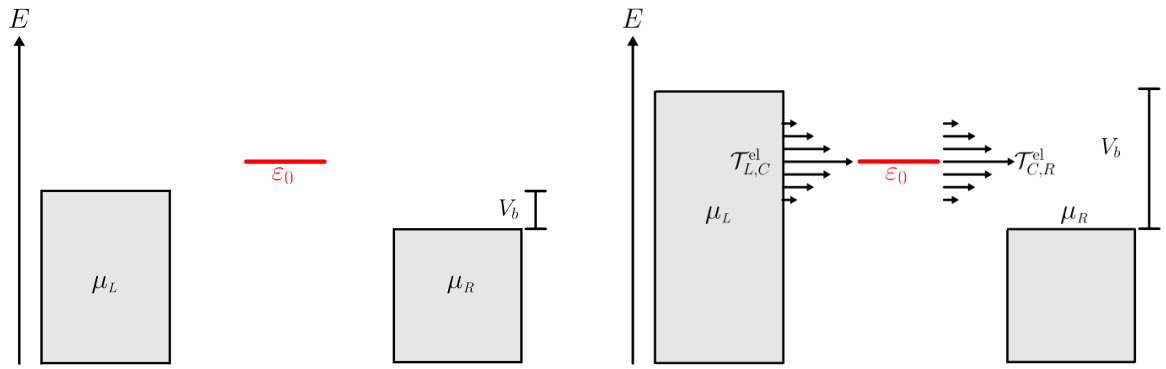


Figure 13: Schematic of the different energies that Eq.3.33 depends on. Here we have the Fermi level μ_L of the left contact shifted from the right contact's Fermi level μ_R (that was set to be the energy reference, that being, $\mu_R = 0$) by an amount V_b that is externally controlled. In the middle of the contact's Fermi levels is the energy level of the central system ε_0 (red) that opens a current channel responsible for the elastic current $J^{(0)}_\text{el}$ arising in the system. **Left:** The energy level of the central region ε_0 is higher than the Fermi levels of both leads, which does not allow for a current to arise. **Right:** The energy level of the central region ε_0 is in between the Fermi level of the leads, that being, $\mu_R < \varepsilon_0 < \mu_L$, which enables the flow of the elastic current. We remark that the electron that crosses the junction maintains its energy and only changes the region where it is located. The black horizontal arrows represent the transmission function $\mathcal{T}^{(0)}_\text{el}$ for either $L \to C$ and $C \to R$.

Therefore, we can infer that in order to obtain a elastic current through a single level without interactions, one must set $V_\text{b} > \varepsilon_0$, otherwise the elastic current flowing through the junction is negligible.

In contrast with the left plot in Fig. 12, in the right plot we fix V_b and vary ε_0. For $\varepsilon_0 < \mu_R$ (illustrated in the left diagram of Fig. 14), the electrons in the central region do not have enough energy to cross to the right lead, so that the flow of a current cannot occur. Once $\varepsilon_0 \geq \mu_R$, the electrons are able to cross to the right lead, giving rise to the flow of a current as depicted in the right plot of Fig. 13. However, if we

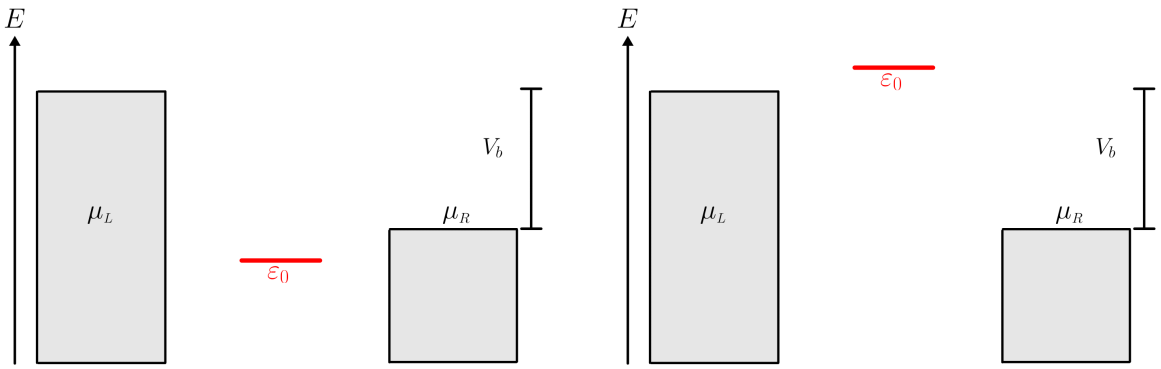


Figure 14: Fermi diagrams for the different cases encountered when varying ε_0 that do not allow the flow of the current $J_{\text{el}}^{(0)}$ **Left:** In this case we have $\varepsilon_0 < \mu_R$, meaning that the electrons are able to cross from the left lead to the central region (because $\mu_L > \varepsilon_0$) but once they arrive at the central region they cannot cross to the right lead, which supresses the flow of a current. **Right:** Here we have $\varepsilon_0 > \mu_L$, which also does not allow the flow of the current. However, in contrast with the case on the left diagram, in this situation the electrons in the left lead are the ones that do not have the required energy to cross to the central region since it has a higher energy than the corresponding Fermi level μ_L.

increase ε_0 enough to overcome μ_L (as can be seen in the right diagram of Fig. 14) then the electrons in the left lead cannot cross to the central region, thus blocking the flow of the current. Therefore, we must set $\mu_R \leq \varepsilon_0 \leq \mu_L$ in order to allow the flow of a current through such junctions.

3.3 Second order correction to the elastic transport

In the previous section we have obtained both the elastic transmission function and the elastic current by neglecting the interactions. In this section we provide the expressions and show the results when the electron-boson interaction is accounted up to second order in perturbation theory.

3.3.1 Correction to the elastic transmission function $\mathcal{T}_{\text{el}}^{(2)}$

We further advance our analysis by noticing that in Eq.2.70, where we have arrived to the general expression for the second order correction to the transmission function $\mathcal{T}_{\text{el}}^{(2)}$, we only seek terms of $\mathbf{\Sigma}_{\text{int}}^{R}$ up to $|M_\lambda|^2$(meaning that we seek the lowest order term $\mathbf{\Sigma}_{\text{int}}^{R;(2)}$). This means that we can replace the exact GFs $G^{R/A}$ present in the right hand side by the approximate GFs $g^{R/A}$ and also replace $\Sigma^{<} \approx \Sigma_L^{<} + \Sigma_R^{<}$so

that

$$\Sigma^R_{\text{int}}(\omega) = \\ = \sum_\lambda |M_\lambda|^2 \left[g^R(\omega - \omega_\lambda) + i \int \frac{d\nu}{2\pi} \left| g^R(\omega - \nu) \right|^2 \left[\Sigma^<_L(\omega - \nu) + \Sigma^<_R(\omega - \nu) \right] \frac{2\omega_\lambda}{(\nu + i0^+)^2 - \omega_\lambda^2} \right] \tag{3.34}$$

Using the fact that in the WBL

$$\begin{aligned} \Sigma^<_\ell(\omega) &= i f_\ell(\omega) \Gamma_\ell(\omega) \\ &\overset{\text{WBL}}{\simeq} i f_\ell(\omega) \gamma \end{aligned} \tag{3.35}$$

we have

$$\Sigma^R_{\text{int}}(\omega) = \\ = \sum_\lambda |M_\lambda|^2 \left[g^R(\omega - \omega_\lambda) - \gamma \int \frac{d\nu}{2\pi} \left| g^R(\omega - \nu) \right|^2 \left[f_L(\omega - \nu) + f_R(\omega - \nu) \right] \frac{2\omega_\lambda}{(\nu + i0^+)^2 - \omega_\lambda^2} \right] \tag{3.36}$$

Replacing g^R by Eq.3.27 (where Σ does not take into account Σ_{int}) in the WBL leads to

$$\begin{aligned} \Sigma^R_{\text{int}}(\omega) = \sum_\lambda |M_\lambda|^2 \Bigg[& \frac{1}{(\omega + i0^+) - \omega_\lambda - \varepsilon_0 + i\gamma} - \\ & - \int \frac{d\nu}{2\pi} \frac{\gamma}{(\omega + i0^+ - \nu - \varepsilon_0)^2 + \gamma^2} \left[f_L(\omega - \nu) + f_R(\omega - \nu) \right] \frac{2\omega_\lambda}{(\nu + i0^+)^2 - \omega_\lambda^2} \Bigg] \end{aligned} \tag{3.37}$$

We now need to handle the remaining integral, either by numerically calculation or by finding an analytical trick to overcome it.

Analytical Approximation

Analytically, we make the assumption that $\gamma \ll \omega_\lambda$ such that we can argue that in this regime $\gamma \to 0$. This assumption is useful because in this limit we have

$$\lim_{\gamma \to 0} \frac{\gamma}{(\omega - \nu - \varepsilon_0)^2 + \gamma^2} = \pi \delta(\omega - \nu - \varepsilon_0) \tag{3.38}$$

so that we can easily calculate the integral, giving

$$\Sigma^R_{\text{int}}(\omega) = \sum_\lambda |M_\lambda|^2 \left[\frac{1}{\omega - \omega_\alpha - \varepsilon_0 + i\gamma} - \left[f_L(\varepsilon_0) + f_R(\varepsilon_0) \right] \frac{\omega_\lambda}{(\omega - \varepsilon_0)^2 - \omega_\lambda^2} \right] \tag{3.39}$$

Since we are at $T = 0$, then we can write $f_\ell(E)$ as

$$\lim_{T\to 0} f_\ell(E) = \Theta(-[E - \mu_\ell]) \tag{3.40}$$

where Θ is the Heaviside step function, so that $f_L(\varepsilon_0) = \Theta(V_\text{b} - \varepsilon_0)$ and $f_R(\varepsilon_0) = 0$ (assuming that $\varepsilon_0 > 0$).

Therefore, we have

$$\Sigma^R_\text{int}(\omega) = \sum_\lambda |M_\lambda|^2 \left[\frac{1}{\omega - \omega_\alpha - \varepsilon_0 + i\gamma} - \frac{\omega_\lambda \Theta(V_b - \varepsilon_0)}{(\omega - \varepsilon_0)^2 - \omega_\lambda^2}\right] \tag{3.41}$$

By plugging Eqs. 3.27 and 3.41 into Eq. 2.69 we obtain an approximated analytical expression for $\mathcal{T}^{(2)}_\text{el}$, given by

$$\begin{aligned}\mathcal{T}^{(2)}_\text{el}(\omega) = 2\sum_\lambda |M_\lambda|^2 \frac{\gamma^2}{(\omega - \varepsilon_0)^2 + \gamma^2} \cdot \\ \cdot \left\{\frac{\omega - \varepsilon_0}{(\omega - \varepsilon_0)^2 + \gamma^2}\left[\frac{\omega - \varepsilon_0 - \omega_\alpha}{(\omega - \omega_\lambda - \varepsilon_0)^2 + \gamma^2} - \frac{\omega_\lambda \Theta(V_\text{b} - \varepsilon_0)}{(\omega - \varepsilon_0)^2 - \omega_\lambda^2}\right] - \right. \\ \left. - \frac{\gamma}{(\omega - \varepsilon_0)^2 + \gamma^2}\frac{\gamma}{(\omega - \omega_\lambda - \varepsilon_0)^2 + \gamma^2}\right\}\end{aligned} \tag{3.42}$$

Numerical evaluation

We can also numerically calculate the integral in Eq. 3.37. The integral is given by

$$I = \int \frac{d\nu}{2\pi}\left[f_L(\omega - \nu) + f_R(\omega - \nu)\right] \frac{\gamma}{(\omega + i0^+ - \nu - \varepsilon_0)^2 + \gamma^2} \frac{2\omega_\lambda}{(\nu + i0^+)^2 - \omega_\lambda^2} \tag{3.43}$$

which has two poles on the real line, at $\nu_\pm = \pm\omega_\lambda$. These two poles can be problematic when numerically calculating this integral, so we need to find a workaround. In order to reduce the size of expressions, we define the function $h(\nu)$ as

$$h(\nu) = \left[f_L(\omega - \nu) + f_R(\omega - \nu)\right] \frac{\gamma}{(\omega + i0^+ - \nu - \varepsilon_0)^2 + \gamma^2} \tag{3.44}$$

so that

$$I = \int \frac{d\nu}{2\pi} h(\nu) \frac{2\omega_\lambda}{(\nu + i0^+)^2 - \omega_\lambda^2}. \tag{3.45}$$

and by employing the Sokhotski-Plemelj theorem we can write

$$\frac{2\omega_\lambda}{(\nu + i0^+)^2 - \omega_\lambda^2} = \mathcal{P}\left(\frac{2\omega_\lambda}{\nu^2 - \omega_\lambda^2}\right) - 2\pi i \omega_\lambda \text{sgn}(\nu)\,\delta\left(\nu^2 - \omega_\lambda^2\right) \tag{3.46}$$

From the following property of the Dirac delta

$$\delta\left(x^2-a^2\right)=\frac{1}{2a}\left[\delta\left(x-a\right)+\delta\left(x+a\right)\right] \tag{3.47}$$

we have that

$$\frac{2\omega_\lambda}{\left(\nu+i0^+\right)^2-\omega_\lambda^2}=\mathcal{P}\left(\frac{2\omega_\lambda}{\nu^2-\omega_\lambda^2}\right)-\pi i\mathrm{sgn}\left(\nu\right)\left[\delta\left(\nu-\omega_\lambda\right)+\delta\left(\nu+\omega_\lambda\right)\right] \tag{3.48}$$

and inserting this into Eq. 3.45 leads to

$$I=\int\frac{d\nu}{2\pi}h\left(\nu\right)\mathcal{P}\left(\frac{2\omega_\lambda}{\nu^2-\omega_\lambda^2}\right)+\frac{i}{2}\left[h\left(-\omega_\lambda\right)-h\left(\omega_\lambda\right)\right] \tag{3.49}$$

We still need to calculate the first term with the principal part. It can be manipulated as

$$\Re\left(I\right)=\int\frac{d\nu}{2\pi}h\left(\nu\right)\mathcal{P}\left(\frac{1}{\nu-\omega_\lambda}-\frac{1}{\nu+\omega_\lambda}\right) \tag{3.50}$$

and by changing the variable ν to $\nu'=\nu-\omega_\alpha$ on the first term and to $\nu''=\nu+\omega_\lambda$ on the second one we have

$$\Re\left(I\right)=\int\frac{d\nu'}{2\pi}\mathcal{P}\left(\frac{1}{\nu'}\right)\left[h\left(\nu'+\omega_\lambda\right)-h\left(\nu'-\omega_\lambda\right)\right] \tag{3.51}$$

Now, by splitting the integral in two, one from $-\infty$ to 0 and the other from 0 to $+\infty$ and manipulating the expression, Eq. 3.43 can be written as

$$\begin{aligned}I=&\frac{i}{2}\left[h\left(-\omega_\lambda\right)-h\left(\omega_\lambda\right)\right]+\int_0^\infty\frac{d\nu}{2\pi}\mathcal{P}\left(\frac{1}{\nu}\right)\cdot\\&\cdot\left[h\left(\nu+\omega_\lambda\right)-h\left(\nu-\omega_\lambda\right)-h\left(-\nu+\omega_\lambda\right)+h\left(-\nu-\omega_\lambda\right)\right]\end{aligned} \tag{3.52}$$

With this procedure we have overcome the problem with the pole at $\nu=0$ by manipulating the expression in a way that the factor in the square brackets tends to ν as ν goes to zero, thus canceling the divergence in $1/\nu$. Also, when numerically calculating the integral, the integration limits are not exactly calculated (only tending to the limits but never reaching them), so that setting the divergent value as one of the integration limits means that the pole is avoided.

Analytical vs. Numerical results

In Fig. 15 we compare the numerical results with the ones obtained analytically. We remark that the analytical results are in closer agreement with the numerical ones for smaller values of γ, which shows that the approximation used in Eq. 3.41 is valid for sufficiently small γ.

Additionally, we show in Fig. 16 the total transmission function $\mathcal{T}_{\mathrm{el}}^{(0)+(2)}$ up to $|\boldsymbol{M}_\lambda|^2$.

We remark that including the effects of electron-boson interactions leads to an increase of the transmission at $\omega=\varepsilon_0\pm\omega_\lambda$, although it also leads to a small suppression at $\omega=\varepsilon_0$.

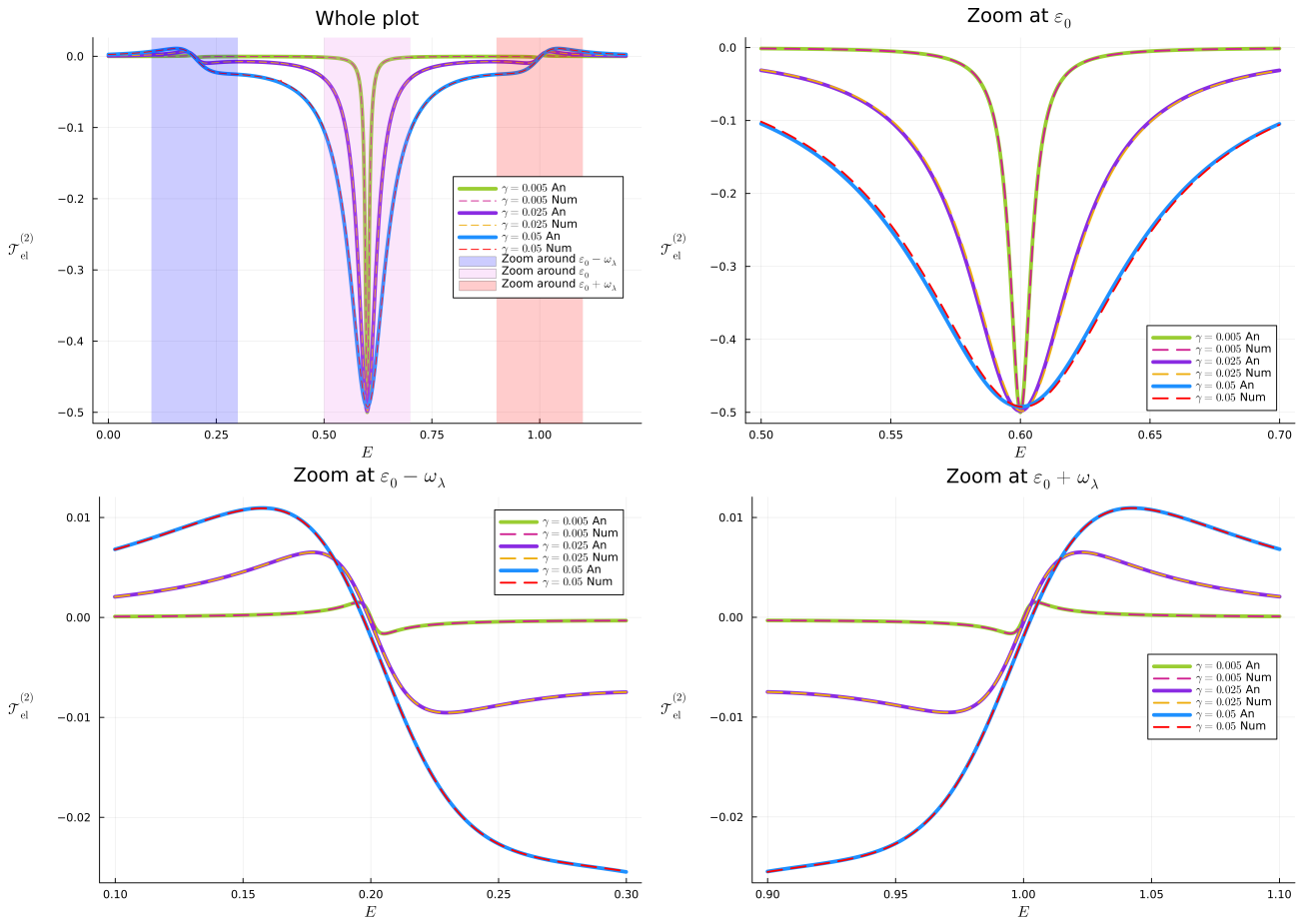


Figure 15: Plot of the lowest order correction to the elastic transmission function in the wide-band limit for $\gamma = 0.005,\ 0.025$ and 0.05, with $\varepsilon_0 = 0.6$, $\omega_\lambda = 0.4$, $M_\lambda = 0.2$, $V_{\rm b} = 3$ and $T = 0$K. The solid lines correspond to the analytical results, while the dashed lines correspond to the numerical ones. The top left plot is along the whole energy range of interest. On the top right plot we zoom at $\omega = \varepsilon_0$ (violet region), where $\mathcal{T}_{\rm el}^{(2)}$ displays the biggest feature. On the bottom left and right plot we zoom at $\omega = \varepsilon_0 - \omega_\lambda$ (blue region) and $\omega = \varepsilon_0 + \omega_\lambda$ (red region), respectively, where the transmission also displays features that stem from the presence of bosons. Notice that for smaller values of γ the transmission $\mathcal{T}_{\rm el}^{(2)}$ becomes more localized around ε_0, getting broader with increasing γ.

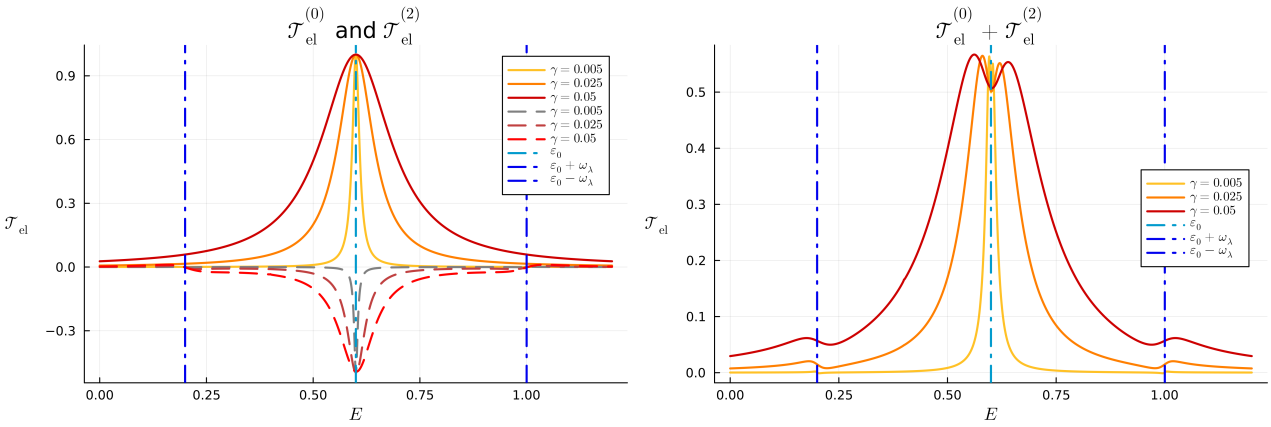


Figure 16: Plot of $\mathcal{T}_{\text{el}}^{(0)}$, $\mathcal{T}_{\text{el}}^{(2)}$ (left) and $\mathcal{T}_{\text{el}}^{(0)} + \mathcal{T}_{\text{el}}^{(2)}$ (right) versus ω with parameters $\varepsilon_0 = 0.6$, $\omega_\lambda = 0.4$, $\mu_R = 0$, $\mu_L = V_b = 3$, $M_\lambda = 0.2$ and $T = 0$K for $\gamma = 0.005$ (yellow), 0.025 (orange), and 0.05 (red). There are three major features: a major one at $\omega = \varepsilon_0$ (vertical light blue line) that arises from the non-interacting case, although it has a decreasing contribution stemming from the interaction with the bosons; and two smaller ones at $\omega = \varepsilon_0 \pm \omega_\lambda$ (vertical dark blue lines) that arise solely from the electron-boson interactions.

3.3.2 Correction to the elastic current $J_{\text{el}}^{(2)}$

From Eq. 3.31, the correction to the elastic current that arises from the electron-boson interactions, up to $|M_\lambda|^2$, is given by

$$J_{\text{el}}^{(2)}\Big|_{T=0\text{K}} = q_e \int_{\mu_R}^{\mu_L} \frac{d\omega}{2\pi} \mathcal{T}_{\text{el}}^{(2)}(\omega)$$

and is shown in Fig.17.

We remark that this second order correction to the elastic current contributes for the total elastic current with a peak at $V_{\text{b}} = \varepsilon_0$ which, as before, is broadened for higher values of γ as well as it is diminished. We remark that the analytical approximation starts to deviate from the numerical results for higher values of γ, as could be expected from the fact that in this approximation we assumed that $\gamma \ll \omega_\lambda$, which starts to break as we increase γ. It should also be noted that the numerical results show an additional feature at $V_{\text{b}} = \varepsilon_0 + \omega_\lambda$ that is not present in the analytical case. This deviation is justified from the fact that the integrand in the numerical calculation has a logarithmic singularity at $\omega = \mu_\ell \pm \omega_\lambda$, which is not captured by the analytical approximation.

Now that we have obtained the final expressions for both $J_{\text{el}}^{(0)}$ and $J_{\text{el}}^{(2)}$, we are in a position where we can obtain the $I - V$ curve for the total elastic current (up to second order in M_λ), which is shown in Fig. 18.

This result shows that by taking into account interactions in the central region (up to the lowest order)

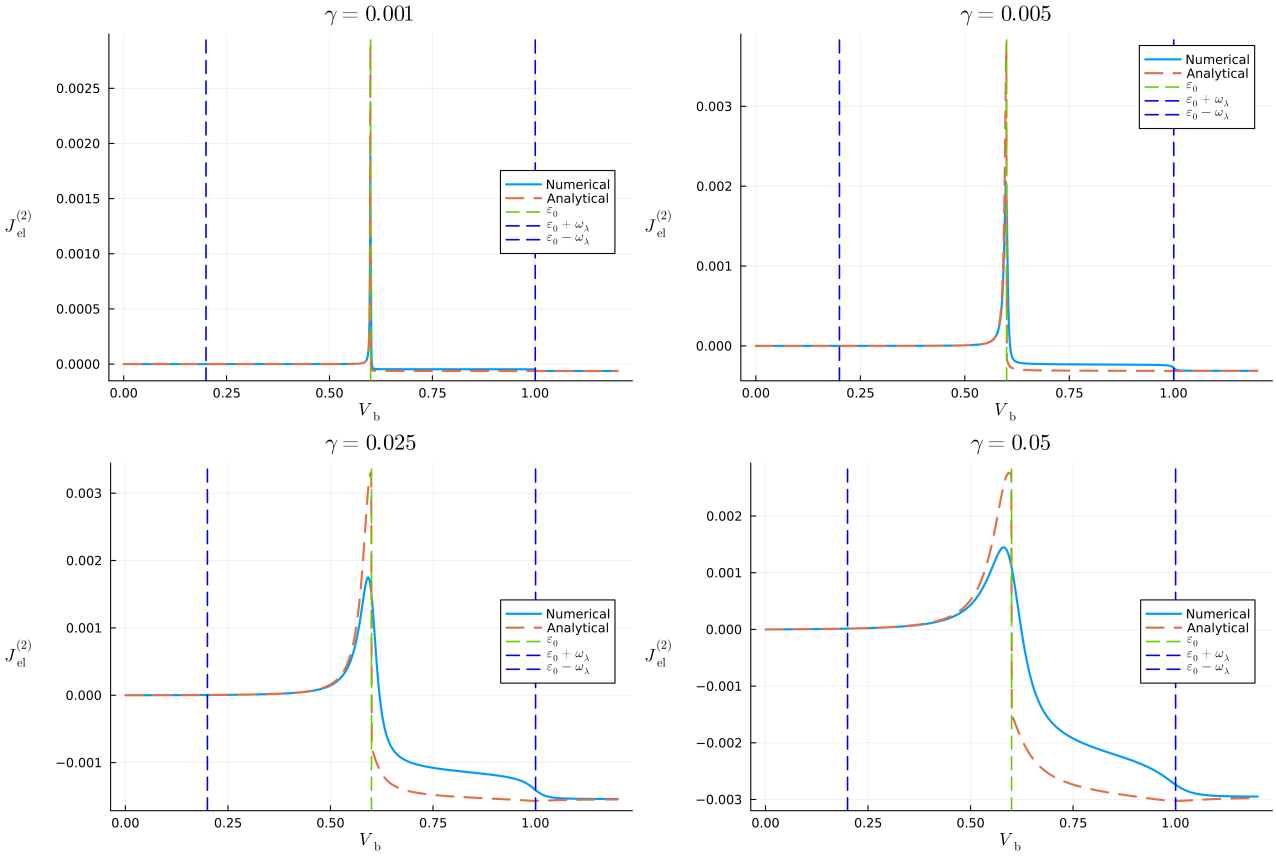


Figure 17: Plot of $J_{\mathrm{el}}^{(2)}$ vs. V_b at $T = 0$ for $\gamma = 0.001$, 0.005, 0.025 and 0.05, either from the analytical results (dashed orange line) or from numerical computation (solid blue line), with $\varepsilon_0 = 0.6$, $\omega_\lambda = 0.4$, $\mu_R = 0$, $\mu_L = V_{\mathrm{b}}$ and $M_\lambda = 0.1$. We remark that both curves tend to overlap for smaller values of γ and that around 10^{-3} are practically similar, corroborating the approximation made in the analytical calculation.

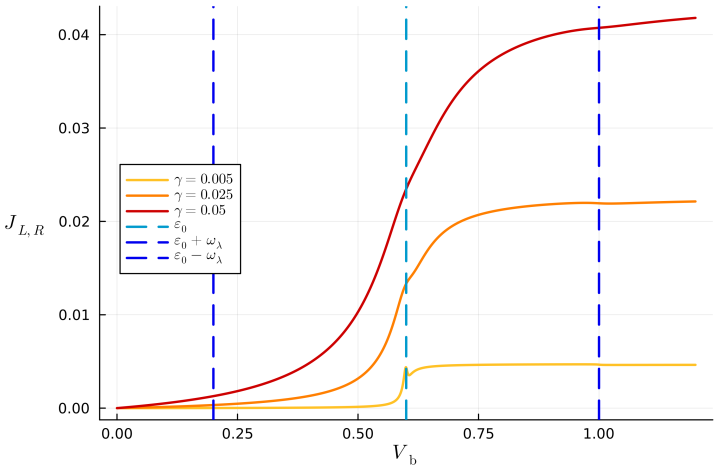


Figure 18: Plot of the total elastic current $J_{\text{el}}^{(0)} + J_{\text{el}}^{(2)}$ vs. V_{b} at $T = 0$ for $\gamma = 0.005$ (yellow), 0.025 (orange) and 0.05 (red) with $\varepsilon_0 = 0.6$, $\omega_\lambda = 0.4$ and $M_\lambda = 0.1$. The lowest order correction $J_{\text{el}}^{(2)}$ (numerically calculated) creates visible features both at $V_{\text{b}} = \varepsilon_0$ and $V_{\text{b}} = \varepsilon_0 + \omega_\lambda$

there is a small contribution followed by a suppression in the elastic current that flows in the system at $V_{\text{b}} = \varepsilon_0$, whereas at $V_{\text{b}} = \varepsilon_0 + \omega_\lambda$ there is also a suppression in $J_{\text{el}}^{(0)+(2)}$ due to the previously mentioned logarithmic divergence.

3.4 Inelastic transport up to second order in M_λ

In the last two sections we have dealt with the elastic contributions to both the transmission and the current. In this section we develop the expressions and show the results for the case of inelastic transport, namely the transmission function and the current, up to $|M_\lambda|^2$.

3.4.1 Inelastic transmission function $\mathcal{T}_{\text{inel}}^{(2)}$

In the last chapter, we have already obtained an expression for the inelastic transmission for a generic system, where the general expression for the inelastic transmission function is in Eq. 2.91 and it reads

$$\mathcal{T}_{\ell,\ell'}^{(\lambda,s)}(\omega) = \\ = \text{Tr}\left[\boldsymbol{\Gamma}_\ell(\omega) \cdot \boldsymbol{G}^R(\omega) \cdot \boldsymbol{M}_\lambda \cdot \boldsymbol{G}^R(\omega - s\omega_\lambda) \cdot \boldsymbol{\Gamma}_{\ell'}(\omega - s\omega_\lambda) \cdot \boldsymbol{G}^A(\omega - s\omega_\lambda) \cdot \boldsymbol{M}_\lambda \cdot \boldsymbol{G}^A(\omega)\right] \tag{3.53}$$

where $s = \pm 1$. We now specify ℓ and ℓ' to follow the $L \to R$ direction, and as before, due to the reduced dimensionality of this modeling system, we can set all quantities as scalars and drop the trace. Therefore, we have

$$\mathcal{T}_{\text{inel}}^{(\lambda,s)}(\omega) = |M_\lambda|^2 G^A(\omega)\,\Gamma_L(\omega)\,G^R(\omega)\,G^R(\omega - s\omega_\lambda)\,\Gamma_R(\omega - s\omega_\lambda)\,G^A(\omega - s\omega_\lambda) \quad (3.54)$$

where the direction $L \to R$ is assumed and thus kept implicit.

From Eq.3.27 the product $G^A(\omega)\,\Gamma_L(\omega)\,G^R(\omega)$ can be rewritten as

$$G^A(\omega)\,\Gamma_L(\omega)\,G^R(\omega) = \frac{-2\Im\left[\Sigma^R(\omega)\right]}{\left(\omega - \varepsilon_0 - 2\Re\left[\Sigma^R(\omega)\right]\right)^2 + \left(2\Im\left[\Sigma^R(\omega)\right]\right)^2} \quad (3.55)$$

where we have set $\Sigma_L^R = \Sigma_R^R = \Sigma^R$ as before and used the fact that $\Gamma_\ell(\omega) = -2\Im\left[\Sigma_\ell^R(\omega)\right]$. The product $G^R(\omega - s\omega_\lambda)\,\Gamma_R(\omega - s\omega_\lambda)\,G^A(\omega - s\omega_\lambda)$ is analogously calculated yielding the same expression with $\omega \to \omega - s\omega_\lambda$.

Therefore, we can infer that for the system that we are studying the second order inelastic transmission function is given by

$$\mathcal{T}_{\text{inel}}^{(\lambda,s)}(\omega) = 4\,|M_\lambda|^2\,\text{Tr}\left[\frac{\Im\left[\Sigma^R(\omega)\right]}{\left(\omega - \varepsilon_0 - 2\Re\left[\Sigma^R(\omega)\right]\right)^2 + \left(2\Im\left[\Sigma^R(\omega)\right]\right)^2} \cdot \right.$$
$$\left. \cdot \frac{\Im\left[\Sigma^R(\omega - s\omega_\lambda)\right]}{\left(\omega - s\omega_\lambda - \varepsilon_0 - 2\Re\left[\Sigma^R(\omega - s\omega_\lambda)\right]\right)^2 + \left(2\Im\left[\Sigma^R(\omega - s\omega_\lambda)\right]\right)^2}\right] \quad (3.56)$$

As for the elastic case, in order to simplify these expressions we employ the WBL, which in practice means neglecting the contribution of $\Re\left[\Sigma^R\right]$ and setting $\Im\left[\Sigma^R\right]$ to be a constant γ. Therefore, in this limit the transmission function can be written as

$$\mathcal{T}_{\text{inel}}^{(\lambda,s)}(\omega) = |M_\lambda|^2 \frac{\gamma}{(\omega - \varepsilon_0)^2 + \gamma^2} \frac{\gamma}{(\omega - s\omega_\lambda - \varepsilon_0)^2 + \gamma^2} \quad (3.57)$$

which is merely the product of two Lorentzians, now with a constant width (not varying with ω). This last expression in Eq.3.57 is plotted in Fig.19 for different values of γ.

In contrast with the elastic transmission function $\mathcal{T}_{\text{el}}$, now we have a total of three possible energy levels in the central region, $\omega = \varepsilon_0$ and $\omega = \varepsilon_0 \pm \omega_\lambda$, which arise from the electron-boson interactions present in the central region. Therefore, there are two channels for the inelastic crossing of electrons through the device, one via the decay $\varepsilon_0 + \omega_\lambda \to \varepsilon_0$ and the other via $\varepsilon_0 \to \varepsilon_0 - \omega_\lambda$, as discussed below with the results for the inelastic current.

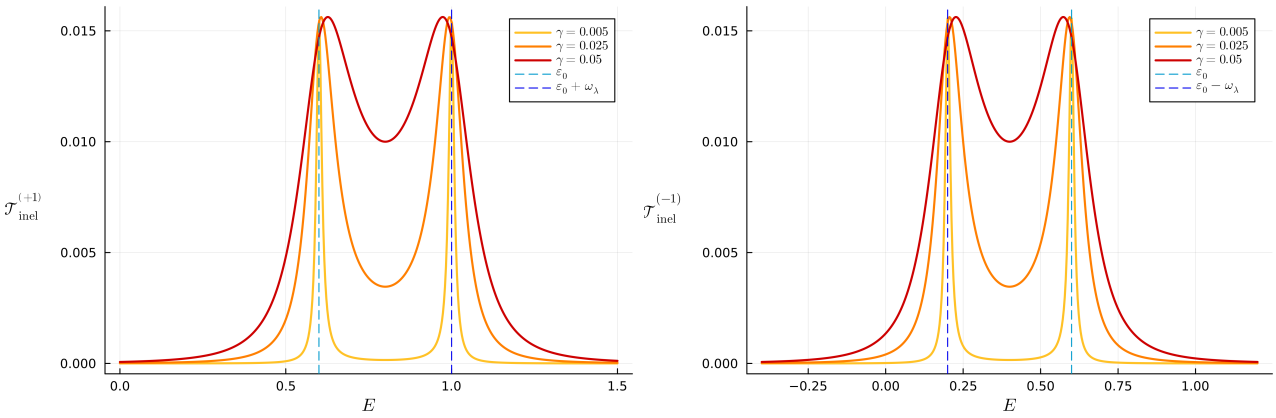


Figure 19: Plot of the inelastic transmission function $\mathcal{T}_{\text{inel}}^{(2)}$ in the WBL regime for $s = +1$ (left) and $s = -1$ (right) given by Eq. 3.57, for $\gamma = 0.005,\ 0.025$ and 0.05 with $\varepsilon_0 = 0.6$, $\omega_\alpha = 0.4$ and $M_\lambda = 0.1$. We remark that all curves display two peaks marked by two vertical lines, a dark blue one which is either at $\omega = \varepsilon_0 + \omega_\lambda$ (left) or $\omega = \varepsilon_0 - \omega_\lambda$ (right) and a light blue line at $\omega = \varepsilon_0$ (both). Notice that for small γ the transmission function becomes very localized around the peaks, and gets broadened with increasing γ.

3.4.2 Lowest order inelastic current $J_{\text{inel}}^{(2)}$

Now that we have arrived to an analytic expression for the inelastic transmission function, we are able to obtain the inelastic current up to $|M_\lambda|^2$, which was generically derived in Eq.2.93 and is given by

$$\begin{aligned} J_{\text{inel}}^{(2)} = &\sum_{\lambda,s=\pm1} q_e \int \frac{d\omega}{2\pi} f_L(\omega)\left[1 - f_R(\omega - s\omega_\lambda)\right]\left[-sb(-s\omega_\lambda)\right]\mathcal{T}_{\text{inel}}^{(\lambda,s)}(\omega) \\ &- \sum_{\lambda,s=\pm1} q_e \int \frac{d\omega}{2\pi}\left[1 - f_L(\omega)\right] f_R(\omega - s\omega_\lambda)\left[sb(s\omega_\lambda)\right]\mathcal{T}_{\text{inel}}^{(\lambda,s)}(\omega) \end{aligned} \tag{3.58}$$

We remark that the variable s is responsible for changing the shape of the Bose-Einstein distribution b, because it either yields $b(\omega_\lambda)$ that corresponds to the absorption of a boson, or $1 + b(\omega_\lambda)$ corresponding to the emission.

Additionally, it is useful to analyze the occupation factors f and b present in the expression because they can be simplified for $T = 0$.

First term

On the argument of the first integral, there appears the factor

$$f_L(\omega)\left[1 - f_R(\omega - s\omega_\lambda)\right]\left[-sb(-s\omega_\lambda)\right] \tag{3.59}$$

Since we are at $T = 0K$, the distribution $b\left(E,T\right)$ can be simplified as

$$\lim_{T\to 0} b\left(E,T\right) = -\Theta\left(-E\right) \tag{3.60}$$

Therefore we can write the expression in Eq.3.59 as

$$\begin{aligned}&\lim_{t\to\infty} f_L\left(\omega\right)\left[1-f_R\left(\omega-s\omega_\lambda\right)\right]\left[-sb\left(-s\omega_\lambda\right)\right] = \\ &= \Theta\left(-\left[\omega-\mu_L\right]\right)\left[1-\Theta\left(-\left[\omega-s\omega_\lambda-\mu_R\right]\right)\right]s\Theta\left(s\omega_\lambda\right)\end{aligned} \tag{3.61}$$

where we can note that $\Theta\left(s\omega_\lambda\right)$ is only non-zero for $s = 1$ (since $\omega_\lambda > 0$) corresponding to the emission of a boson, which is the only process that can happen at $T = 0K$ since that at these temperatures there is no bosons in the environment to be absorbed.

Additionally, if we write $\mu_L = \mu_R + V_\mathrm{b}$ and also if we set $\mu_R = 0$ as being our energy reference, then we obtain

$$\lim_{t\to\infty} f_L\left(\omega\right)\left[1-f_R\left(\omega-\omega_\lambda\right)\right]\left[-b\left(-\omega_\lambda\right)\right] = \Theta\left(V_\mathrm{b}-\omega\right)\left[1-\Theta\left(\omega_\lambda-\omega\right)\right] \tag{3.62}$$

which is plotted in Fig. 20. We can readily notice on the RHS that the term in square brackets is non-zero only for $\omega > \omega_\lambda$ and that $\Theta\left(V_\mathrm{b}-\omega\right)$ is non-zero only for $\omega < V_\mathrm{b}$. Since we are assuming that $\omega_\lambda > 0$, in order for this expression to be non-zero we also need to have $V_\mathrm{b} > \omega_\lambda$.

From Fig.20, we can see that the first term in Eq.2.93 can be rewritten as (assuming $\omega_\alpha < V_\mathrm{b}$)

$$\sum_{\lambda,s=\pm 1} q_e \int \frac{d\omega}{2\pi} f_L\left(\omega\right)\left[1-f_R\left(\omega-s\omega_\lambda\right)\right]\left[-sb\left(-s\omega_\lambda\right)\right]\mathcal{T}_{\mathrm{inel}}^{(\lambda,s)}\left(\omega\right) = \sum_\alpha q_e \int_{\omega_\lambda}^{V_\mathrm{b}} \frac{d\omega}{2\pi}\mathcal{T}_{\mathrm{inel}}^{(\lambda,+1)}\left(\omega\right) \tag{3.63}$$

Second term

Proceeding to the argument of the second integral, the limit of its distributions factors when $T \to 0$ is

$$\lim_{T\to 0}\left[1-f_L\left(\omega\right)\right]f_R\left(\omega-s\omega_\lambda\right)\left[sb\left(s\omega_\lambda\right)\right] = \left[1-\Theta\left(\mu_L-\omega\right)\right]\Theta\left(\mu_R+s\omega_\lambda-\omega\right)\left[-s\Theta\left(-s\omega_\lambda\right)\right] \tag{3.64}$$

and once again noticing that $\Theta\left(-s\omega_\lambda\right)$ is only non-zero for $s = -1$ (assuming positive ω_λ), the second term in Eq.2.93 becomes (with $\mu_L = \mu_R + V_\mathrm{b}$ and $\mu_R = 0$)

$$\begin{aligned}&\sum_{\lambda,s=\pm 1} q_e \int \frac{d\omega}{2\pi}\left[1-f_L\left(\omega\right)\right]f_R\left(\omega-s\omega_\lambda\right)\left[sb\left(s\omega_\lambda\right)\right]\mathcal{T}_{L,R}^{(\lambda,s)}\left(\omega\right) = \\ &= \sum_\alpha q_e \int \frac{d\omega}{2\pi}\left[1-\Theta\left(V_\mathrm{b}-\omega\right)\right]\cdot\cdot\Theta\left(-\omega_\lambda-\omega\right)\mathcal{T}_{L,R}^{(\lambda,-1)}\left(\omega\right)\end{aligned}$$

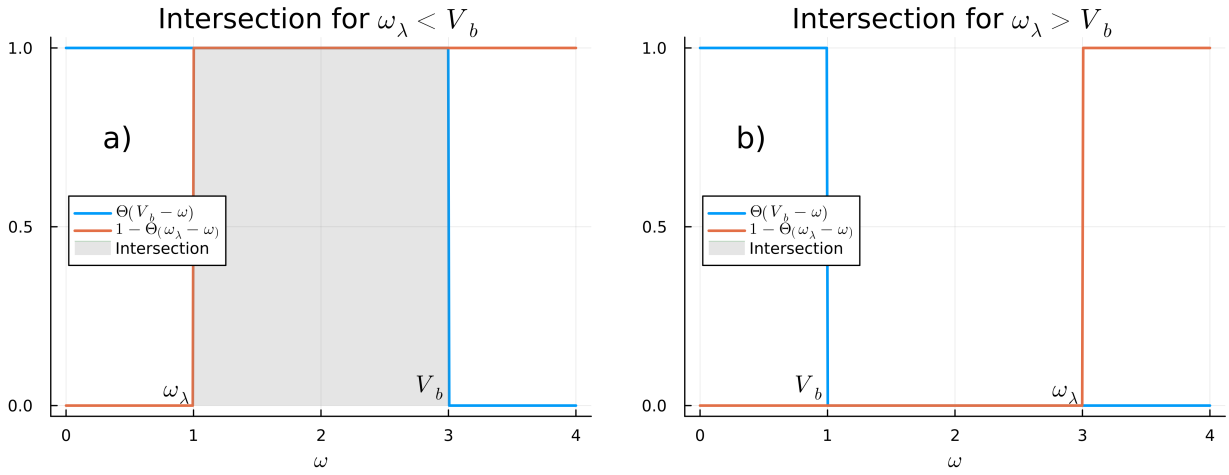


Figure 20: Plot of the Fermi-Dirac distribution factors that arise in the first term of Eq.3.59 for $T = 0K$, $\mu_R = 0$ and $s = +1$, where we have restrained V_b to positive values. **a)** On the left, we have set $V_\text{b} = 3$ and $V_\text{b} > \omega_\lambda = 1$, so that there is a finite region (in gray) where both functions overlap. **b)** On the right, we have set $V_\text{b} = 1$ and $V_\text{b} < \omega_\lambda = 3$, so that these two functions don't overlap, which leads to the integral's argument being zero for all possible values of ω. This means that the first term in Eq.3.59 vanishes for boson energies ω_λ greater than the bias potential V_b.

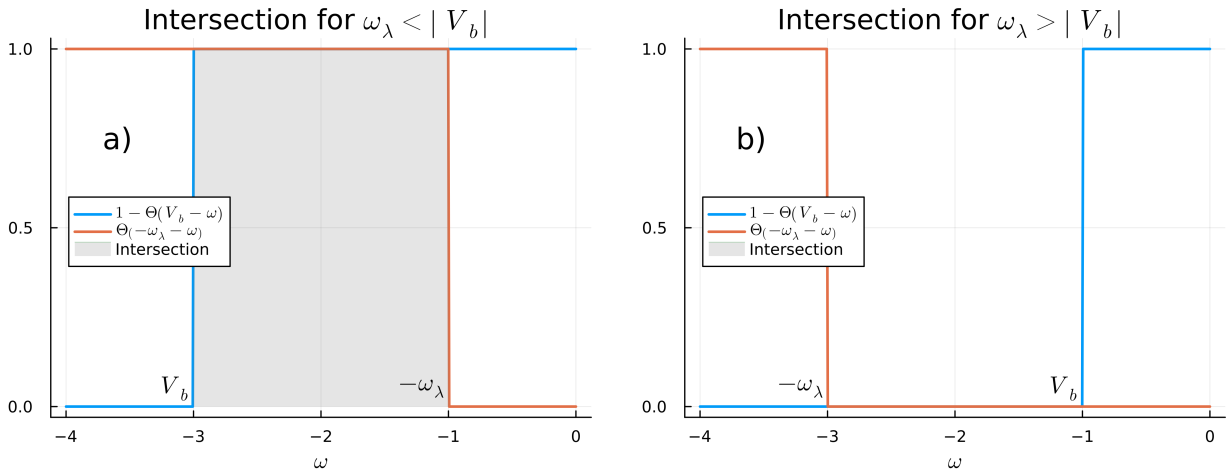


Figure 21: Plot of the Fermi-Dirac distribution factors that arise in the second term of Eq. **??** for $T = 0K$, $\mu_R = 0$ and $s = -1$, where we have restrained V_b to negative values. **a)** On the left, we have set $V_\text{b} = -3$ and $|V_\text{b}| > \omega_\lambda = 1$, so that there is a finite region (in gray) where both functions overlap. **b)** On the right, we have $V_\text{b} = -1$ and $|V_\text{b}| < \omega_\lambda = 3$, so that these two functions don't overlap, which leads to the integrand being zero for all possible values of ω. This means that the first term in Eq. **??** vanishes for boson energies ω_λ greater than the magnitude of the bias potential $|V_\text{b}|$.

The Heaviside step functions present in this equation modify the integration limits. In order to better understand how, we plot these factor in Fig.21

From Fig.21, we can see that the second term in Eq.2.93 can be rewritten as (assuming $\omega_\lambda < |V_\text{b}|$)

$$\sum_{\lambda,s=\pm1} q_e \int \frac{d\omega}{2\pi} \left[1 - f_L(\omega)\right] f_R(\omega - s\omega_\lambda) \left[sb(s\omega_\lambda)\right] \mathcal{T}_\text{inel}^{(\lambda,s)}(\omega) = \sum_\lambda q_e \int_{-|V_\text{b}|}^{-\omega_\lambda} \frac{d\omega}{2\pi} \mathcal{T}_\text{inel}^{(\lambda,-1)}(\omega) \tag{3.65}$$

Resulting inelastic current

From these past few considerations regarding the terms of the integral in Eq. 2.93, we are now in the position to substantially simplify that expression for $T = 0K$ as

$$\begin{aligned} J_\text{inel}^{(2)}\Big|_{T=0} = &\sum_\lambda q_e \int_{\omega_\lambda}^{V_\text{b}} \frac{d\omega}{2\pi} \mathcal{T}_\text{inel}^{(\lambda,+1)}(\omega) \\ &- \sum_\lambda q_e \int_{-|V_\text{b}|}^{-\omega_\lambda} \frac{d\omega}{2\pi} \mathcal{T}_\text{inel}^{(\lambda,-1)}(\omega) \end{aligned} \tag{3.66}$$

The first term in Eq. 3.66 corresponds to the inelastic current at $T = 0K$ arising when we apply a positive bias voltage $V_\text{b} > 0$, whereas the second term corresponds to the current for a negative bias voltage $V_\text{b} < 0$.

Thus, this equation states that the total current flowing from the left to the right contact is equal to the current flowing in the $L \to R$ direction (from applying a positive V_b) minus the current flowing in the $R \to L$ direction (from applying a negative V_b).

We can separate Eq. 3.66 in cases as follows

$$J_\text{inel}^{(2)}\Big|_{T=0} = \begin{cases} \sum_\lambda q_e \int_{\omega_\lambda}^{V_\text{b}} \frac{d\omega}{2\pi} \mathcal{T}_\text{inel}^{(\lambda,+1)}(\omega) & \text{, for } V_\text{b} > \omega_\alpha > 0 \\ -\sum_\lambda q_e \int_{-|V_\text{bias}|}^{-\omega_\lambda} \frac{d\omega}{2\pi} \mathcal{T}_\text{inel}^{(\lambda,-1)}(\omega) & \text{, for } V_\text{b} < 0 \text{ and } \omega_\alpha < |V_\text{b}| \\ 0 & \text{, for } V_\text{b} = 0 \text{ or } \omega_\alpha > |V_\text{b}| \end{cases} \tag{3.67}$$

which is plotted in Fig. 22, where the integral over ω was numerically calculated.

Starting with the left plot of Fig. 22 that shows the variation of $J_\text{inel}^{(2)}$ with V_b, we remark that as in the previous sections, for $V_\text{b} < \varepsilon_0$ the inelastic current is also zero and it dramatically increases around $V_\text{b} = \varepsilon_0$. However, contrarily to the the zeroth order coherent current $J_\text{el}^{(0)}$ which stabilizes for $V_\text{b} > \varepsilon_0$, the inelastic current $J_\text{inel}^{(2)}$ has another rise at $V_\text{b} = \varepsilon_0 + \omega_\lambda$ and only then it stabilizes into a plateau. This happens because, as can be seen in Fig. 19, the inelastic transmission function $\mathcal{T}_\text{inel}^{(2)}$ has two peaks, one at $\omega = \varepsilon_0$ and the other at $\omega = \varepsilon_0 + s\omega_\lambda$, which arises due to the electron-boson interaction that we

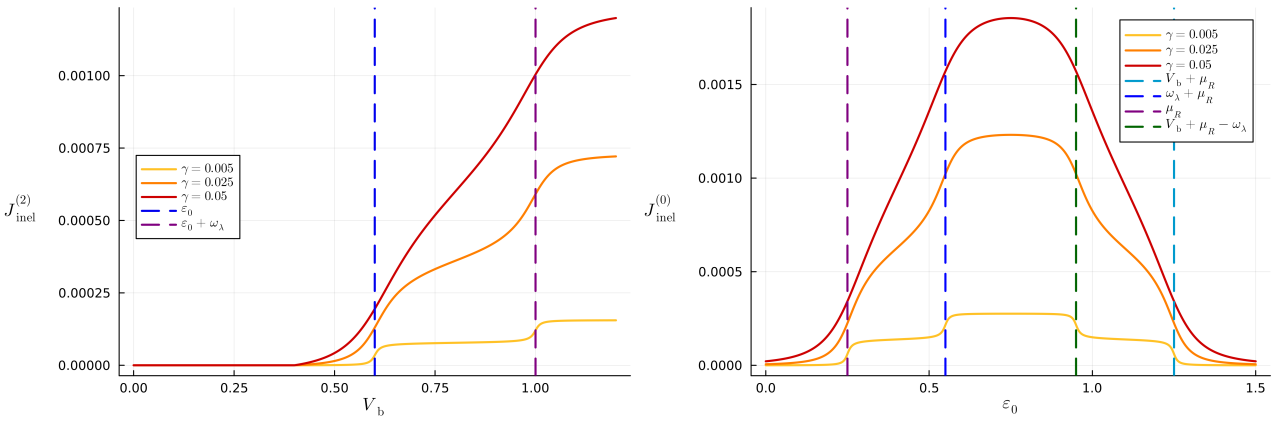


Figure 22: Plot of $J^{(2)}_{\text{inel}}$ vs. V_b (left) and $J^{(2)}_{\text{inel}}$ vs. ε_0 (right) at $T = 0$ in the WBL regime for $\gamma = 0.005$ (yellow), 0.025 (orange) and 0.05 (red). **Left:** We have set $\varepsilon_0 = 0.6$, $\omega_\lambda = 0.4$, $M_\lambda = 0.1$ and $\mu_R = 0$, and the vertical lines were plotted at $V_b = \varepsilon_0$ (blue) and $V_b = \varepsilon_0 + \omega_\lambda$ (purple), respectively, corresponding to the regions where the current increases abruptly. These regions where $J^{(2)}_{\text{inel}}$ suddenly rises are broadened with increasing γ. This is occurs since we are integrating $\mathcal{T}^{(\lambda,s)}_{\text{inel}}$ (Eq.3.57) which displays two peaks that have width γ. **Right:** For this plot we have set $\mu_R = 0.2$ for visual purposes, $V_b = 0.5$ and $\omega_\lambda = 0.3$. For $\varepsilon_0 < \mu_R$ the current is zero but when ε_0 reaches the same value as μ_R it experiences an abrupt increase which is maintained in the region $\mu_R < \varepsilon_0 < \mu_R + \omega_\lambda$. Additionally, at $\varepsilon_0 = \omega_\lambda + \mu_R$ it experiences another increase, which is then canceled at $\varepsilon_0 = V_b - \omega_\lambda + \mu_R$ by a decrease of the same amount. As in the case of $J^{(0)}_{\text{el}}$, the inelastic current $J^{(2)}_{\text{inel}}$ experiences another sudden decrease at $\varepsilon_0 = \mu_R + V_b$ going back to zero.

have included in the central region. The first inelastic transmission/current channel is depicted in the left diagram of Fig. 23, corresponding to the transition of an electron with energy $\varepsilon_0 + \omega_\lambda$ located in the left lead to the central region, where it then decays to the ε_0 level by emitting a boson with energy ω_λ, and finally crosses to the right lead. The second channel is analogous to the first one, the difference being that the decay occurring in the central region is from the level ε_0 to $\varepsilon_0 - \omega_\lambda$, which is illustrated in the right diagram of Fig. 23. We also remark that since we are at $T = 0$, the number of bosons naturally present in the system is zero, which means that there could be only the emission and not the absorption of a boson in the central region. Therefore, transitions where the electron gains energy via the absorption of a boson such as $\varepsilon_0 \to \varepsilon_0 + \omega_\lambda$ or $\varepsilon_0 - \omega_\lambda \to \varepsilon_0$ cannot occur, and the only inelastic process possible is the emission of bosons.

As for the right plot of Fig. 22, it shows the variation of $J^{(2)}_{\text{inel}}$ with ε_0 (with fixed V_b) and the reasoning is the same as before. For $\varepsilon_0 < \mu_R$ there is no current, but once it approaches μ_R the decaying channel $\varepsilon_0 + \omega_\lambda \to \varepsilon_0$ is enabled and now the electrons can undergo the path

$$\mu_L \to \varepsilon_0 + \omega_\lambda \underset{\text{emission}}{\to} \varepsilon_0 \to \mu_R \tag{3.68}$$

as depicted in the top diagram of Fig. 23. The current stabilizes into a plateau until ε_0 reaches values around $\mu_R + \omega_\lambda$, where the inelastic current experiences a new rise due to the opening of the second decaying channel $\varepsilon_0 \to \varepsilon_0 - \omega_\lambda$, where the electrons follow the path

$$\mu_L \to \varepsilon_0 \underset{\text{emission}}{\to} \varepsilon_0 - \omega_\lambda \to \mu_R,$$

which is illustrated in the bottom diagram of Fig. 23. The inelastic current has its maximum value in the interval $\omega_\lambda + \mu_R < \varepsilon_0 < V_\text{b} + \mu_R - \omega_\lambda$ and starts to decrease around $\varepsilon_0 = V_\text{b} + \mu_R - \omega_\lambda$, since for those values the energy level $\varepsilon_0 + \omega_\lambda$ becomes larger than μ_L, disabling the flow of electrons from the left lead to that same level, only remaining the decaying channel $\varepsilon_0 \to \varepsilon_0 - \omega_\lambda$. As we continue to increase ε_0 we reach the point $\varepsilon_0 = V_b + \mu_R$ where the current goes to zero again because ε_0 is now larger than the Fermi level of the left lead μ_L, also disabling the decaying channel $\varepsilon_0 \to \varepsilon_0 - \omega_\lambda$.

It is also worth of mentioning that, as in the previous sections, the level width γ plays a significant role in the processes here described by controlling the width of the regions where the current increases/-decreases, and also contributing to the height of the curves. As explained before, these attributes come from the fact that γ controls the coupling between the leads and the central region.

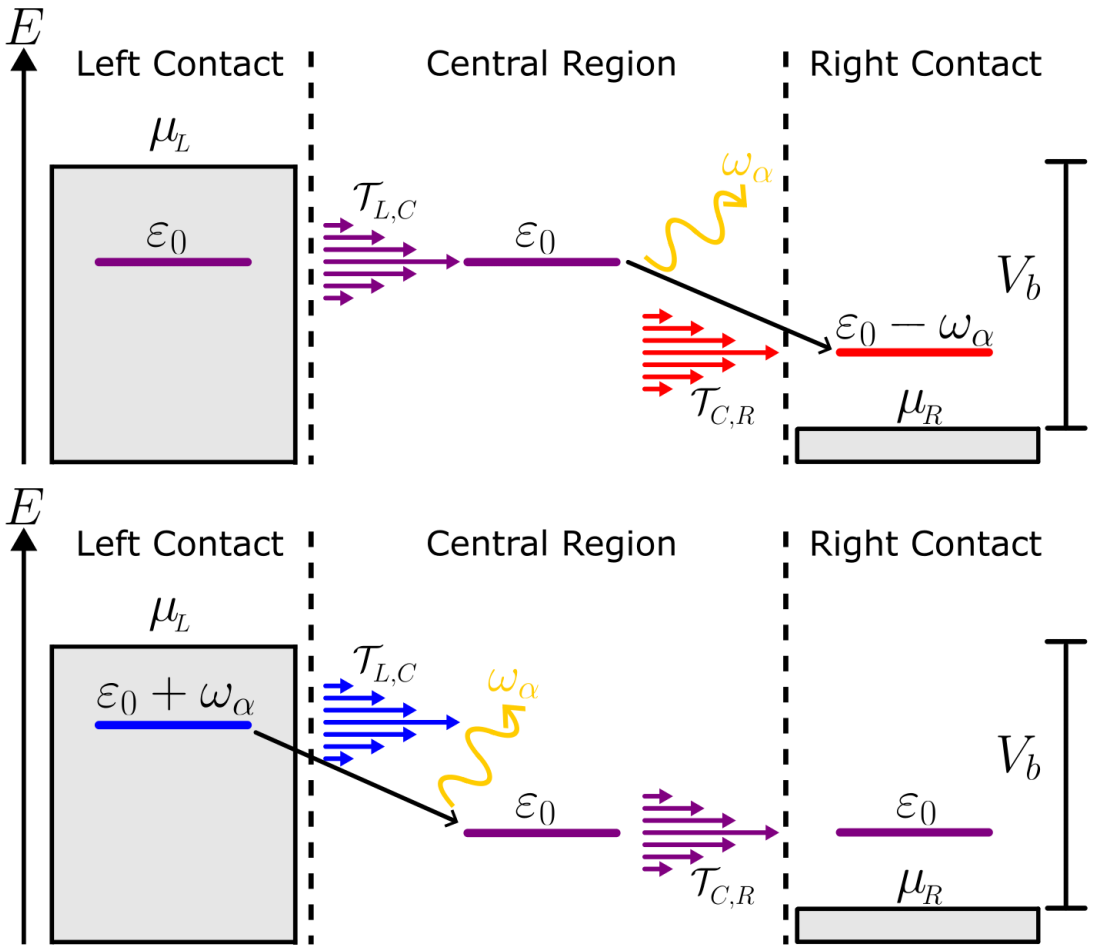


Figure 23: Fermi diagrams of the two decaying channels that come into play in the inelastic current $J^{(2)}_{\text{inel}}$. In both diagrams, the Fermi levels of the contacts are represented by the grey columns that are labeled as μ_L for the left contact and μ_R for the right one, which are shifted from each other by an amount V_b that is an externally controlled bias voltage. In between the Fermi levels of the contact is the energy level ε_0 (purple). **Top:** An electron from the left lead with energy ε_0 (purple) elastically crosses to the central region, where it tunnels inelastically to the level $\varepsilon_0 - \omega_\lambda$ (red) of the right lead by the emitting a boson with energy ω_λ (curly yellow arrow). **Bottom:** Same as the left diagram, the difference being that an electron with energy $\varepsilon_0 + \omega_\lambda$ (blue) goes from the left lead to the to the level ε_0 (purple) in the central region by emitting a boson and then it elastically crosses to the right lead. The horizontal arrows represent the peaks of the transmission function, which have a width γ (not to scale).

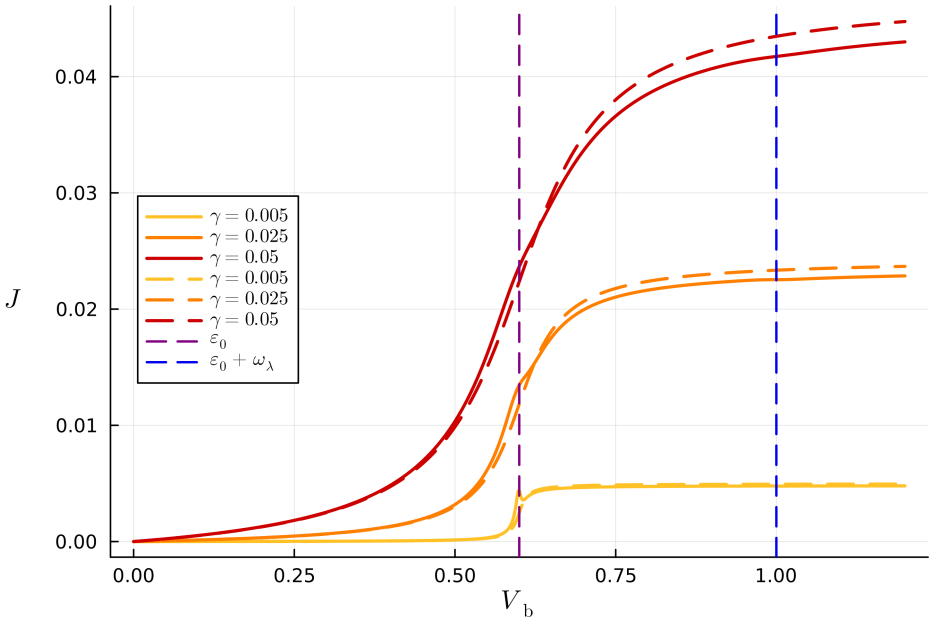


Figure 24: Plot of the total current J_{tot} (solid lines) up to $|M_\lambda|^2$ that flow in the system at $T = 0$ in the WBL regime for $\varepsilon_0 = 0.6$, $\mu_R = 0$, $\omega_\lambda = 0.4$ and $M_\lambda = 0.3$, with $\gamma = 0.005$ (yellow), 0.025 (orange) and 0.05 (red). For comparison we also show the correspondent zero-th order current $J_{\text{el}}^{(0)}$ (dashed lines). The vertical dashed lines were plotted at $V_{\text{b}} = \varepsilon_0$ (purple) and $V_{\text{b}} = \varepsilon_0 + \omega_\lambda$ (blue), respectively, corresponding to the regions where the current displays important features.

3.5 Discussion

To conclude this chapter, we show the total current J_{tot} up to $|M_\lambda|^2$ in Fig.24, where we compare it to the zero-th order current $J_{\text{el}}^{(0)}$ that does not account for interactions.

We remark that accounting for interactions in the system leads to modifications in the current. It is slightly increased around $V_{\text{b}} = \varepsilon_0$, which is followed by a considerable suppression for higher values of V_{b}. The magnitude of this suppression highly depends on $|M_\lambda|^2$, and the determination of this matrix element is considered in the next chapter (in the context of the 3D system of Fig. 1).

In Fig. 25 we show the different contributions to the current. It should be noted that the contribution from the interactions, present in the bottom-right panel, is dominated by the elastic correction although the inelastic contribution also plays a role. Notice that, for $V_{\text{b}} < \varepsilon_0$, the interactions lead to an increase in the total current, while for $V_{\text{b}} > \varepsilon_0$ their effect is the opposite.

We now proceed to contrast the presented results with the experimental results of Tsui *et al.* [161]. In their work, a peak in the I-V curve was observed corresponding to elastic resonant tunneling and another smaller peak that was shifted from the former by an amount that they attributed to the energy of LO-

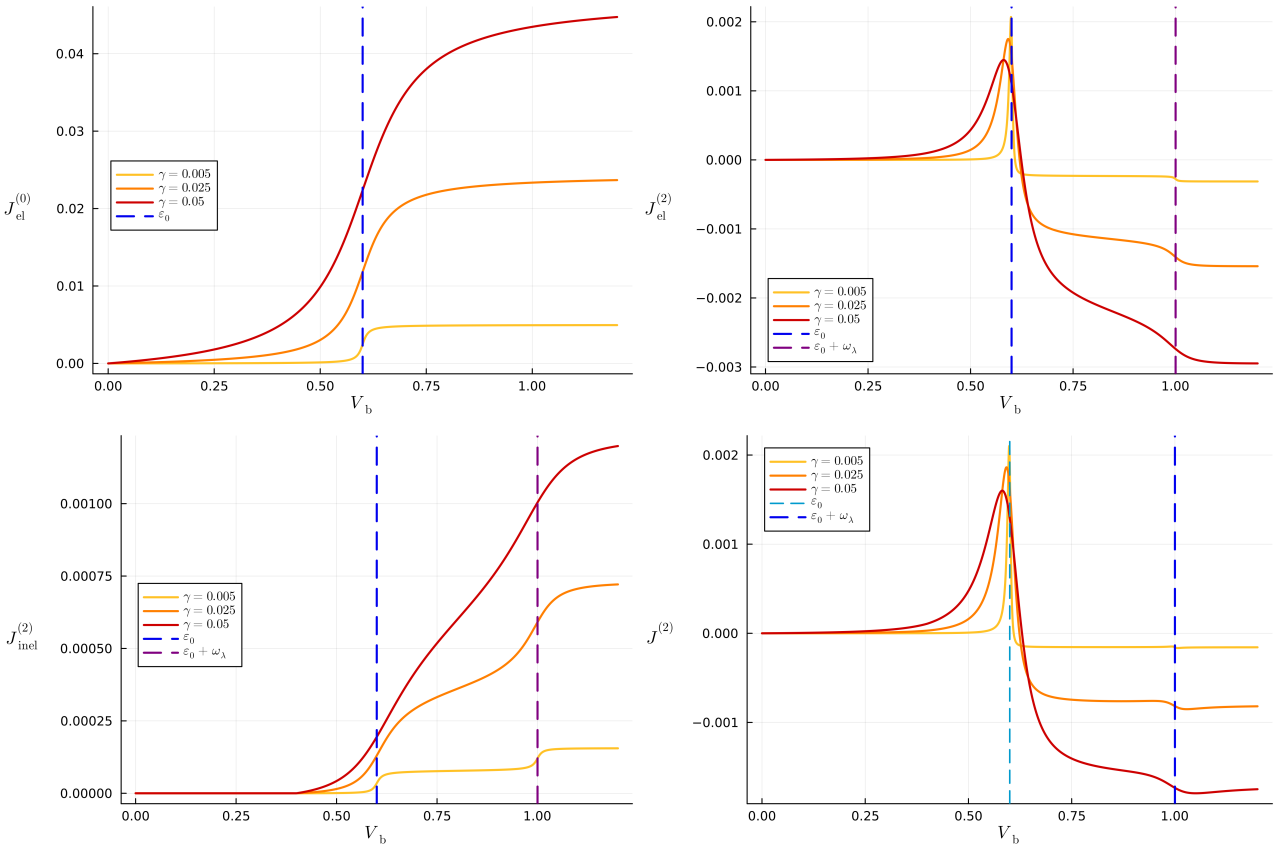


Figure 25: **Top-left:** Plot of the zeroth order elastic current $J^{(0)}_{\text{el}}$ vs. the bias voltage V_{b} in the WBL at $T = 0$ for $\varepsilon_0 = 0.6$, $\mu_R = 0$, $\omega_\lambda = 0.4$ and $M_\lambda = 0.1$, with $\gamma = 0.005$, 0.025 and 0.05. The same parameters were used in all the four images. **Top-right:** Plot of the second order elastic current $J^{(2)}_{\text{el}}$ vs. the bias voltage V_{b}. **Bottom-left:** Plot of the second order inelastic current $J^{(2)}_{\text{inel}}$ vs. the bias voltage V_{b}. **Bottom-right:** Plot of the second order contribution to the current $J^{(2)}_{\text{el}} + J^{(2)}_{\text{inel}}$ vs. the bias voltage V_{b}.

phonons. Additionally, they reported that the ratio between the inelastic and elastic peaks was about 0.04. However, in our model there are no peaks in the current due to the WBL approximation that we used. Indeed, the drop of $I\left(V_{\mathrm{b}}\right)$ at $V_{\mathrm{b}} \approx -0.2$ V in Fig. 5 arises from the matching of the resonant energy level (E_0) with the bottom of the conduction band in the left contact, which simply does not exist in our model.

Nonetheless, we can compare the relative magnitudes of the elastic and inelastic currents calculated within our model. In the limit of high voltages (where there are no more relevant features left unaccounted) we have obtained a ratio $J_{\mathrm{inel}}^{(2)}/J_{\mathrm{el}}^{(0)}$ of 0.012. In order to get closer of the experimentally obtained value of 0.04, we could increase the independent variable M_λ by a factor of 2 (which would yield an increase in $J_{\mathrm{inel}}^{(2)}$ by a factor of 4 since it quadratically depends on M_λ), from 0.1 to 0.2.

Another quantity that is relevant in this study is the differential conductivity dJ/dV_{b}, which is shown in Fig. 26. In order to have a better view at the feature that arises for $V_{\mathrm{b}} = \omega_\lambda$, we also calculate the second derivative of the current, which is present in Fig. 27.

To conclude this chapter, we notice that, when accounting for the interactions, a new tunneling channel is opened at $V_{\mathrm{b}} = \omega_\lambda$. This is a general feature that arises in many tunneling problems [129, 161] and it is the concept for a type of spectroscopy that measures the energy of the bosons (or other resonant entities) existing in the system, which is known as Inelastic Electron Tunneling Spectroscopy (IETS) [163, 164].

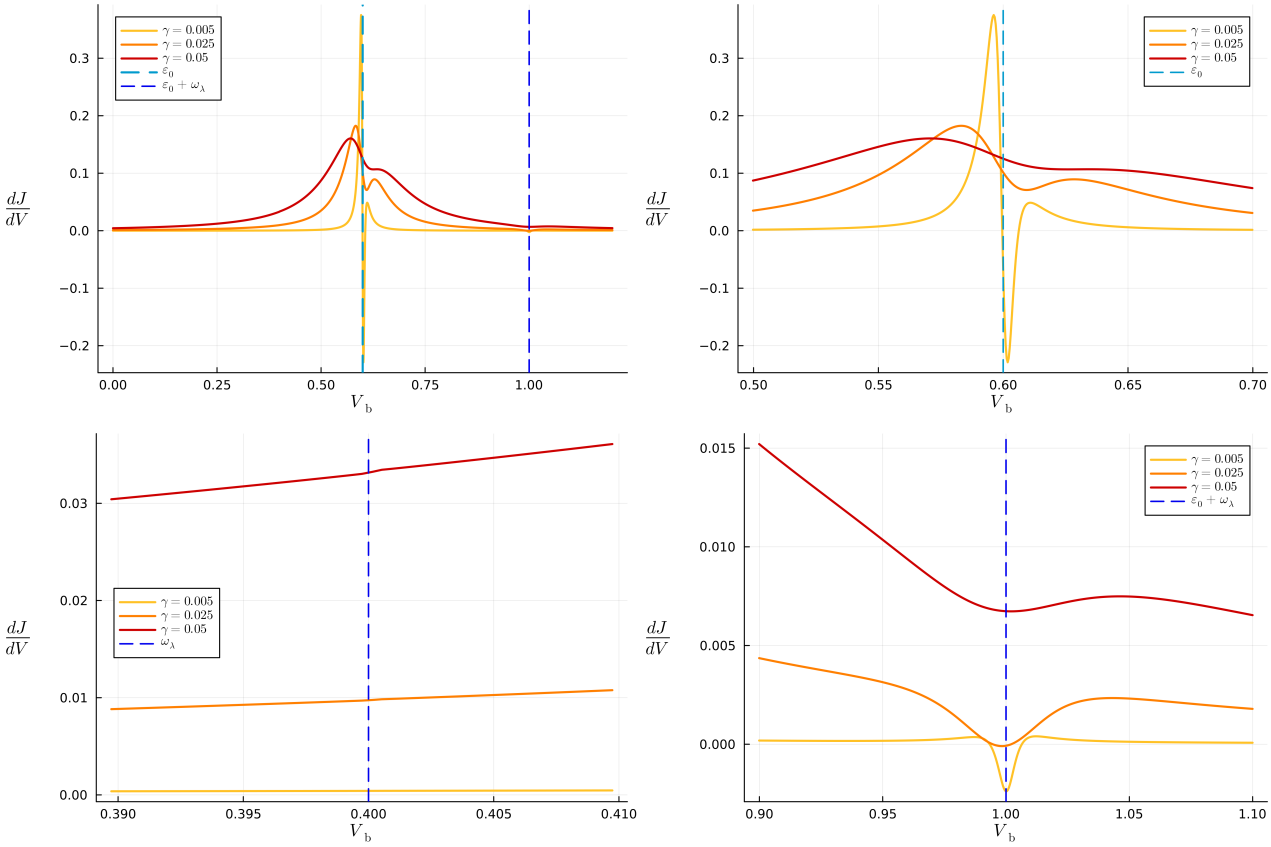


Figure 26: Plot of the differential conductivity dJ/dV_b vs. V_b for $\varepsilon_0 = 0.6$, $\mu_R = 0$, $\omega_\lambda = 0.4$ and $M_\lambda = 0.3$, with $\gamma = 0.005$ (yellow), 0.025 (orange) and 0.05 (red). **Top left:** Plot over the whole range of V_b. Most of the relevant features are around $V_b = \varepsilon_0$, although there is also a small detail at $V_b = \varepsilon_0 + \omega_\lambda$. **Top right:** Zoom around $V_b = \varepsilon_0$. **Bottom left:** Zoom around $V_b = \omega_\lambda$. Although barely visible, there are some small features in this region that are better captured by the second derivative. **Bottom right:** Zoom around $V_b = \varepsilon_0 + \omega_\lambda$. Although smaller than the central features, there are also some details in this region due to the electron-boson interactions.

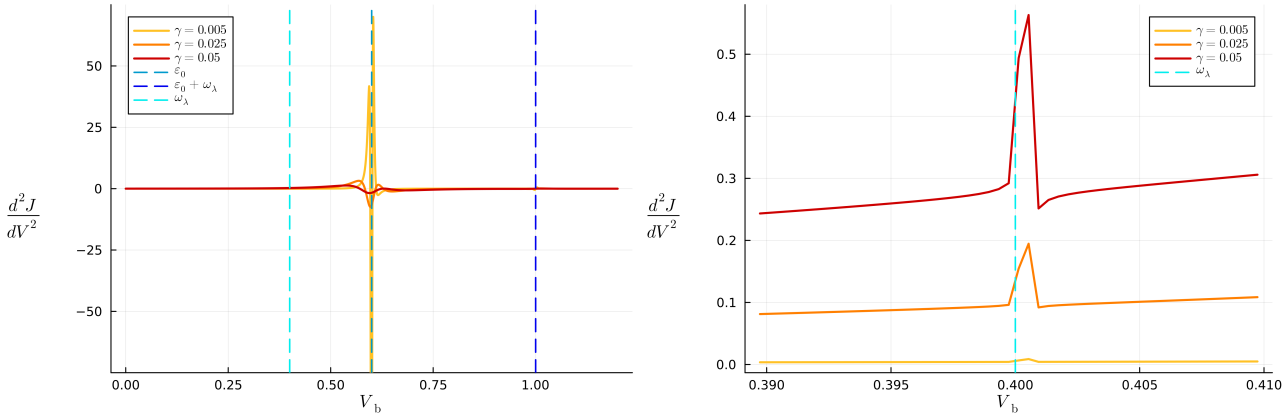


Figure 27: Plot of the second derivative of the current d^2J/dV_b^2 vs. V_b for $\varepsilon_0 = 0.6$, $\mu_R = 0$, $\omega_\lambda = 0.4$ and $M_\lambda = 0.3$, with $\gamma = 0.005$ (yellow), 0.025 (orange) and 0.05 (red). **Left:** Plot over the whole range of V_b. The relevant features are around $V_b = \varepsilon_0$, although there is also a small detail at $V_b = \varepsilon_0 + \omega_\lambda$. **Right:** Zoom around $V_b = \omega_\lambda$. It is now visible the signature left by the bosons, given by the peak around their energy.

Chapter 4

Second-order perturbation theory for the 3D device

We now move forward from the toy-model perspective, which was the focus of the previous chapter, to the study of the device based on the vdW structure schematically presented in Fig. 1.

Particularly, in this chapter we tackle the problem left open in the previous chapter of finding the suitable interaction matrix element M_λ, specifically for the electron-exciton interaction, via second order perturbation theory. The explicit expression for this quantity allows us to obtain more accurate results when we employ the idealized 1D system previously studied as a model for the tunneling current flowing through the gr-hBN-gr + TMD system. Additionally, by direct application of this quantity into Fermi's Golden Rule, we obtain transition rates and the probability for the exciton assisted electron tunneling to occur.

4.1 Microscopic processes and Hamiltonians

4.1.1 Preliminary remarks

In this chapter, our aim is to tackle the problem of finding an explicit expression for the probability (per unit time) of tunneling between two graphene sheets, assisted by generation of excitons in the nearby TMD layer, considering the structure of Fig. 1. The approach consists in using Fermi's Golden Rule, which is conceptually simpler than the NEGF formalism while still yielding a good description of the tunneling process, including both the cases of elastic and inelastic tunneling [165, 133, 166, 167, 132]. In this approach, the pivotal quantities to be calculated are the matrix elements of the elementary processes involved, namely, (i) electron transition between two states that belong to the different graphene sheets, accompanied by the emission of a virtual photon, and (ii) absorption of this photon by the TMD layer with its transition between two excitonic states (one of them typically being the exciton vacuum). These constitute a globally second-order process (with two interactions) and we are interested in this second-order matrix element.

We highlight the fact that we are dealing with different physical particles, these being the electrons in the graphene sheets, the virtual photons that propagate from the gr-hBN-gr system to the TMD, and the excitons in the TMD. Therefore, the quantities describing the "global" system (states, Hamiltonians, etc...) must encode the Hilbert space of these three different entities. This is made possible by writing the "global" states as outer products of the individual particle states, such as

$$|s\rangle = |\boldsymbol{K}_\ell\rangle \otimes |n_{\boldsymbol{q}\lambda}\rangle \otimes |n_{\text{ex}}, \boldsymbol{k}\rangle \tag{4.1}$$

where $|\boldsymbol{K}_\ell\rangle$ describes an electron with wave-vector $\boldsymbol{K} = \boldsymbol{k} + \kappa_z$ in the $\ell = L, R$ graphene ($\boldsymbol{k}$ is the in-plane component and κ_z the out-of-plane component), $n_{\boldsymbol{q}\lambda}$ is the number of photons with momentum $\boldsymbol{q}$ and polarization λ in the system and $|n_{\text{ex}}, \boldsymbol{k}\rangle$ describes the n-th hydrogenoic state (with the corresponding effective mass and Bohr's radius [168, 169]) in which the exciton with $\boldsymbol{k}$ CM momentum is. Such state can be written simply as

$$|s\rangle = |\boldsymbol{K}_\ell\rangle\, |n_{\boldsymbol{q}}\rangle\, |n_{\text{ex}}, \boldsymbol{k}\rangle \tag{4.2}$$

where the outer products between the individual states is implied.

Also, we write the Hamiltonian governing this system as

$$H = H_0 + H_{\text{int}} \tag{4.3}$$

where the unperturbed Hamiltonian H_0 is simply given by the sum of the independent particle Hamiltonians for the electrons H_e, the photons H_{ph} and the excitons H_{ex} such that

$$H_0 = H_{\text{e}} \otimes \mathbb{I}_{\text{ph}} \otimes \mathbb{I}_{\text{ex}} + \mathbb{I}_{\text{e}} \otimes H_{\text{ph}} \otimes \mathbb{I}_{\text{ex}} + \mathbb{I}_{\text{e}} \otimes \mathbb{I}_{\text{ph}} \otimes H_{\text{ex}} \tag{4.4}$$

which can simply be written as (where the outer products with the identity of the Hilbert subspace of each particle is implied)

$$H_0 = H_{\text{e}} + H_{\text{ph}} + H_{\text{ex}} \tag{4.5}$$

and the interacting Hamiltonian is given by the electron-photon interaction $H_{\text{e-ph}}$ and by the exciton-photon interaction $H_{\text{ph-ex}}$ such that

$$H_{\text{int}} = H_{\text{e-ph}} \otimes \mathbb{I}_{\text{ex}} + \mathbb{I}_{\text{e}} \otimes H_{\text{ph-ex}} \tag{4.6}$$

with $H_{\text{e-ph}}$ and $H_{\text{ph-ex}}$ acting at $z = 0$ and $z = a + b$, respectively.

To tackle the problem of obtaining an explicit expression for the matrix element for the electron-exciton interaction occurring between the tunneling electron and the excitons in the TMD, which from now on we denote as $M_{i\to f}$, we use the second order time-dependent perturbation approach. While being extensively used throughout the literature and conceptually easy to understand, this approach captures the relevant

physical processes that we are interested in, provided that the perturbation in question - this being the interaction itself - is small enough in comparison to the other quantities that also come into play.

The following expression holds for the interaction matrix element [170]

$$M_{i\to f} = \sum_m \frac{\langle f| V_2 |m\rangle \langle m| V_1 |i\rangle}{E_i - E_m} \tag{4.7}$$

where $|i\rangle$, $|f\rangle$ are the initial and final states for this process with energies E_i and E_f, respectively, $|m\rangle$ are possible intermediate states of the system with energy E_m and $V_{1/2}$ is the interacting potential, which correspond to the interaction Hamiltonians $H_{\text{e-ph}}$ and $H_{\text{ph-ex}}$, where the order in which they act depends on the process labeled as m.

In order for this method to be applicable, it is assumed that the energy of the final state is equal (or at least approximately) to the energy of the initial state. This implies energy conservation by discarding possible losses due to other mechanisms, which we are not interested in.

Now, we need to elaborate on $H_{\text{e-ph}}$, $H_{\text{ph-ex}}$ and all these states that appear in Eq. 4.7.

4.1.2 Electron-photon interaction Hamiltonian $H_{\text{e-ph}}$

Focusing in $H_{\text{e-ph}}$, it describes the interaction between the electrons in the graphene sheets and the EM field. The Hamiltonian that governs the electronic behavior close to the Dirac point of graphene, where the electrons can be described as massless Dirac fermions, is given by

$$H_{\text{gr}} = v_F \boldsymbol{\sigma} \cdot \boldsymbol{p} \tag{4.8}$$

where v_F is the Fermi velocity of the electron in the graphene and $\boldsymbol{\sigma} = (\sigma_x, \sigma_y)$ is the 2D vector of Pauli matrices, also known as pseudo-spin (coming from the sub-lattice degree of freedom). In the presence of a vector potential $\boldsymbol{A}$, the momentum operator changes as $\boldsymbol{p} \to \boldsymbol{p} + e\boldsymbol{A}/c$ [171], introducing in the previous equation the following term

$$H_{\text{e-ph}} = \frac{ev_F}{c} \left[\boldsymbol{\sigma} \cdot \boldsymbol{A}\left(\boldsymbol{R}, t\right)\right] \tag{4.9}$$

which is the expression for the electron-photon interaction Hamiltonian in graphene (near the Dirac cones).

In turn, the vector potential of the electromagnetic (EM) field in its second-quantized form is given by [172]

$$\boldsymbol{A}\left(\boldsymbol{R}, t\right) = \sum_{\boldsymbol{q}\lambda} \boldsymbol{e}_{\boldsymbol{q}}^{\lambda} B_{\boldsymbol{q}} \left[a_{\boldsymbol{q}\lambda} e^{i(\boldsymbol{q}\cdot\boldsymbol{R} - \omega_{\boldsymbol{q}} t)} + a_{\boldsymbol{q}\lambda}^{\dagger} e^{-i(\boldsymbol{q}\cdot\boldsymbol{R} - \omega_{\boldsymbol{q}} t)}\right] \tag{4.10}$$

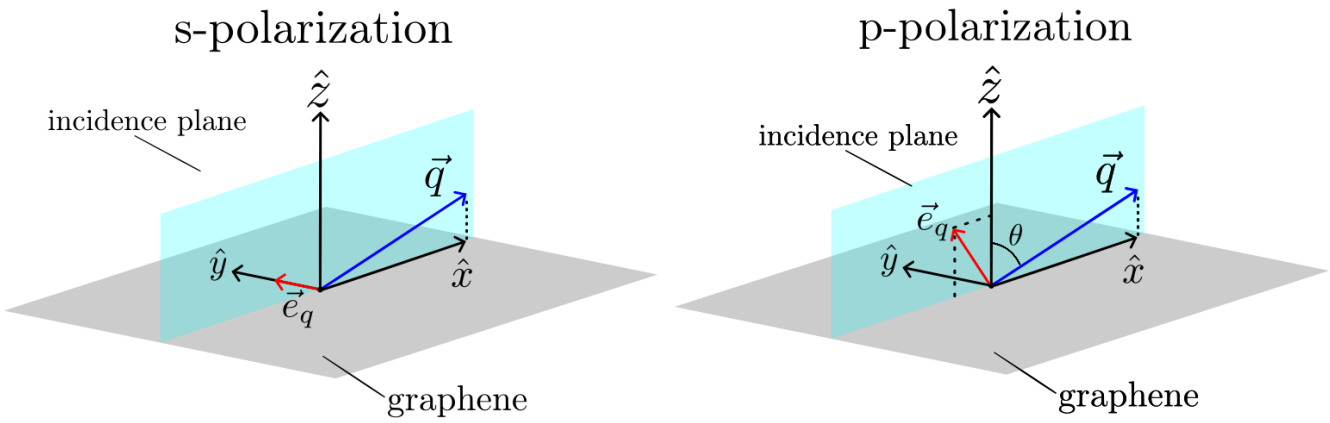


Figure 28: Sketch of the two different cases for the projection of $\boldsymbol{e_q}$ into the graphene's plane, depending on the polarization. The gray plane corresponds to the graphene sheet, perpendicular to the $\hat{z}$ axis, and in light blue is shown the incidence plane, perpendicular to the graphene, which includes the wave-vector $\boldsymbol{q}$ and the $\hat{z}$ axis. **Left:** For the s-polarization, $\boldsymbol{e_q}$ is perpendicular to $\boldsymbol{q}$ and to the plane of incidence. This means that $\boldsymbol{e_q}$ is always parallel to the graphene sheet. **Right:** For the p-polarization, $\boldsymbol{e_q}$ is also perpendicular to $\boldsymbol{q}$ but is parallel to the plane of incidence. If we set θ to be the angle between $\boldsymbol{q}$ and $\hat{z}$, then the projection of $\boldsymbol{e_q}$ into the graphene's plane is $\cos(\theta) = q_z/q$.

where

$$B_{\boldsymbol{q}} = \left(\frac{2\pi\hbar c^2}{V\omega_{\boldsymbol{q}}\eta^2}\right)^{1/2} \tag{4.11}$$

with $\boldsymbol{R}$ being a 3D position vector, $\boldsymbol{e_q}$ the polarization vector, $\omega_q = cq/\eta$ the frequency (energy) of a photon with wave-vector $\boldsymbol{q}$, η the refraction index of the environment (in our case hBN), V is the volume of the "box" where the EM field was quantized on (which will cancel later on), λ is the polarization index, and $a_{\boldsymbol{q}\lambda}$ ($a^\dagger_{\boldsymbol{q}\lambda}$) is the annihilation (creation) operator for the photons with momentum $\boldsymbol{q}$ and polarization λ.

Therefore, the electron photon interacting Hamiltonian is given by

$$H_{\text{e-ph}} = \frac{ev_F}{c}\sum_{\boldsymbol{q},\lambda} B_{\boldsymbol{q}}\left[a_{\boldsymbol{q}}e^{i(\boldsymbol{q}\cdot\boldsymbol{R}-\omega_q t)} + a^\dagger_{\boldsymbol{q}}e^{-i(\boldsymbol{q}\cdot\boldsymbol{R}-\omega_q t)}\right]\boldsymbol{e}^\lambda_{\boldsymbol{q}}\cdot\sigma \tag{4.12}$$

where we need to take into account the two possible polarizations of the electromagnetic field that are represented by the index λ, which are shown in Fig. 28.

4.1.3 Exciton-photon interaction Hamiltonian $H_{\text{ph-ex}}$

We now proceed to $H_{\text{ph-ex}}$, which in the dipole approximation can be written as [173]

$$H_{\text{ph-ex}} = -\boldsymbol{d}_{\text{cv}} \cdot \boldsymbol{E} \tag{4.13}$$

with $\boldsymbol{d}_{\text{cv}}$ being the dipole moment matrix element between the conduction and valence bands of the TMD that is given by

$$\boldsymbol{d}_{\text{cv}} = \frac{d_{\text{cv}}}{\sqrt{2}} \left(\boldsymbol{e}_x \pm i\boldsymbol{e}_y\right) \tag{4.14}$$

where the $\pm$ sign corresponds to the K and K' points of the TMD's Brillouin zone and the magnitude d_{cv} is a characteristic parameter of the material (TMD). The in-plane electric field $\boldsymbol{E}$ can be obtained from the vector potential $\boldsymbol{A}$ (Eq. 4.10) as

$$\begin{aligned} \boldsymbol{E} &= -\frac{1}{c}\frac{\partial}{\partial t}\boldsymbol{A} \\ &= \frac{i}{c}\sum_{\boldsymbol{q}\lambda} \omega_{\boldsymbol{q}} \boldsymbol{e}_{\boldsymbol{q}}^{\lambda} B_{\boldsymbol{q}} \left[a_{\boldsymbol{q}\lambda} e^{i(\boldsymbol{q}\cdot\boldsymbol{R}-\omega_{\boldsymbol{q}}t)} - a_{\boldsymbol{q}\lambda}^{\dagger} e^{-i(\boldsymbol{q}\cdot\boldsymbol{R}-\omega_{\boldsymbol{q}}t)}\right] \end{aligned} \tag{4.15}$$

which points in the same direction as $\boldsymbol{A}$.

Therefore, in the dipole approximation we have

$$H_{\text{ph-ex}} = \frac{i}{c}\sum_{\boldsymbol{q}\lambda} \omega_{\boldsymbol{q}} \left(\boldsymbol{d}_{\text{cv}} \cdot \boldsymbol{e}_{\boldsymbol{q}}^{\lambda}\right) B_{\boldsymbol{q}} \left[a_{\boldsymbol{q}\lambda} e^{i(\boldsymbol{q}\cdot\boldsymbol{R}-\omega_{\boldsymbol{q}}t)} - a_{\boldsymbol{q}\lambda}^{\dagger} e^{-i(\boldsymbol{q}\cdot\boldsymbol{R}-\omega_{\boldsymbol{q}}t)}\right] \tag{4.16}$$

where once again we need to account for the two possible polarizations depicted in Fig. 28.

4.1.4 Description of the states

Now, we focus on the states present in Eq. 4.7.

In light of the notation shown in Eq. 4.2, the initial state $|i\rangle$ is characterized by an electron with momentum $\boldsymbol{K}_L$ in the left graphene, no excitons in the TMD and also no photons in the system, which can be written as

$$|i\rangle = |\boldsymbol{K}_L\rangle \, |0_{\boldsymbol{q}\lambda}\rangle \, |0_{\text{ex}}\rangle \tag{4.17}$$

where $|0_{\text{ex}}\rangle$ is the excitonic vacuum state.

Likewise, the final state $|f\rangle$ is characterized by an electron with momentum $\boldsymbol{K}_R$ in the right graphene, an exciton with CM momentum $\boldsymbol{k}$ being in the n state on the TMD and also no photons in the system, which can be expressed as

$$|f\rangle = |\boldsymbol{K}_R\rangle \, |0_{\boldsymbol{q}\lambda}\rangle \, |1_{\boldsymbol{k}_{\text{ex}}}\rangle \tag{4.18}$$

As for the intermediate states encoded in the label m, in second order perturbation theory these correspond to two different processes, depicted in Fig. 29.

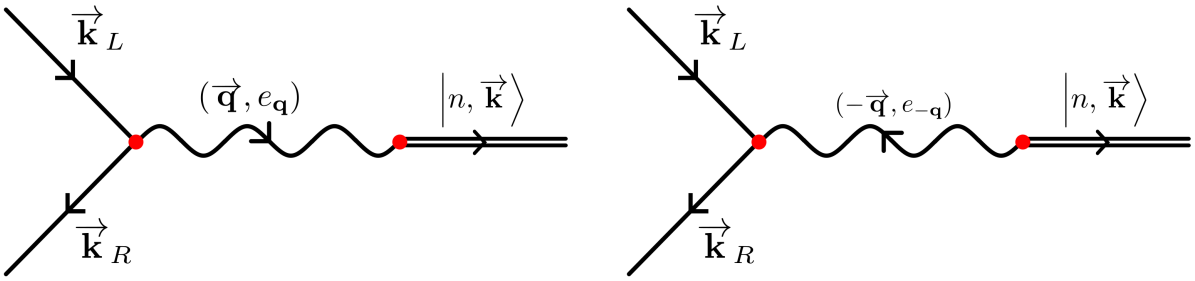


Figure 29: Feynman diagrams for the two possible interactions in the second-order perturbation theory. The straight single lines represent the electron propagator, the wobbly line the photon propagator and the straight double line the exciton propagator. The red dots correspond to the interaction vertices. **Left:** An electron with momentum $\boldsymbol{k}_L$ emits a photon with momentum $\boldsymbol{q}$ and polarization $e_{\boldsymbol{q}}$ and decays to a state with momentum $\boldsymbol{k}_R$. In turn, the emitted photon is responsible for exciting and exciton in the TMD with momentum $\boldsymbol{k}$ and energy quantum number n. **Right:** This corresponds to the permutation of the interactions present in the left diagram. Here, an exciton in the state $|n, \boldsymbol{k}\rangle$ is spontaneously created in the TMD along with a photon with momentum $-\boldsymbol{q}$ and polarization $e_{-\boldsymbol{q}}$. This photon is then responsible for interacting with an electron with momentum $\boldsymbol{k}_L$ in the left graphene, leading to its decay into the state with momentum $\boldsymbol{k}_R$ in the right graphene.

The first process (left diagram of Fig. 29), which we label as $m = I_1$, corresponds to the decaying of the tunneling electron from the state $|\boldsymbol{k}_L\rangle$ in the left graphene into the state $|\boldsymbol{k}_R\rangle$ in the right graphene, with the emission of a virtual photon with momentum $\boldsymbol{q}_1$ that is responsible for the formation of an exciton in the state $|n, \boldsymbol{k}\rangle$ in the neighboring TMD. The intermediate state $|I_1\rangle$ corresponding to this process is characterized by the electron already being in the state $|\boldsymbol{K}_R\rangle$ in the right graphene, while the photon that was emitted from that decay is still propagating and has not been absorbed yet by the exciton. Such a state is given by

$$|I_1\rangle = |\boldsymbol{K}_R\rangle \left|1_{\boldsymbol{q}_1\lambda_1}\right\rangle |0_{\text{ex}}\rangle \tag{4.19}$$

and can be interpreted as the state in which the system is after the electron transition but before the absorption of the photon by the exciton

The second process, which we label as $m = I_2$, corresponds to the same decay of the tunneling electron, but now a pair composed by a virtual photon with momentum $-\boldsymbol{q}$ and an exciton in the state $|n_{\text{ex}}, \boldsymbol{k}_{\text{ex}}\rangle$ is formed in the TMD. The formation of such a pair, although with an expected low probability, respects the conservation of momentum but momentarily breaks energy conservation, hence the low probability. The intermediate state $|I_2\rangle$ is then characterized by the exciton and the photon in the states $|n_{\text{ex}}, \boldsymbol{k}_{\text{ex}}\rangle$ and $\left|1_{\boldsymbol{q}_2}\right\rangle$, respectively. As before, the photon is the mediator of the electronic transition

between the graphene sheets. However, at this point it has not yet reached the graphene sheet in order for the electron to decay, meaning that the electron is in the state $|\boldsymbol{K}_L\rangle$. Therefore, this state is given by

$$|I_2\rangle = |\boldsymbol{K}_L\rangle \left|1_{\boldsymbol{q}_2\lambda_2}\right\rangle |1_{\boldsymbol{k}_{\text{ex}}}\rangle \tag{4.20}$$

4.2 Calculation of the second-order matrix element $M_{i\to f}$

We proceed our analysis by pointing out that the label m in Eq. 4.7 corresponds to the two different possible processes that can occur in the second-order perturbation scheme that we are developing here, that is, it encodes the processes depicted in Fig. 29, which we label as $m = 1$ and $m = 2$, respectively. Therefore, we have

$$\begin{aligned} M_{i\to f} &= \sum_m \frac{\langle f| V_2^{(m)} |m\rangle \langle m| V_1^{(m)} |i\rangle}{E_i - E_m} \\ &= \sum_{\boldsymbol{q}\lambda} \left[\frac{\langle f| V_2^{(1)} |I_1\rangle \langle I_1| V_1^{(1)} |i\rangle}{E_i - E_1} + \frac{\langle f| V_2^{(2)} |I_2\rangle \langle I_2| V_1^{(2)} |i\rangle}{E_i - E_2} \right] \\ &= \sum_{\boldsymbol{q}\lambda} [M_1 + M_2] \end{aligned} \tag{4.21}$$

where the lower label in $V_{1/2}^{(m)}$ means that it is the first/second interaction occurring in the m-th process, so that

$$\begin{aligned} M_1 &= \frac{\langle f| V_2^{(1)} |I_1\rangle \langle I_1| V_1^{(1)} |i\rangle}{E_i - E_1} \\ &= \frac{\langle f| \mathbb{I}_{\text{e}} \otimes H_{\text{ph-ex}} |I_1\rangle \langle I_1| H_{\text{e-ph}} \otimes \mathbb{I}_{\text{ex}} |i\rangle}{E_i - E_1} \end{aligned} \tag{4.22}$$

and

$$\begin{aligned} M_2 &= \frac{\langle f| V_2^{(2)} |I_2\rangle \langle I_2| V_1^{(2)} |i\rangle}{E_i - E_2} \\ &= \frac{\langle f| H_{\text{e-ph}} \otimes \mathbb{I}_{\text{ex}} |I_2\rangle \langle I_2| \mathbb{I}_{\text{e}} \otimes H_{\text{ph-ex}} |i\rangle}{E_i - E_2} \end{aligned} \tag{4.23}$$

4.2.1 Direct process, M_1

Starting with the process M_1, we have

$$M_1 = \frac{\langle f| \mathbb{I}_{\text{e}} \otimes H_{\text{ph-ex}} |I_1\rangle \langle I_1| H_{\text{e-ph}} \otimes \mathbb{I}_{\text{ex}} |i\rangle}{E_i - E_1} \tag{4.24}$$

The terms in the denominator are

$$E_1 = \hbar v_F k_R + \hbar\omega_q \tag{4.25}$$

and

$$E_i = \hbar v_F k_L + eV_b \tag{4.26}$$

so that the denominator reads

$$E_i - E_1 = \hbar v_F \left(k_L - k_R\right) + eV_b - \hbar\omega_q \tag{4.27}$$

As for the numerator, the matrix element for the electron-photon interaction is given by

$$\begin{aligned}\left\langle I_1\right| H_{\text{e-ph}} \otimes \mathbb{I}_{\text{ex}} \left|i\right\rangle &= \left\langle 0_{\text{ex}}\right| \left\langle 1_{\boldsymbol{q}_1\lambda_1}\right| \left\langle \boldsymbol{K}_R\right| H_{\text{e-ph}} \otimes \mathbb{I}_{\text{ex}} \left|\boldsymbol{K}_L\right\rangle \left|0_{\boldsymbol{q}\lambda}\right\rangle \left|0_{\text{ex}}\right\rangle \\ &= \frac{ev_F}{c} \sum_{\boldsymbol{q}\lambda} B_{\boldsymbol{q}} \left\langle 1_{\boldsymbol{q}_1\lambda_1}\right| \left\langle \boldsymbol{K}_R\right| \left[a_q e^{i\left(\boldsymbol{q}_\parallel \cdot \boldsymbol{r} + q_z z\right)} + a_q^\dagger e^{-i\left(\boldsymbol{q}_\parallel \cdot \boldsymbol{r} + q_z z\right)}\right] \boldsymbol{e}_{\boldsymbol{q}}^\lambda \cdot \boldsymbol{\sigma} \left|\boldsymbol{K}_L\right\rangle \left|0_{\boldsymbol{q}}\right\rangle \\ &= \frac{ev_F}{c} B_{\boldsymbol{q}} \left\langle \boldsymbol{K}_R\right| e^{-i\left(\boldsymbol{q}_\parallel \cdot \boldsymbol{r} + q_z z\right)} \boldsymbol{e}_{\boldsymbol{q}}^\lambda \cdot \boldsymbol{\sigma} \left|\boldsymbol{K}_L\right\rangle\end{aligned} \tag{4.28}$$

The state $\left|\boldsymbol{K}_\ell\right\rangle$ for an electron in graphene is given by Eq. B.22 (see Appendix B) as

$$\left|\boldsymbol{K}_\ell\right\rangle = \frac{1}{\sqrt{A_{\text{gr}}}} \left|\chi_{\boldsymbol{k}_\ell}\right\rangle e^{i\boldsymbol{k}_\ell \cdot \boldsymbol{r}} \left|\phi_\ell\left(z\right)\right\rangle \tag{4.29}$$

with the in-plane component being

$$\left|\chi_{\boldsymbol{k}_\ell}\right\rangle = \frac{1}{\sqrt{2}} \begin{bmatrix} 1 \\ e^{i\theta(\boldsymbol{k}_\ell)} \end{bmatrix} \tag{4.30}$$

so that

$$\left\langle I_1\right| H_{\text{e-ph}} \otimes \mathbb{I}_{\text{ex}} \left|i\right\rangle = \frac{ev_F}{c} \left(\frac{2\pi\hbar c^2}{V\omega_q\eta^2}\right)^{1/2} \frac{1}{A_{\text{gr}}} \left\langle \phi_R\right| e^{-iq_z z} \left|\phi_L\right\rangle \left\langle \chi_{\boldsymbol{k}_R}\right| e^{i\left(\boldsymbol{k}_L - \boldsymbol{k}_R - \boldsymbol{q}_\parallel\right)\cdot \boldsymbol{r}} \boldsymbol{e}_{\boldsymbol{q}}^\lambda \cdot \boldsymbol{\sigma} \left|\chi_{\boldsymbol{k}_L}\right\rangle \tag{4.31}$$

Focusing on the factor $\left\langle \phi_R\right| e^{-iq_z z} \left|\phi_L\right\rangle$, we treat the electric field in between the graphene sheets as a perturbation (only shifting the energies) so that, in a good approximation, we can consider the electron confining wave-function $\left|\phi_\ell\right\rangle$ in the z direction to be the wave-function of particle in a Dirac delta potential, which is given by

$$\phi\left(z\right) = \sqrt{\kappa} e^{-\kappa|z|} \tag{4.32}$$

where we account for the environment difference (on one side of graphene is vacuum and on the other side is a dielectric) in the wave-vector κ such that

$$\phi\left(z\right) = \begin{cases} \sqrt{\kappa_1} e^{-\kappa_1|z \pm a|} & |z| > a \\ \sqrt{\kappa_2} e^{-\kappa_2|z|} & |z| < a \end{cases} \tag{4.33}$$

with

$$\kappa_1 = \sqrt{\frac{2mE_{\text{w}}}{\hbar^2}},\ \kappa_2 = \sqrt{\frac{2m\left(E_{\text{w}} - V_0\right)}{\hbar^2}} \tag{4.34}$$

where E_{w} is the energy required to extract an electron from graphene (typically 4.3 eV [174]) and $V_0 \approx -0.5$ eV is the bottom of the conduction band of hBN (see Appendix B.2).

Therefore, we have

$$\begin{aligned}
&\langle \phi_R | \, e^{-iq_z z} \, | \phi_L \rangle = \\
&= \kappa_1 \int_{-\infty}^{-a} e^{-\kappa_1|z+a|} e^{-\kappa_1|z-a|} e^{-iq_z z} dz + \kappa_2 \int_{-a}^{a} e^{-\kappa_2|z+a|} e^{-\kappa_2|z-a|} e^{-iq_z z} dz \\
&+ \kappa_1 \int_{a}^{\infty} e^{-\kappa_1|z+a|} e^{-\kappa_1|z-a|} e^{-iq_z z} dz \\
&= \kappa_1 \frac{e^{-(2\kappa_1 - iq_z)a}}{2\kappa_1 - iq_z} + \kappa_2 e^{-2\kappa_2 a} \frac{2\sin\left(q_z a\right)}{q_z} + \kappa_1 \frac{e^{-(2\kappa_1 + iq_z)a}}{2\kappa_1 + iq_z}
\end{aligned} \tag{4.35}$$

Since $\kappa_1 \approx 10^{10}\text{m}^{-1}$ and $q = 2\pi/\lambda \approx 10^7\text{m}^{-1}$ ($\lambda = 600$nm is the typical wavelength of excitonic emission in TMDs), we have $\kappa \gg q$ so that the dominant contribution comes from the second term and thus we can discard the other terms, so that we end up with

$$\langle \phi_R | \, e^{-iq_z z} \, | \phi_L \rangle = \kappa_2 e^{-2\kappa_2 a} \frac{2\sin\left(q_z a\right)}{q_z} \tag{4.36}$$

Moreover, since $a \approx 10$nm we can approximate $\sin\left(q_z a\right) \approx q_z a$ so that

$$\langle \phi_R | \, e^{-iq_z z} \, | \phi_L \rangle \simeq 2\kappa a e^{-2\kappa a} \tag{4.37}$$

where we have redefined $\kappa_2 \to \kappa$. Therefore, we have that

$$\langle I_1 | \, H_{\text{e-ph}} \otimes \mathbb{I}_{\text{ex}} \, | i \rangle = 2\frac{ev_F}{c} \kappa a e^{-2\kappa a} B_{\boldsymbol{q}} \frac{1}{A_{\text{gr}}} \langle \chi_{\boldsymbol{k}_R} | \, e^{i\left(\boldsymbol{k}_L - \boldsymbol{k}_R - \boldsymbol{q}_\parallel\right)\cdot \boldsymbol{r}} \boldsymbol{e}_{\boldsymbol{q}}^{\lambda} \cdot \boldsymbol{\sigma} \, | \chi_{\boldsymbol{k}_L} \rangle \tag{4.38}$$

Proceeding to the matrix element for the exciton-photon interaction, $\langle f | \, \mathbb{I}_{\text{e}} \otimes H_{\text{ph-ex}} \, | I_1 \rangle$, it reads

$$\begin{aligned}
\langle f | \, \mathbb{I}_{\text{e}} \otimes H_{\text{ph-ex}} \, | I_1 \rangle &= \langle n_{\text{ex}}, \boldsymbol{k}_{\text{ex}} | \, \langle 0_{\boldsymbol{q}} | \, \langle \boldsymbol{K}_R | \, \mathbb{I}_{\text{e}} \otimes H_{\text{ph-ex}} \, | \boldsymbol{K}_R \rangle \, \left| 1_{\boldsymbol{q}_2} \right\rangle | 0_{\text{ex}} \rangle \\
&= \langle n_{\text{ex}}, \boldsymbol{k}_{\text{ex}} | \, \langle 0_{\boldsymbol{q}} | \, H_{\text{ph-ex}} \left| 1_{\boldsymbol{q}_2} \right\rangle | 0_{\text{ex}} \rangle
\end{aligned} \tag{4.39}$$

and from Eq. 4.16 we obtain

$$\begin{aligned}
\langle f | \, \mathbb{I}_{\text{e}} \otimes H_{\text{ph-ex}} \, | I_1 \rangle &= \frac{i}{c} \sum_{\boldsymbol{q}\lambda} \omega_{\boldsymbol{q}} \left(\boldsymbol{d}_{\text{cv}} \cdot \boldsymbol{e}_{\boldsymbol{q}}^{\lambda} \right) B_{\boldsymbol{q}} \langle n_{\text{ex}}, \boldsymbol{k}_{\text{ex}} | \, \langle 0_{\boldsymbol{q}\lambda} | \left[a_{\boldsymbol{q}\lambda} e^{i\boldsymbol{q}\cdot\boldsymbol{R}} - a_{\boldsymbol{q}\lambda}^{\dagger} e^{-i\boldsymbol{q}\cdot\boldsymbol{R}} \right] \left| 1_{\boldsymbol{q}_2\lambda_2} \right\rangle | 0_{\text{ex}} \rangle \\
&= \frac{i}{c} \omega_{\boldsymbol{q}} \left(\boldsymbol{d}_{\text{cv}} \cdot \boldsymbol{e}_{\boldsymbol{q}}^{\lambda} \right) B_{\boldsymbol{q}} \langle n_{\text{ex}}, \boldsymbol{k}_{\text{ex}} | \, e^{i\boldsymbol{q}\cdot\boldsymbol{R}} | 0_{\text{ex}} \rangle
\end{aligned} \tag{4.40}$$

The matrix element $\langle n_{\text{ex}}, \boldsymbol{k}_{\text{ex}}| \, e^{i\boldsymbol{q}\cdot\boldsymbol{R}} \, |0_{\text{ex}}\rangle$ is a well-known quantity from the theory of excitons in semiconductors [169, 175] in the hydrogenoic approximation, and is given by

$$\langle n_{\text{ex}}, \boldsymbol{k}_{\text{ex}}| \, e^{i\boldsymbol{q}\cdot\boldsymbol{R}} \, |0_{\text{ex}}\rangle = F_n\left(0\right) \frac{e^{iq_z d}}{\sqrt{S}} \delta\left(\boldsymbol{k} - \boldsymbol{q}_{\parallel}\right) \tag{4.41}$$

where S is the area of the TMD, $F_n\left(r_{\text{ex}}\right)$ is the two-dimensional hydrogenoic wave-function of an exciton in the n-th state with its argument r_{ex} being the relative position vector for the electron-hole pair and the factor $e^{iq_z d}$ comes from the fact that the excitons are confined in the TMD's plane at $z = d$ (with $d = a + b$). Thus, we have

$$\langle f| \, \mathbb{I}_{\text{e}} \otimes H_{\text{ph-ex}} \, |I_1\rangle = \frac{i}{c} \left(\boldsymbol{d}_{\text{cv}} \cdot \boldsymbol{e}_{\boldsymbol{q}}^{\lambda}\right) \omega_{\boldsymbol{q}} B_{\boldsymbol{q}} F_n\left(0\right) e^{iq_z d} \delta\left(\boldsymbol{k} - \boldsymbol{q}_{\parallel}\right) \tag{4.42}$$

so that, by plugging Eqs. 4.27, 4.38 and 4.42 into Eq. 4.24, we obtain

$$\begin{aligned} M_1 = & \frac{iev_F \kappa a e^{-2\kappa a}}{\hbar v_F \left(k_L - k_R\right) + eV_b - \hbar\omega_q} \frac{4\pi\hbar}{V\sqrt{S}\eta^2} F_n\left(0\right) e^{iq_z d} \delta\left(\boldsymbol{k} - \boldsymbol{q}_{\parallel}\right) \\ & \left(\boldsymbol{d}_{\text{cv}} \cdot \boldsymbol{e}_{\boldsymbol{q}}^{\lambda}\right) \frac{1}{A_{\text{gr}}} \langle \chi_{\boldsymbol{k}_R}| \, e^{i\left(\boldsymbol{k}_L - \boldsymbol{k}_R - \boldsymbol{q}_{\parallel}\right)\cdot\boldsymbol{r}} \boldsymbol{e}_{\boldsymbol{q}}^{\lambda} \cdot \boldsymbol{\sigma} \, |\chi_{\boldsymbol{k}_L}\rangle \end{aligned} \tag{4.43}$$

In order to further simplify this expression, we need to consider the two possible polarizations, s and p. From Fig. 28, we can infer that for the p-polarization, the vector $\boldsymbol{e}_{\boldsymbol{q}}^{\lambda}$ is given by $\boldsymbol{e}_{\boldsymbol{q}}^{\lambda} = \left(\cos\left(\theta\right), 0, \sin\left(\theta\right)\right)$, so that

$$\begin{aligned} & \left(\boldsymbol{d}_{\text{cv}} \cdot \boldsymbol{e}_{\boldsymbol{q}}^{\lambda}\right) \langle \chi_{\boldsymbol{k}_R}| \, e^{i\left(\boldsymbol{k}_L - \boldsymbol{k}_R - \boldsymbol{q}_{\parallel}\right)\cdot\boldsymbol{r}} \boldsymbol{e}_{\boldsymbol{q}}^{\lambda} \cdot \boldsymbol{\sigma} \, |\chi_{\boldsymbol{k}_L}\rangle = \\ & = d_{\text{cv}} \frac{\cos^2\left(\theta\right)}{2\sqrt{2}} \frac{1}{A_{\text{gr}}} \langle \chi_{\boldsymbol{k}_R}| \, e^{i\left(\boldsymbol{k}_L - \boldsymbol{k}_R - \boldsymbol{q}_{\parallel}\right)\cdot\boldsymbol{r}} \sigma_x \, |\chi_{\boldsymbol{k}_L}\rangle \\ & = d_{\text{cv}} \frac{\cos^2\left(\theta\right)}{2\sqrt{2}} \begin{bmatrix} 1 \\ e^{i\theta(\boldsymbol{k}_R)} \end{bmatrix}^{\dagger} \begin{pmatrix} 0 & 1 \\ 1 & 0 \end{pmatrix} \begin{bmatrix} 1 \\ e^{i\theta(\boldsymbol{k}_L)} \end{bmatrix} \frac{1}{A_{\text{gr}}} \int d\boldsymbol{r} e^{i\left(\boldsymbol{k}_L - \boldsymbol{k}_R - \boldsymbol{q}_{\parallel}\right)\cdot\boldsymbol{r}} \\ & = d_{\text{cv}} \frac{\cos^2\left(\theta\right)}{2\sqrt{2}} \left(e^{i\theta_{\boldsymbol{k}_L}} + e^{-i\theta_{\boldsymbol{k}_R}}\right) \delta_{\boldsymbol{k}_L - \boldsymbol{k}_R - \boldsymbol{q}_{\parallel}} \end{aligned} \tag{4.44}$$

For the case of s-polarization, $\boldsymbol{e}_{\boldsymbol{q}}^{\lambda} = (0, 1, 0)$, so that

$$\begin{aligned} & \langle \chi_{\boldsymbol{k}_R}| \, e^{i\left(\boldsymbol{k}_L - \boldsymbol{k}_R - \boldsymbol{q}_{\parallel}\right)\cdot\boldsymbol{r}} \boldsymbol{e}_{\boldsymbol{q}}^{\lambda} \cdot \boldsymbol{\sigma} \, |\chi_{\boldsymbol{k}_L}\rangle \\ & = \frac{id_{\text{cv}}}{2\sqrt{2}} \frac{1}{A_{\text{gr}}} \langle \chi_{\boldsymbol{k}_R}| \, e^{i\left(\boldsymbol{k}_L - \boldsymbol{k}_R - \boldsymbol{q}_{\parallel}\right)\cdot\boldsymbol{r}} \sigma_y \, |\chi_{\boldsymbol{k}_L}\rangle \\ & = \frac{id_{\text{cv}}}{2\sqrt{2}} \begin{bmatrix} 1 \\ e^{i\theta(\boldsymbol{k}_R)} \end{bmatrix}^{\dagger} \begin{pmatrix} 0 & -i \\ i & 0 \end{pmatrix} \begin{bmatrix} 1 \\ e^{i\theta(\boldsymbol{k}_L)} \end{bmatrix} \frac{1}{A_{\text{gr}}} \int d\boldsymbol{r} e^{i\left(\boldsymbol{k}_L - \boldsymbol{k}_R - \boldsymbol{q}_{\parallel}\right)\cdot\boldsymbol{r}} \\ & = \frac{d_{\text{cv}}}{2\sqrt{2}} \left(e^{i\theta_{\boldsymbol{k}_L}} - e^{-i\theta_{\boldsymbol{k}_R}}\right) \delta_{\boldsymbol{k}_L - \boldsymbol{k}_R - \boldsymbol{q}_{\parallel}} \end{aligned} \tag{4.45}$$

Therefore, the total matrix element for this process is

$$M_1 = iev_F\kappa a\sqrt{2}\frac{\pi\hbar}{\sqrt{S}V\eta^2}F_n\left(0\right)d_{\text{cv}}e^{-2\kappa a}\frac{e^{iq_z d}\delta\left(\boldsymbol{k}-\boldsymbol{q}_{\parallel}\right)\delta_{\boldsymbol{k}_L-\boldsymbol{k}_R-\boldsymbol{q}_{\parallel}}}{\hbar v_F\left(k_L-k_R\right)+eV_b-\hbar\omega_q}A^{(\lambda)}\left(\boldsymbol{k}_L,\boldsymbol{k}_R\right) \tag{4.46}$$

where we have introduced $A^{(\lambda)}\left(\boldsymbol{k}_L,\boldsymbol{k}_R\right)$ to account for the different factors that arise from each polarization, which reads

$$A^{(\lambda)}\left(\boldsymbol{k}_L,\boldsymbol{k}_R\right)=\begin{cases}\cos^2\left(\theta\right)\left(e^{i\theta_{\boldsymbol{k}_L}}+e^{-i\theta_{\boldsymbol{k}_R}}\right) & ,\lambda=p\\ \left(e^{i\theta_{\boldsymbol{k}_L}}-e^{-i\theta_{\boldsymbol{k}_R}}\right) & ,\lambda=s\end{cases} \tag{4.47}$$

4.2.2 Inverse process, M_2

The calculation of M_2 is made in the same fashion as it was done for M_1, so we do not go into the details. Starting with the denominator, it reads

$$E_i-E_2=-\hbar\omega_{\boldsymbol{q}}-E_{\text{ex}}\left(n,\boldsymbol{k}\right) \tag{4.48}$$

and for the numerator, we can follow a shortcut and reuse the one obtained for M_1 by replacing $\boldsymbol{q}\rightarrow-\boldsymbol{q}$, which leads to

$$M_2 = iev_F\kappa a\sqrt{2}\frac{\pi\hbar}{\sqrt{S}V\eta^2}F_n\left(0\right)d_{\text{cv}}e^{-2\kappa a}\frac{e^{-iq_z d}\delta\left(\boldsymbol{k}+\boldsymbol{q}_{\parallel}\right)\delta_{\boldsymbol{k}_L-\boldsymbol{k}_R+\boldsymbol{q}_{\parallel}}}{-\hbar\omega_{\boldsymbol{q}}-E_{\text{ex}}\left(n,\boldsymbol{k}\right)}A^{(\lambda)}\left(\boldsymbol{k}_L,\boldsymbol{k}_R\right) \tag{4.49}$$

4.2.3 Total matrix element M_{if}

Now that we have found the explicit expression for both M_1 and M_2, we plug the two together in order to obtain $M_{i\rightarrow f}$. Therefore, we have

$$\begin{aligned}M_{if}&=\sum_{\boldsymbol{q}\lambda}\left[M_1+M_2\right]\\&=iev_F\kappa a\sqrt{2}\frac{\pi\hbar}{\sqrt{S}V\eta^2}F_n\left(0\right)d_{\text{cv}}e^{-2\kappa a}\sum_{\boldsymbol{q}\lambda}A^{(\lambda)}\left(\boldsymbol{k}_L,\boldsymbol{k}_R\right)\cdot\\&\cdot\left[\frac{e^{iq_z d}\delta\left(\boldsymbol{k}-\boldsymbol{q}_{\parallel}\right)\delta_{\boldsymbol{k}_L-\boldsymbol{k}_R-\boldsymbol{q}_{\parallel}}}{\hbar v_F\left(k_L-k_R\right)+eV_b-\hbar\omega_q}+\frac{e^{-iq_z d}\delta\left(\boldsymbol{k}+\boldsymbol{q}_{\parallel}\right)\delta_{\boldsymbol{k}_L-\boldsymbol{k}_R+\boldsymbol{q}_{\parallel}}}{-\hbar\omega_{\boldsymbol{q}}-E_{\text{ex}}\left(n,\boldsymbol{k}\right)}\right]\end{aligned} \tag{4.50}$$

We can promote the sum over $\boldsymbol{q}$ into a integral such that

$$M_{if} = \frac{V}{(2\pi)^3} iev_F\kappa a\sqrt{2}\frac{\pi\hbar}{\sqrt{S}V\eta^2} F_n(0)\, d_{\text{cv}} e^{-2\kappa a}\cdot$$
$$\cdot \sum_\lambda \int d\boldsymbol{q} A^{(\lambda)}(\boldsymbol{k}_L, \boldsymbol{k}_R) \left[\frac{e^{iq_z d}\delta\left(\boldsymbol{k} - \boldsymbol{q}_\parallel\right)\delta_{\boldsymbol{k}_L - \boldsymbol{k}_R - \boldsymbol{q}_\parallel}}{\hbar v_F(k_L - k_R) + eV_b - \hbar\omega_q} + \frac{e^{-iq_z d}\delta\left(\boldsymbol{k} + \boldsymbol{q}_\parallel\right)\delta_{\boldsymbol{k}_L - \boldsymbol{k}_R + \boldsymbol{q}_\parallel}}{-\hbar\omega_{\boldsymbol{q}} - E_{\text{ex}}(n, \boldsymbol{k})}\right] \tag{4.51}$$

where the integration over $\boldsymbol{q}_\parallel$ of $\delta\left(\boldsymbol{k} \pm \boldsymbol{q}_\parallel\right)$ yields $\boldsymbol{q}_\parallel = \pm\boldsymbol{k}$, leading to

$$M_{if} = i\sqrt{2}\frac{ev_F\kappa a}{(2\pi)^3}\frac{\pi\hbar}{\sqrt{S}\eta^2} F_n(0)\, d_{\text{cv}} e^{-2\kappa a}\delta_{\boldsymbol{k}_L - \boldsymbol{k}_R - \boldsymbol{k}}\cdot$$
$$\cdot \sum_\lambda \int dq_z A^{(\lambda)}(\boldsymbol{k}_L, \boldsymbol{k}_R) \left[\frac{e^{iq_z d}}{\hbar v_F k + eV_b - \hbar\omega_q} + \frac{e^{-iq_z d}}{-\hbar\omega_{\boldsymbol{q}} - E_{\text{ex}}(n, \boldsymbol{k})}\right] \tag{4.52}$$

where we have set $k_L - k_R \to k$ due to the presence of $\delta_{\boldsymbol{k}_L - \boldsymbol{k}_R - \boldsymbol{k}}$.

We anticipate the conservation of global energy by setting

$$E_{\text{ex}}(n, \boldsymbol{k}) = \hbar v_F k + eV_b \tag{4.53}$$

so that

$$M_{if} = i\sqrt{2}\frac{ev_F\kappa a}{(2\pi)^3}\frac{\pi\hbar}{\sqrt{S}\eta^2} F_n(0)\, d_{\text{cv}} e^{-2\kappa a}\delta_{\boldsymbol{k}_L - \boldsymbol{k}_R - \boldsymbol{k}}\cdot$$
$$\cdot \sum_\lambda \int dq_z A^{(\lambda)}(\boldsymbol{k}_L, \boldsymbol{k}_R) \left[\frac{e^{iq_z d}}{E_{\text{ex}}(n, \boldsymbol{k}) - \hbar\omega_q} - \frac{e^{-iq_z d}}{E_{\text{ex}}(n, \boldsymbol{k}) + \hbar\omega_{\boldsymbol{q}}}\right] \tag{4.54}$$

and by changing $q_z \to -q_z$ in the second term, we can write M_{if} as

$$M_{if} = i\sqrt{2}\frac{ev_F\kappa a}{(2\pi)^3}\frac{\pi\hbar}{\sqrt{S}\eta^2} F_n(0)\, d_{\text{cv}} e^{-2\kappa a}\delta_{\boldsymbol{k}_L - \boldsymbol{k}_R - \boldsymbol{k}}\cdot$$
$$\cdot \frac{2\eta}{\hbar c}\sum_\lambda \int dq_z A^{(\lambda)}(\boldsymbol{k}_L, \boldsymbol{k}_R)\frac{qe^{iq_z d}}{Q^2 - q^2} \tag{4.55}$$

with $Q = E_{\text{ex}}(n, \boldsymbol{k})\,\eta/\hbar c$. Since the excitons in the TMD have a finite lifetime, we introduce a small imaginary part to their energy as $E_{\text{ex}} \to E_{\text{ex}} - i\Delta$, so that $Q \simeq Q_0 - i\Gamma$, with $\Gamma = \Delta\eta/\hbar c$, where we have neglected the kinetic energy $\hbar^2 k^2/2m_{\text{ex}}$ of the exciton due to its effective mass m_{ex} being relatively large. Therefore, we have

$$M_{if} = \sqrt{2}\frac{iev_F\kappa a}{4\pi^2\eta c\sqrt{S}} F_n(0)\, d_{\text{cv}} e^{-2\kappa a}\delta_{\boldsymbol{k}_L - \boldsymbol{k}_R - \boldsymbol{k}}\sum_\lambda J^{(\lambda)}(\boldsymbol{k}_L, \boldsymbol{k}_R) \tag{4.56}$$

with

$$J^{(\lambda)}(\boldsymbol{k}_L, \boldsymbol{k}_R) = \int dq_z A^{(\lambda)}(\boldsymbol{k}_L, \boldsymbol{k}_R)\frac{e^{iq_z d}\sqrt{k^2 + q_z^2}}{Q_0^2 - 2iQ_0\Gamma - k^2 - q_z^2} \tag{4.57}$$

where we are left with the integration in q_z.

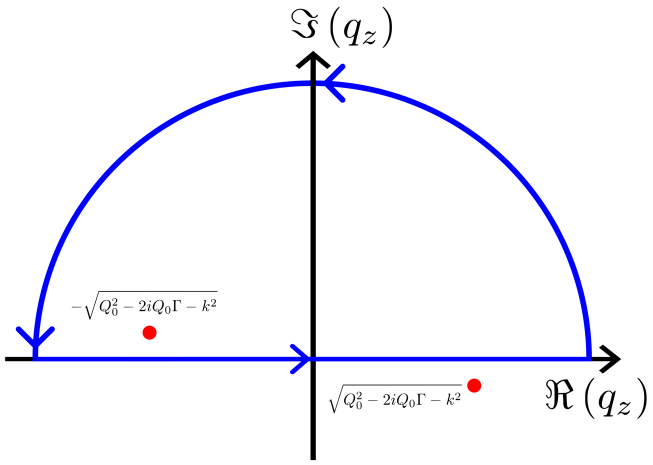


Figure 30: Complex contour (half-circumference in blue) with infinite radius used for the evaluation of $J^{(\lambda)}$ for the case when $k < Q_0$. The red dots are the poles at $q_z = \pm\sqrt{Q_0^2 - 2iQ_0\Gamma - k^2}$. The choosing of our contour leads to only the pole $q_z^- = -\sqrt{Q_0^2 - 2iQ_0\Gamma - k^2}$ being accounted.

4.2.4 Integration in q_z

We now focus on solving the integral

$$J^{(\lambda)}(\boldsymbol{k}_L, \boldsymbol{k}_R) = \int dq_z A^{(\lambda)}(\boldsymbol{k}_L, \boldsymbol{k}_R) \frac{e^{iq_z d}\sqrt{k^2+q_z^2}}{Q_0^2 - 2iQ_0\Gamma - k^2 - q_z^2} \tag{4.58}$$

where we need to be careful when dealing with the different polarizations.

Starting with the s-polarization, in this case we have

$$J^{(s)}(\boldsymbol{k}_L, \boldsymbol{k}_R) = A^{(s)}(\boldsymbol{k}_L, \boldsymbol{k}_R) \int dq_z \frac{e^{iq_z d}\sqrt{k^2+q_z^2}}{Q_0^2 - 2iQ_0\Gamma - k^2 - q_z^2} \tag{4.59}$$

where we have removed $A^{(s)}$ out of the integral since it does not depend on q_z. We remark that this integral has poles at $q_z^{\pm} = \pm\sqrt{Q_0^2 - 2iQ_0\Gamma - k^2}$, where we need to separate the cases when $k \lessgtr Q_0$.

For $k < Q_0$, the poles lie close to the real axis with a small imaginary shift due to Γ, as shown in Fig. 30, but only the pole q_z^- lies inside the complex contour.

Therefore, resorting to the residue theorem we have that

$$J^{(s)}(\boldsymbol{k}_L, \boldsymbol{k}_R) = \pi i A^{(s)}(\boldsymbol{k}_L, \boldsymbol{k}_R) \sqrt{\frac{Q_0^2 - 2iQ_0\Gamma}{Q_0^2 - 2iQ_0\Gamma - k^2}} e^{-i\sqrt{Q_0^2 - 2iQ_0\Gamma - k^2}d}, \text{ for } k < Q_0 \tag{4.60}$$

For $k > Q_0$, the poles lie close to the imaginary axis with a small real shift due to Γ, as shown in Fig. 31, but only the pole q_z^+ lies inside the complex contour. Once again, the residue theorem yields

$$J^{(s)}(\boldsymbol{k}_L, \boldsymbol{k}_R) = \pi A^{(s)}(\boldsymbol{k}_L, \boldsymbol{k}_R) \sqrt{\frac{Q_0^2 - 2iQ_0\Gamma}{k^2 - Q_0^2 + 2iQ_0\Gamma}} e^{-\sqrt{k^2 - Q^2 + 2iQ_0\Gamma}d}, \text{ for } k > Q_0 \tag{4.61}$$

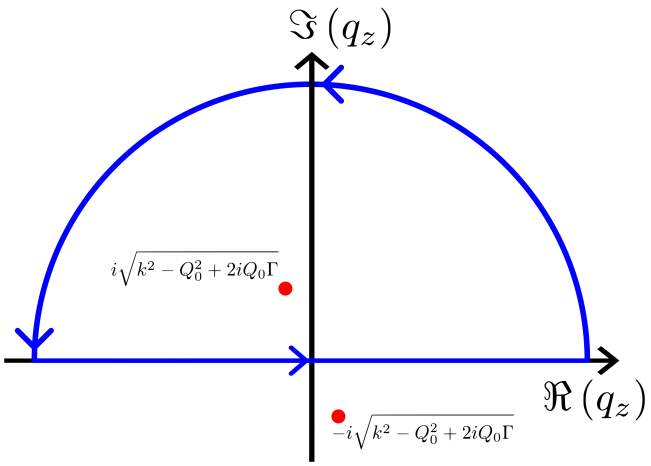


Figure 31: Complex contour (half-circumference in blue) with infinite radius used for the evaluation of $J^{(\lambda)}$ for the case when $k > Q_0$. The red dots are the poles at $q_z = \pm i\sqrt{k^2 - Q^2 + 2iQ_0\Gamma}$. The choosing of our contour leads to only the pole $q_z^+ = +i\sqrt{k^2 - Q_0^2 + 2iQ_0\Gamma}$ being accounted.

Therefore, for the s-polarization we have

$$J^{(s)}\left(\boldsymbol{k}_L, \boldsymbol{k}_R\right) = \pi A^{(s)}\left(\boldsymbol{k}_L, \boldsymbol{k}_R\right)\sqrt{Q_0^2 - 2iQ_0\Gamma}\begin{cases} i\frac{e^{-\sqrt{k^2-Q^2+2iQ_0\Gamma}d}}{\sqrt{k^2-Q_0^2+2iQ_0\Gamma}}, & \text{for } k > Q_0 \\ \frac{e^{-i\sqrt{Q_0^2-2iQ_0\Gamma-k^2}d}}{\sqrt{Q_0^2-2iQ_0\Gamma-k^2}}, & \text{for } k < Q_0 \end{cases} \tag{4.62}$$

Proceeding to the case of p-polarization, we have

$$J^{(p)}\left(\boldsymbol{k}_L, \boldsymbol{k}_R\right) = C^p\left(\boldsymbol{k}_L, \boldsymbol{k}_R\right)\int dq_z \frac{q_z^2}{q_z^2 + k^2}\frac{e^{iq_z d}\sqrt{k^2 + q_z^2}}{Q_0^2 - 2iQ_0\Gamma - k^2 - q_z^2} \tag{4.63}$$

with $C^p\left(\boldsymbol{k}_L, \boldsymbol{k}_R\right) = \left(e^{i\theta_{\boldsymbol{k}_L}} + e^{-i\theta_{\boldsymbol{k}_R}}\right)$. In this case, we have the same poles as $J^{(s)}$, with the addition of the poles at $q_z = \pm ik$. However, we remark that when calculating the residue corresponding to this pole it yields 0 due to the factor $\sqrt{k^2 + q_z^2}$. Therefore, we shall only be concerned with the poles $q_z^{\pm} = \pm\sqrt{Q_0^2 - 2iQ_0\Gamma - k^2}$ where, as before, we separate the cases when $k \lessgtr Q_0$. For the case of $k < Q_0$, by using the contour depicted in Fig. 30 and using the residue theorem we obtain

$$\begin{aligned} J^{(p)}\left(\boldsymbol{k}_L, \boldsymbol{k}_R\right) &= \pi i C^p\left(\boldsymbol{k}_L, \boldsymbol{k}_R\right)\frac{Q_0^2 - 2iQ_0\Gamma - k^2}{Q_0^2 - 2iQ_0\Gamma}\frac{e^{-i\sqrt{Q_0^2-2iQ_0\Gamma-k^2}d}\sqrt{Q_0^2 - 2iQ_0\Gamma}}{\sqrt{Q_0^2 - 2iQ_0\Gamma - k^2}} \\ &= \pi i C^p\left(\boldsymbol{k}_L, \boldsymbol{k}_R\right)\sqrt{\frac{Q_0^2 - 2iQ_0\Gamma - k^2}{Q_0^2 - 2iQ_0\Gamma}}e^{-i\sqrt{Q_0^2-2iQ_0\Gamma-k^2}d}, \text{ for } k < Q_0 \end{aligned} \tag{4.64}$$

The case of $k > Q_0$ yields

$$J^{(p)}\left(\boldsymbol{k}_L, \boldsymbol{k}_R\right) = -\pi i C^p\left(\boldsymbol{k}_L, \boldsymbol{k}_R\right) \frac{Q_0^2 - 2iQ_0\Gamma - k^2}{Q_0^2 - 2iQ_0\Gamma} \frac{e^{-\sqrt{k^2 - Q_0^2 + 2iQ_0\Gamma}d}\sqrt{Q_0^2 - 2iQ_0\Gamma}}{i\sqrt{k^2 - Q_0^2 + 2iQ_0\Gamma}}$$
$$= \pi C^p\left(\boldsymbol{k}_L, \boldsymbol{k}_R\right) \sqrt{\frac{k^2 - Q_0^2 + 2iQ_0\Gamma}{Q_0^2 - 2iQ_0\Gamma}} e^{-\sqrt{k^2 - Q_0^2 + 2iQ_0\Gamma}d}, \text{ for } k > Q_0 \tag{4.65}$$

Therefore, for the s-polarization we have

$$J^{(p)}\left(\boldsymbol{k}_L, \boldsymbol{k}_R\right) = \pi C^{(p)}\left(\boldsymbol{k}_L, \boldsymbol{k}_R\right) \begin{cases} \sqrt{\frac{k^2 - Q_0^2 + 2iQ_0\Gamma}{Q_0^2 - 2iQ_0\Gamma}} e^{-\sqrt{k^2 - Q_0^2 + 2iQ_0\Gamma}d}, & \text{for } k > Q_0 \\ i\sqrt{\frac{Q_0^2 - 2iQ_0\Gamma - k^2}{Q_0^2 - 2iQ_0\Gamma}} e^{-i\sqrt{Q_0^2 - 2iQ_0\Gamma - k^2}d}, & \text{for } k < Q_0 \end{cases} \tag{4.66}$$

4.3 Fermi's Golden Rule and inelastic current

Now that we have obtained an expression for $M_{i\to f}$, we are able to obtain the probability for this transition to occur (which is related to the rate of generation of excitons) via Fermi's Golden Rule, which states that

$$W_{i\to f}\left(\boldsymbol{k}_L\right) =$$
$$= \frac{2\pi}{\hbar} g_s g_\nu \sum_{\boldsymbol{k}, \boldsymbol{k}_R, n} \left|M_{i\to f}\left(\boldsymbol{k}_L, \boldsymbol{k}_R, \boldsymbol{k}\right)\right|^2 f\left(k_L, \mu_L\right)\left[1 - f\left(k_R, \mu_R\right)\right] \delta\left\{eV_\text{b} + \hbar v_F\left(k_L - k_R\right) - E_\text{ex}\left(n\right)\right\} \tag{4.67}$$

where $g_{s/\nu}$ are the spin and valley degeneracies, respectively (both equal to 2 in graphene), $\mu_{L/R}$ is the Fermi level for the electrons in the left/right graphene relative to its Dirac point with $\mu_L = \mu_R + eV_\text{b}$, f is the Fermi-Dirac distribution for the occupation of electrons in graphene. To simplify this analysis, we assume that $\mu_R = 0$, we set the temperature $T = 0$K and we take $n = 0$, that being, we consider only the exciton's ground state. We point out that the expression for $M_{i\to f}$ in Eq. 4.56 has a factor $\delta_{\boldsymbol{k}_L - \boldsymbol{k}_R - \boldsymbol{k}}$ that is responsible for removing the sum over $\boldsymbol{k}_R$ in the last equation, so that we are left with only the sum over $\boldsymbol{k}$. This integration in $\boldsymbol{k}$ can be rather cumbersome do, with one of the main source of complexity being the divergence that occurs in $M_{i\to f}$ when $\boldsymbol{k} = Q_0$. Therefore, we leave it to be numerically calculated in future works.

Instead, we devote the rest of this chapter to showing the link between this model and the one studied in Chapter 2. For that, we starting by remarking that this probability (per unit of time) $W_{i\to f}$ is related

with the current density as

$$J = \frac{e}{S}\sum_{\boldsymbol{k}_L} W_{i\to f}\left(\boldsymbol{k}_L\right)$$
$$= \frac{e}{S}\frac{8\pi}{\hbar}\sum_{\boldsymbol{k}_L\boldsymbol{k}_R}\sum_{\boldsymbol{k}} \left|M_{i\to f}\left(\boldsymbol{k}_L,\boldsymbol{k}_R,\boldsymbol{k}\right)\right|^2 f\left(k_L,\mu_L\right)\left[1-f\left(k_R,\mu_R\right)\right]\delta\left\{eV_{\text{b}}+\hbar v_F\left(k_L-k_R\right)-E_{\text{ex}}\left(0\right)\right\} \tag{4.68}$$

Promoting the sum over the momenta of the electrons in the two graphene sheets as a energy integral (where we need to account with their respective density of states), we can rewrite this expression as

$$J \propto \int d\varepsilon_L \int d\varepsilon_R \left[\sum_{\boldsymbol{k}_L\boldsymbol{k}_R} \delta\left(\varepsilon_R-\varepsilon_{\boldsymbol{k}_R}\right)\delta\left(\varepsilon_L-\varepsilon_{\boldsymbol{k}_L}\right) f\left(\varepsilon_L,\mu_L\right)\left[1-f\left(\varepsilon_R,\mu_R\right)\right]\cdot\right.$$
$$\left.\cdot\sum_{\boldsymbol{k}}\left|M_{i\to f}\left(\boldsymbol{k}_L,\boldsymbol{k}_R,\boldsymbol{k}\right)\right|^2\delta\left\{\varepsilon_L-\varepsilon_R-E_{\text{ex}}\left(0\right)\right\}\right] \tag{4.69}$$

where we have set $\varepsilon_L = \hbar v_F k_L + eV_{\text{b}}$, $\varepsilon_R = \hbar v_F k_R$ and $\varepsilon_{\boldsymbol{k}_L/\boldsymbol{k}_R}$ is the dispersion relation of the left/right graphene sheets. The delta factor that comes from the Fermi Golden Rule allows us to calculate one of the integrals such that

$$J \propto \int d\varepsilon_L f\left(\varepsilon_L,\mu_L\right)\left[1-f\left(\varepsilon_L-E_{\text{ex}}\left(0\right),\mu_R\right)\right]T_{\text{x}}\left(\varepsilon_L\right) \tag{4.70}$$

where we have defined $T_{\text{x}}\left(\varepsilon_L\right)$ as

$$T_{\text{x}}\left(\varepsilon_L\right) = \sum_{\boldsymbol{k}_L\boldsymbol{k}_R}\delta\left(\varepsilon_L-E_{\text{ex}}\left(0\right)-\varepsilon_{\boldsymbol{k}_R}\right)\delta\left(\varepsilon_L-\varepsilon_{\boldsymbol{k}_L}\right)\sum_{\boldsymbol{k}}\left|M_{i\to f}\left(\boldsymbol{k}_L,\boldsymbol{k}_R,\boldsymbol{k}\right)\right|^2 \tag{4.71}$$

which we relate to the formalism of the previous chapter by calling it the transmission function, in analogy with Eqs. 2.93 and 3.58.

Thus, we can see that from this conceptually simpler formalism we can still obtain results for the current that are analogous to those derived using the NEGF formalism, namely, an expression for the current that is given by the energy integral of the contact's occupation factors and a quantity that is related to the probability for the transition to occur - the transmission function.

Chapter 5

Conclusion and Outlook

As a conclusion, we summarize below the work presented in this thesis.

In Chapter 2, we have delved into the formalism of non-equilibrium Green's functions, where we have acquired the necessary expertise to be able to employ this technique in Chapter 3. In particular, we addressed a generalized transport problem for a two-contact mesoscopic system, also accounting for generic electron-boson interactions. We derived the Landauer formula for the case of non-interacting elastic current, which expresses it as the energy integral of a quantity that is often referred to as the transmission function, this being related with the probability of an electron with a given energy to cross the device. Additionally, by treating the electron-boson interactions as perturbations, we have obtained analytic expressions up to the second order for the corrections that these interactions introduce to the current, where we have considered both elastic and inelastic processes.

Moreover, in order to become acquainted with the phenomenon of tunneling currents and the effects that interactions introduce to these problems, in Chapter 3 we have applied the rather generic results of the previous chapter to a one-dimensional toy-model composed by two semi-infinite tight-binding chains of atoms coupled to a single-level central site. Thus, we have calculated the transmission function and the I-V characteristic curve at zero temperature, for both the non-interacting and interacting cases. The results show a dominant elastic feature for voltages in resonance with the single level. However, additional channels open when we account for the interactions, with their energetic position depending on the energy of the bosons. For voltages lower than the energy of the single level, these corrections contribute to an increase of the total current, although for higher voltages the opposite effect was verified. Therefore, we have concluded that, even though being intrinsically simple, this toy-model allowed us to understand some of the general features that are characteristic in electron tunneling problems arising in more complicated vdW devices.

Finally, in Chapter 4 we have addressed the problem of finding the exciton-assisted inelastic tunneling current flowing in the vdW heterostructure, electromagnetically coupled to the excitonic layer (TMD). To

do so, we resorted to second order perturbation theory to calculate the matrix element for the electron-exciton interaction, mediated by the emission and absorption of virtual photons. Then, we have plugged this result into Fermi's Golden Rule so that the inelastic current density can be expressed in the closed form of a double integral over the momenta of the graphene electron and the TMD exciton, which has to be evaluated numerically. This expression can be cast in the form of Eq. 4.70, which reveals the structural link between two models studied in this thesis, being the differences "hidden" in the matrix element and the densities of states (that depend on the dimensionality).

As for future work, two main things are planned:

- Complete the calculation of the inelastic current density, presented in this thesis, with realistic material parameters by numerical evaluation of the double integral in momenta;
- Extend the application of the NEGF technique to the 3D device, with the interaction matrix element calculated in the thesis and the necessary integration over the 2D electron momenta. Our hope is that it will enable a qualitative comparison with the existing experimental data and stimulate new experiments directed in the development of single-photon sources based on the effects considered in this thesis.

Bibliography

[1] Gordon E Moore. Cramming more components onto integrated circuits. *Proceedings of the IEEE*, 86(1):82–85, 1998.

[2] Jonathan Koomey, Stephen Berard, Marla Sanchez, and Henry Wong. Implications of historical trends in the electrical efficiency of computing. *IEEE Annals of the History of Computing*, 33(3):46–54, 2010.

[3] Max M Shulaker, Gage Hills, Rebecca S Park, Roger T Howe, Krishna Saraswat, H-S Philip Wong, and Subhasish Mitra. Three-dimensional integration of nanotechnologies for computing and data storage on a single chip. *Nature*, 547(7661):74–78, 2017.

[4] Floris A Zwanenburg, Andrew S Dzurak, Andrea Morello, Michelle Y Simmons, Lloyd CL Hollenberg, Gerhard Klimeck, Sven Rogge, Susan N Coppersmith, and Mark A Eriksson. Silicon quantum electronics. *Reviews of modern physics*, 85(3):961, 2013.

[5] Dieter Bimberg, Marius Grundmann, and Nikolai N Ledentsov. *Quantum dot heterostructures*. John Wiley & Sons, 1999.

[6] Marc A Kastner. The single-electron transistor. *Reviews of modern physics*, 64(3):849, 1992.

[7] Jerome Faist, Federico Capasso, Deborah L Sivco, Carlo Sirtori, Albert L Hutchinson, and Alfred Y Cho. Quantum cascade laser. *Science*, 264(5158):553–556, 1994.

[8] Leo P Kouwenhoven, Charles M Marcus, Paul L McEuen, Seigo Tarucha, Robert M Westervelt, and Ned S Wingreen. Electron transport in quantum dots. *Mesoscopic electron transport*, pages 105–214, 1997.

[9] John Clarke and Alex I Braginski. *The SQUID handbook: Applications of SQUIDs and SQUID systems*. John Wiley & Sons, 2006.

[10] Michael A Nielsen and Isaac L Chuang. *Quantum computation and quantum information*. Cambridge university press, 2010.

[11] Igor Žutić, Jaroslav Fabian, and S Das Sarma. Spintronics: Fundamentals and applications. *Reviews of modern physics*, 76(2):323, 2004.

[12] Yuan Liu, Nathan O Weiss, Xidong Duan, Hung-Chieh Cheng, Yu Huang, and Xiangfeng Duan. Van der waals heterostructures and devices. *Nature Reviews Materials*, 1(9):1–17, 2016.

[13] Andre K Geim and Irina V Grigorieva. Van der waals heterostructures. *Nature*, 499(7459):419–425, 2013.

[14] Sheneve Z Butler, Shawna M Hollen, Linyou Cao, Yi Cui, Jay A Gupta, Humberto R Gutiérrez, Tony F Heinz, Seung Sae Hong, Jiaxing Huang, Ariel F Ismach, et al. Progress, challenges, and opportunities in two-dimensional materials beyond graphene. *ACS nano*, 7(4):2898–2926, 2013.

[15] K S Novoselov, Artem Mishchenko, Alexandra Carvalho, and AH Castro Neto. 2d materials and van der waals heterostructures. *Science*, 353(6298):aac9439, 2016.

[16] Kostya S Novoselov, Andre K Geim, Sergei V Morozov, De-eng Jiang, Yanshui Zhang, Sergey V Dubonos, Irina V Grigorieva, and Alexandr A Firsov. Electric field effect in atomically thin carbon films. *science*, 306(5696):666–669, 2004.

[17]

[18] Santosh K Tiwari, Sumanta Sahoo, Nannan Wang, and Andrzej Huczko. Graphene research and their outputs: Status and prospect. *Journal of Science: Advanced Materials and Devices*, 5(1):10–29, 2020.

[19] Konstantin S Novoselov, Luca Colombo, PR Gellert, MG Schwab, KAJN Kim, et al. A roadmap for graphene. *nature*, 490(7419):192–200, 2012.

[20] Changgu Lee, Xiaoding Wei, Jeffrey W Kysar, and James Hone. Measurement of the elastic properties and intrinsic strength of monolayer graphene. *science*, 321(5887):385–388, 2008.

[21] J Scott Bunch, Scott S Verbridge, Jonathan S Alden, Arend M Van Der Zande, Jeevak M Parpia, Harold G Craighead, and Paul L McEuen. Impermeable atomic membranes from graphene sheets. *Nano letters*, 8(8):2458–2462, 2008.

[22] Andre K Geim and Konstantin S Novoselov. The rise of graphene. *Nature materials*, 6(3):183–191, 2007.

[23] AH Castro Neto, Francisco Guinea, Nuno MR Peres, Kostya S Novoselov, and Andre K Geim. The electronic properties of graphene. *Reviews of modern physics*, 81(1):109, 2009.

[24] Kirill I Bolotin, KJ Sikes, Zhifang Jiang, M Klima, G Fudenberg, James Hone, Phaly Kim, and Horst L Stormer. Ultrahigh electron mobility in suspended graphene. *Solid state communications*, 146(9-10):351–355, 2008.

[25] Xu Du, Ivan Skachko, Anthony Barker, and Eva Y Andrei. Approaching ballistic transport in suspended graphene. *Nature nanotechnology*, 3(8):491–495, 2008.

[26] Alexander S Mayorov, Roman V Gorbachev, Sergey V Morozov, Liam Britnell, Rashid Jalil, Leonid A Ponomarenko, Peter Blake, Kostya S Novoselov, Kenji Watanabe, Takashi Taniguchi, et al. Micrometer-scale ballistic transport in encapsulated graphene at room temperature. *Nano letters*, 11(6):2396–2399, 2011.

[27] S Das Sarma, Shaffique Adam, EH Hwang, and Enrico Rossi. Electronic transport in two-dimensional graphene. *Reviews of modern physics*, 83(2):407, 2011.

[28] Alexander A Balandin, Suchismita Ghosh, Wenzhong Bao, Irene Calizo, Desalegne Teweldebrhan, Feng Miao, and Chun Ning Lau. Superior thermal conductivity of single-layer graphene. *Nano letters*, 8(3):902–907, 2008.

[29] Suchismita Ghosh, Irene Calizo, Desalegne Teweldebrhan, Evghenii P Pokatilov, Denis L Nika, Alexander A Balandin, Wenzhong Bao, Feng Miao, and C Ning Lau. Extremely high thermal conductivity of graphene: Prospects for thermal management applications in nanoelectronic circuits. *Applied Physics Letters*, 92(15), 2008.

[30] Jae Hun Seol, Insun Jo, Arden L Moore, Lucas Lindsay, Zachary H Aitken, Michael T Pettes, Xuesong Li, Zhen Yao, Rui Huang, David Broido, et al. Two-dimensional phonon transport in supported graphene. *Science*, 328(5975):213–216, 2010.

[31] Weiwei Cai, Arden L Moore, Yanwu Zhu, Xuesong Li, Shanshan Chen, Li Shi, and Rodney S Ruoff. Thermal transport in suspended and supported monolayer graphene grown by chemical vapor deposition. *Nano letters*, 10(5):1645–1651, 2010.

[32] DL Nika, S Ghosh, EP Pokatilov, and AA Balandin. Lattice thermal conductivity of graphene flakes: Comparison with bulk graphite. *Applied Physics Letters*, 94(20), 2009.

[33] Xiangfan Xu, Luiz FC Pereira, Yu Wang, Jing Wu, Kaiwen Zhang, Xiangming Zhao, Sukang Bae, Cong Tinh Bui, Rongguo Xie, John TL Thong, et al. Length-dependent thermal conductivity in suspended single-layer graphene. *Nature communications*, 5(1):3689, 2014.

[34] Vasilios Georgakilas, Michal Otyepka, Athanasios B Bourlinos, Vimlesh Chandra, Namdong Kim, K Christian Kemp, Pavel Hobza, Radek Zboril, and Kwang S Kim. Functionalization of graphene: covalent and non-covalent approaches, derivatives and applications. *Chemical reviews*, 112(11):6156–6214, 2012.

[35] Rahul Raveendran Nair, Peter Blake, Alexander N Grigorenko, Konstantin S Novoselov, Tim J Booth, Tobias Stauber, Nuno MR Peres, and Andre K Geim. Fine structure constant defines visual transparency of graphene. *science*, 320(5881):1308–1308, 2008.

[36] Francesco Bonaccorso, Zhipei Sun, Tawfique Hasan, and Andrea C Ferrari. Graphene photonics and optoelectronics. *Nature photonics*, 4(9):611–622, 2010.

[37] Jijo Abraham, Kalangi S Vasu, Christopher D Williams, Kalon Gopinadhan, Yang Su, Christie T Cherian, James Dix, Eric Prestat, Sarah J Haigh, Irina V Grigorieva, et al. Tunable sieving of ions using graphene oxide membranes. *Nature nanotechnology*, 12(6):546–550, 2017.

[38] Xuesong Li, Yanwu Zhu, Weiwei Cai, Mark Borysiak, Boyang Han, David Chen, Richard D Piner, Luigi Colombo, and Rodney S Ruoff. Transfer of large-area graphene films for high-performance transparent conductive electrodes. *Nano letters*, 9(12):4359–4363, 2009.

[39] Tobias Stauber, Numo MR Peres, and Andre K Geim. Optical conductivity of graphene in the visible region of the spectrum. *Physical Review B*, 78(8):085432, 2008.

[40] Farhan Rana. Graphene terahertz plasmon oscillators. *IEEE Transactions on Nanotechnology*, 7(1):91–99, 2008.

[41] Kin Fai Mak, Matthew Y Sfeir, Yang Wu, Chun Hung Lui, James A Misewich, and Tony F Heinz. Measurement of the optical conductivity of graphene. *Physical review letters*, 101(19):196405, 2008.

[42] F Javier Garcia de Abajo. Graphene plasmonics: challenges and opportunities. *Acs Photonics*, 1(3):135–152, 2014.

[43] Alexander N Grigorenko, Marco Polini, and KS Novoselov. Graphene plasmonics. *Nature photonics*, 6(11):749–758, 2012.

[44] Frank HL Koppens, Darrick E Chang, and F Javier García de Abajo. Graphene plasmonics: a platform for strong light–matter interactions. *Nano letters*, 11(8):3370–3377, 2011.

[45] Long Ju, Baisong Geng, Jason Horng, Caglar Girit, Michael Martin, Zhao Hao, Hans A Bechtel, Xiaogan Liang, Alex Zettl, Y Ron Shen, et al. Graphene plasmonics for tunable terahertz metamaterials. *Nature nanotechnology*, 6(10):630–634, 2011.

[46] Tony Low and Phaedon Avouris. Graphene plasmonics for terahertz to mid-infrared applications. *ACS nano*, 8(2):1086–1101, 2014.

[47] Zhe Fei, AS Rodin, Gregory O Andreev, Wenzhong Bao, AS McLeod, M Wagner, LM Zhang, Zeng Zhao, M Thiemens, Gerardo Dominguez, et al. Gate-tuning of graphene plasmons revealed by infrared nano-imaging. *Nature*, 487(7405):82–85, 2012.

[48] Gwan-Hyoung Lee, Young-Jun Yu, Xu Cui, Nicholas Petrone, Chul-Ho Lee, Min Sup Choi, Dae-Yeong Lee, Changgu Lee, Won Jong Yoo, Kenji Watanabe, et al. Flexible and transparent mos2 field-effect transistors on hexagonal boron nitride-graphene heterostructures. *ACS nano*, 7(9):7931–7936, 2013.

[49] Cory R Dean, Andrea F Young, Inanc Meric, Chris Lee, Lei Wang, Sebastian Sorgenfrei, Kenji Watanabe, Takashi Taniguchi, Phillip Kim, Kenneth L Shepard, et al. Boron nitride substrates for high-quality graphene electronics. *Nature nanotechnology*, 5(10):722–726, 2010.

[50] Thanasis Georgiou, Rashid Jalil, Branson D Belle, Liam Britnell, Roman V Gorbachev, Sergey V Morozov, Yong-Jin Kim, Ali Gholinia, Sarah J Haigh, Oleg Makarovsky, et al. Vertical field-effect transistor based on graphene–ws2 heterostructures for flexible and transparent electronics. *Nature nanotechnology*, 8(2):100–103, 2013.

[51] Woo Jong Yu, Yuan Liu, Hailong Zhou, Anxiang Yin, Zheng Li, Yu Huang, and Xiangfeng Duan. Highly efficient gate-tunable photocurrent generation in vertical heterostructures of layered materials. *Nature nanotechnology*, 8(12):952–958, 2013.

[52] Ya-Ning Ren, Yu Zhang, Yi-Wen Liu, and Lin He. Twistronics in graphene-based van der waals structures. *Chinese Physics B*, 29(11):117303, 2020.

[53] Simone Fratini and Francisco Guinea. Substrate-limited electron dynamics in graphene. *Physical Review B*, 77(19):195415, 2008.

[54] Jian-Hao Chen, Chaun Jang, Shudong Xiao, Masa Ishigami, and Michael S Fuhrer. Intrinsic and extrinsic performance limits of graphene devices on sio2. *Nature nanotechnology*, 3(4):206–209, 2008.

[55] Lei Wang, I Meric, PY Huang, Q Gao, Y Gao, H Tran, T Taniguchi, Kenji Watanabe, LM Campos, DA Muller, et al. One-dimensional electrical contact to a two-dimensional material. *Science*, 342(6158):614–617, 2013.

[56] Kenji Watanabe, Takashi Taniguchi, and Hisao Kanda. Direct-bandgap properties and evidence for ultraviolet lasing of hexagonal boron nitride single crystal. *Nature materials*, 3(6):404–409, 2004.

[57] Takashi Taniguchi and Kenji Watanabe. Synthesis of high-purity boron nitride single crystals under high pressure by using ba–bn solvent. *Journal of crystal growth*, 303(2):525–529, 2007.

[58] Leonardo Martini, Vaidotas Mišeikis, David Esteban, Jon Azpeitia, Sergio Pezzini, Paolo Paletti, Michał W Ochapski, Domenica Convertino, Mar Garcia Hernandez, Ignacio Jimenez, et al. Scalable high-mobility graphene/hbn heterostructures. *ACS Applied Materials & Interfaces*, 15(31):37794–37801, 2023.

[59] CR Woods, Liam Britnell, Axel Eckmann, RS Ma, JC Lu, HM Guo, X Lin, GL Yu, Y Cao, Roman V Gorbachev, et al. Commensurate–incommensurate transition in graphene on hexagonal boron nitride. *Nature physics*, 10(6):451–456, 2014.

[60] RV Gorbachev, JCW Song, GL Yu, AV Kretinin, F Withers, Y Cao, A Mishchenko, IV Grigorieva, Konstantin S Novoselov, LS Levitov, et al. Detecting topological currents in graphene superlattices. *Science*, 346(6208):448–451, 2014.

[61] Liam Britnell, RV Gorbachev, Rashid Jalil, BD Belle, Fredrik Schedin, Artem Mishchenko, Thanasis Georgiou, MI Katsnelson, Laurence Eaves, SV Morozov, et al. Field-effect tunneling transistor based on vertical graphene heterostructures. *Science*, 335(6071):947–950, 2012.

[62] Matthew Yankowitz, Jiamin Xue, Daniel Cormode, Javier D Sanchez-Yamagishi, K Watanabe, T Taniguchi, Pablo Jarillo-Herrero, Philippe Jacquod, and Brian J LeRoy. Emergence of superlattice dirac points in graphene on hexagonal boron nitride. *Nature physics*, 8(5):382–386, 2012.

[63] RV Gorbachev, Al K Geim, MI Katsnelson, KS Novoselov, T Tudorovskiy, IV Grigorieva, AH MacDonald, SV Morozov, K Watanabe, T Taniguchi, et al. Strong coulomb drag and broken symmetry in double-layer graphene. *Nature Physics*, 8(12):896–901, 2012.

[64] Fengnian Xia, Han Wang, Di Xiao, Madan Dubey, and Ashwin Ramasubramaniam. Two-dimensional material nanophotonics. *Nature photonics*, 8(12):899–907, 2014.

[65] FHL Koppens, Thomas Mueller, Ph Avouris, AC Ferrari, M Serena Vitiello, and M Polini. Photodetectors based on graphene, other two-dimensional materials and hybrid systems. *Nature nanotechnology*, 9(10):780–793, 2014.

[66] Thomas Mueller, Fengnian Xia, and Phaedon Avouris. Graphene photodetectors for high-speed optical communications. *Nature photonics*, 4(5):297–301, 2010.

[67] Nathan Youngblood, Che Chen, Steven J Koester, and Mo Li. Waveguide-integrated black phosphorus photodetector with high responsivity and low dark current. *Nature photonics*, 9(4):247–252, 2015.

[68] Marcus Freitag, Tony Low, Wenjuan Zhu, Hugen Yan, Fengnian Xia, and Phaedon Avouris. Photocurrent in graphene harnessed by tunable intrinsic plasmons. *Nature communications*, 4(1):1951, 2013.

[69] LA Ponomarenko, RV Gorbachev, GL Yu, DC Elias, R Jalil, AA Patel, A Mishchenko, AS Mayorov, CR Woods, JR Wallbank, et al. Cloning of dirac fermions in graphene superlattices. *Nature*, 497(7451):594–597, 2013.

[70] Benjamin Hunt, Javier D Sanchez-Yamagishi, Andrea F Young, Matthew Yankowitz, Brian J LeRoy, Kenji Watanabe, Takashi Taniguchi, Pilkyung Moon, Mikito Koshino, Pablo Jarillo-Herrero, et al. Massive dirac fermions and hofstadter butterfly in a van der waals heterostructure. *Science*, 340(6139):1427–1430, 2013.

[71] LA Ponomarenko, R Yang, RV Gorbachev, P Blake, AS Mayorov, KS Novoselov, MI Katsnelson, and AK Geim. Density of states and zero landau level probed through capacitance of graphene. *Physical Review Letters*, 105(13):136801, 2010.

[72] Alexander V Kolobov and Junji Tominaga. *Two-dimensional transition-metal dichalcogenides*, volume 239. Springer, 2016.

[73] Manish Chhowalla, Zhongfan Liu, and Hua Zhang. Two-dimensional transition metal dichalcogenide (tmd) nanosheets. *Chemical Society Reviews*, 44(9):2584–2586, 2015.

[74] Divya Monga, Surbhi Sharma, Nagaraj P Shetti, Soumen Basu, Kakarla Raghava Reddy, and Tejraj M Aminabhavi. Advances in transition metal dichalcogenide-based two-dimensional nanomaterials. *Materials Today Chemistry*, 19:100399, 2021.

[75] Xidong Duan, Chen Wang, Anlian Pan, Ruqin Yu, and Xiangfeng Duan. Two-dimensional transition metal dichalcogenides as atomically thin semiconductors: opportunities and challenges. *Chemical Society Reviews*, 44(24):8859–8876, 2015.

[76] Julia Gusakova, Xingli Wang, Li Lynn Shiau, Anna Krivosheeva, Victor Shaposhnikov, Victor Borisenko, Vasilii Gusakov, and Beng Kang Tay. Electronic properties of bulk and monolayer tmds: theoretical study within dft framework (gvj-2e method). *physica status solidi (a)*, 214(12):1700218, 2017.

[77] Ruitao Lv, Joshua A Robinson, Raymond E Schaak, Du Sun, Yifan Sun, Thomas E Mallouk, and Mauricio Terrones. Transition metal dichalcogenides and beyond: synthesis, properties, and applications of single-and few-layer nanosheets. *Accounts of chemical research*, 48(1):56–64, 2015.

[78] Matteo Bosi. Growth and synthesis of mono and few-layers transition metal dichalcogenides by vapour techniques: a review. *RSC Advances*, 5(92):75500–75518, 2015.

[79] Yumeng Shi, Henan Li, and Lain-Jong Li. Recent advances in controlled synthesis of two-dimensional transition metal dichalcogenides via vapour deposition techniques. *Chemical Society Reviews*, 44(9):2744–2756, 2015.

[80] Liyong Niu, Jonathan N Coleman, Hua Zhang, Hyeonsuk Shin, Manish Chhowalla, and Zijian Zheng. Production of two-dimensional nanomaterials via liquid-based direct exfoliation. *Small*, 12(3):272–293, 2016.

[81] Ignacio Gutiérrez Lezama, Ashish Arora, Alberto Ubaldini, Céline Barreteau, Enrico Giannini, Marek Potemski, and Alberto F Morpurgo. Indirect-to-direct band gap crossover in few-layer mote2. *Nano letters*, 15(4):2336–2342, 2015.

[82] Elena Blundo, Marco Felici, Tanju Yildirim, Giorgio Pettinari, Davide Tedeschi, Antonio Miriametro, B Liu, W Ma, Y Lu, and Antonio Polimeni. Evidence of the direct-to-indirect band gap transition in strained two-dimensional ws 2, mos 2, and wse 2. *Physical review research*, 2(1):012024, 2020.

[83] Yajing Sun, Dong Wang, and Zhigang Shuai. Indirect-to-direct band gap crossover in few-layer transition metal dichalcogenides: a theoretical prediction. *The Journal of Physical Chemistry C*, 120(38):21866–21870, 2016.

[84] Qing Hua Wang, Kourosh Kalantar-Zadeh, Andras Kis, Jonathan N Coleman, and Michael S Strano. Electronics and optoelectronics of two-dimensional transition metal dichalcogenides. *Nature nanotechnology*, 7(11):699–712, 2012.

[85] Yu Wang, Ling Wang, Xin Zhang, Xuejing Liang, Yiyu Feng, and Wei Feng. Two-dimensional nanomaterials with engineered bandgap: Synthesis, properties, applications. *Nano Today*, 37:101059, 2021.

[86] Minh Dao Tran, Ji-Hee Kim, and Young Hee Lee. Tailoring photoluminescence of monolayer transition metal dichalcogenides. *Current Applied Physics*, 16(9):1159–1174, 2016.

[87] Kathleen M McCreary, Aubrey T Hanbicki, Glenn G Jernigan, James C Culbertson, and Berend T Jonker. Synthesis of large-area ws2 monolayers with exceptional photoluminescence. *Scientific reports*, 6(1):19159, 2016.

[88] A Steinhoff, J-H Kim, F Jahnke, M Rosner, D-S Kim, Ch Lee, Gang Hee Han, Mun Seok Jeong, TO Wehling, and C Gies. Efficient excitonic photoluminescence in direct and indirect band gap monolayer mos2. *Nano letters*, 15(10):6841–6847, 2015.

[89] Carmen Palacios-Berraquero and Carmen Palacios-Berraquero. Atomically-thin quantum light emitting diodes. *Quantum confined excitons in 2-dimensional materials*, pages 71–89, 2018.

[90] S Schwarz, Aleksey Kozikov, Freddie Withers, JK Maguire, AP Foster, S Dufferwiel, Lee Hague, MN Makhonin, LR Wilson, AK Geim, et al. Electrically pumped single-defect light emitters in wse2. *2D Materials*, 3(2):025038, 2016.

[91] Kin Fai Mak and Jie Shan. Photonics and optoelectronics of 2d semiconductor transition metal dichalcogenides. *Nature Photonics*, 10(4):216–226, 2016.

[92] Mathieu Massicotte, Fabien Vialla, Peter Schmidt, Mark B Lundeberg, Simone Latini, Sten Haastrup, Mark Danovich, Diana Davydovskaya, Kenji Watanabe, Takashi Taniguchi, et al. Dissociation of two-dimensional excitons in monolayer wse2. *Nature communications*, 9(1):1633, 2018.

[93] Delphine Pommier, Rémi Bretel, Luis E Parra López, Florentin Fabre, Andrew Mayne, Elizabeth Boer-Duchemin, Gérald Dujardin, Guillaume Schull, Stéphane Berciaud, and Eric Le Moal. Scanning tunneling microscope-induced excitonic luminescence of a two-dimensional semiconductor. *Physical review letters*, 123(2):027402, 2019.

[94] Gregory D Scholes and Garry Rumbles. Excitons in nanoscale systems. *Nature materials*, 5(9):683–696, 2006.

[95] PJ Dean, B Fischer, DC Herbert, J Lagois, and PY Yu. *Excitons*, volume 14. Springer Science & Business Media, 2012.

[96] Maurício FC Martins Quintela and Nuno MR Peres. A colloquium on the variational method applied to excitons in 2d materials. *The European Physical Journal B*, 93:1–16, 2020.

[97] Xiaoyang Zheng and Xian Zhang. Excitons in two-dimensional materials. *Advances in Condensed-Matter and Materials Physics-Rudimentary Research to Topical Technology*, 2019.

[98] Galan Moody, John Schaibley, and Xiaodong Xu. Exciton dynamics in monolayer transition metal dichalcogenides. *JOSA B*, 33(7):C39–C49, 2016.

[99] F Schöne, S-O Krüger, P Grünwald, H Stolz, S Scheel, M Aßmann, J Heckötter, J Thewes, D Fröhlich, and M Bayer. Deviations of the exciton level spectrum in cu 2 o from the hydrogen series. *Physical Review B*, 93(7):075203, 2016.

[100] Jai Singh and Jai Singh. Theory of excitons. *Excitation Energy Transfer Processes in Condensed Matter: Theory and Applications*, pages 1–45, 1994.

[101] Chunxiao Cong, Jingzhi Shang, Yanlong Wang, and Ting Yu. Optical properties of 2d semiconductor ws2. *Advanced Optical Materials*, 6(1):1700767, 2018.

[102] Alejandro Molina-Sánchez, Maurizia Palummo, Andrea Marini, and Ludger Wirtz. Temperature-dependent excitonic effects in the optical properties of single-layer mos 2. *Physical Review B*, 93(15):155435, 2016.

[103] Ke Xiao, Tengfei Yan, Qiye Liu, Siyuan Yang, Chiming Kan, Ruihuan Duan, Zheng Liu, and Xiaodong Cui. Many-body effect on optical properties of monolayer molybdenum diselenide. *The Journal of Physical Chemistry Letters*, 12(10):2555–2561, 2021.

[104] Thomas Mueller and Ermin Malic. Exciton physics and device application of two-dimensional transition metal dichalcogenide semiconductors. *npj 2D Materials and Applications*, 2(1):29, 2018.

[105] Weihao Zheng, Ying Jiang, Xuelu Hu, Honglai Li, Zhouxiaosong Zeng, Xiao Wang, and Anlian Pan. Light emission properties of 2d transition metal dichalcogenides: fundamentals and applications. *Advanced Optical Materials*, 6(21):1800420, 2018.

[106] K Kośmider, Jhon W González, and Joaquın Fernández-Rossier. Large spin splitting in the conduction band of transition metal dichalcogenide monolayers. *Physical Review B*, 88(24):245436, 2013.

[107] Rafael Roldan, M Pilar López-Sancho, Francisco Guinea, Emmanuele Cappelluti, Jose Angel Silva-Guillén, and Pablo Ordejón. Momentum dependence of spin–orbit interaction effects in single-layer and multi-layer transition metal dichalcogenides. *2D Materials*, 1(3):034003, 2014.

[108] Zhiyong Y Zhu, Yingchun C Cheng, and Udo Schwingenschlögl. Giant spin-orbit-induced spin splitting in two-dimensional transition-metal dichalcogenide semiconductors. *Physical Review B*, 84(15):153402, 2011.

[109] Ting Cao, Gang Wang, Wenpeng Han, Huiqi Ye, Chuanrui Zhu, Junren Shi, Qian Niu, Pingheng Tan, Enge Wang, Baoli Liu, et al. Valley-selective circular dichroism of monolayer molybdenum disulphide. *Nature communications*, 3(1):887, 2012.

[110] Hualing Zeng, Junfeng Dai, Wang Yao, Di Xiao, and Xiaodong Cui. Valley polarization in mos2 monolayers by optical pumping. *Nature nanotechnology*, 7(8):490–493, 2012.

[111] Hanan Dery and Yang Song. Polarization analysis of excitons in monolayer and bilayer transition-metal dichalcogenides. *Physical Review B*, 92(12):125431, 2015.

[112] Kathleen M McCreary, Aubrey T Hanbicki, Saujan V Sivaram, and Berend T Jonker. A-and b-exciton photoluminescence intensity ratio as a measure of sample quality for transition metal dichalcogenide monolayers. *Apl Materials*, 6(11), 2018.

[113] AT Hanbicki, M Currie, G Kioseoglou, AL Friedman, and BT Jonker. Measurement of high exciton binding energy in the monolayer transition-metal dichalcogenides ws2 and wse2. *Solid State Communications*, 203:16–20, 2015.

[114] Liam Britnell, Roman V Gorbachev, Rashid Jalil, Branson D Belle, Fred Schedin, Mikhail I Katsnelson, Laurence Eaves, Sergey V Morozov, Alexander S Mayorov, Nuno MR Peres, et al. Electron tunneling through ultrathin boron nitride crystalline barriers. *Nano letters*, 12(3):1707–1710, 2012.

[115] L Britnell, RV Gorbachev, AK Geim, LA Ponomarenko, A Mishchenko, MT Greenaway, TM Fromhold, KS Novoselov, and Laurence Eaves. Resonant tunnelling and negative differential conductance in graphene transistors. *Nature communications*, 4(1):1794, 2013.

[116] Artem Mishchenko, JS Tu, Y Cao, Roman V Gorbachev, JR Wallbank, MT Greenaway, VE Morozov, SV Morozov, MJ Zhu, SL Wong, et al. Twist-controlled resonant tunnelling in graphene/boron nitride/graphene heterostructures. *Nature nanotechnology*, 9(10):808–813, 2014.

[117] LA Ponomarenko, AK Geim, AA Zhukov, Rashid Jalil, SV Morozov, KS Novoselov, IV Grigorieva, EH Hill, VV Cheianov, VI FalKo, et al. Tunable metal–insulator transition in double-layer graphene heterostructures. *Nature Physics*, 7(12):958–961, 2011.

[118] Evgeny E Vdovin, A Mishchenko, MT Greenaway, MJ Zhu, D Ghazaryan, A Misra, Y Cao, SV Morozov, Oleg Makarovsky, TM Fromhold, et al. Phonon-assisted resonant tunneling of electrons in graphene–boron nitride transistors. *Physical review letters*, 116(18):186603, 2016.

[119] Mei Ge and Chen Si. Mechanical and electronic properties of lateral graphene and hexagonal boron nitride heterostructures. *Carbon*, 136:286–291, 2018.

[120] AP Durajski and AE Auguścik. Electronic properties of graphene/hbn heterostructures with in-plane displacement. *Acta Physica Polonica, A.*, 138(2), 2020.

[121] Dong Zhang, Dong-Bo Zhang, Fuhua Yang, Hai-Qing Lin, Hongqi Xu, and Kai Chang. Interface engineering of electronic properties of graphene/boron nitride lateral heterostructures. *2D Materials*, 2(4):041001, 2015.

[122] Jagoda Sławińska, Ilona Zasada, and Zbigniew Klusek. Energy gap tuning in graphene on hexagonal boron nitride bilayer system. *Physical Review B*, 81(15):155433, 2010.

[123] Freddie Withers, Osvaldo Del Pozo-Zamudio, Artem Mishchenko, Aiden P Rooney, Ali Gholinia, K Watanabe, Takashi Taniguchi, Sarah J Haigh, AK Geim, AI Tartakovskii, et al. Light-emitting diodes by band-structure engineering in van der waals heterostructures. *Nature materials*, 14(3):301–306, 2015.

[124] Jingang Wang, Fengcai Ma, Wenjie Liang, and Mengtao Sun. Electrical properties and applications of graphene, hexagonal boron nitride (h-bn), and graphene/h-bn heterostructures. *Materials Today Physics*, 2:6–34, 2017.

[125] Shinpei Ogawa, Shoichiro Fukushima, and Masaaki Shimatani. Hexagonal boron nitride for photonic device applications: a review. *Materials*, 16(5):2005, 2023.

[126] Hong Wang, Fucai Liu, Wei Fu, Zheyu Fang, Wu Zhou, and Zheng Liu. Two-dimensional heterostructures: fabrication, characterization, and application. *Nanoscale*, 6(21):12250–12272, 2014.

[127] Kyunghee Choi, Young Tack Lee, and Seongil Im. Two-dimensional van der waals nanosheet devices for future electronics and photonics. *Nano Today*, 11(5):626–643, 2016.

[128] Liam Britnell, Roman V Gorbachev, Rashid Jalil, Branson D Belle, Fred Schedin, Mikhail I Katsnelson, Laurence Eaves, Sergey V Morozov, Alexander S Mayorov, Nuno MR Peres, et al. Atomically thin boron nitride: a tunnelling barrier for graphene devices. *arXiv preprint arXiv:1202.0735*, 2012.

[129] Lujun Wang, Sotirios Papadopoulos, Fadil Iyikanat, Jian Zhang, Jing Huang, Takashi Taniguchi, Kenji Watanabe, Michel Calame, Mickael L Perrin, F Javier García de Abajo, et al. Exciton-assisted electron tunnelling in van der waals heterostructures. *Nature Materials*, 22(9):1094–1099, 2023.

[130] B Amorim, RM Ribeiro, and NMR Peres. Multiple negative differential conductance regions and inelastic phonon assisted tunneling in graphene/h- bn/graphene structures. *Physical Review B*, 93(23):235403, 2016.

[131] LEF Foa Torres, HM Pastawski, and SS Makler. Tuning a resonance in fock space: Optimization of phonon emission in a resonant-tunneling device. *Physical Review B*, 64(19):193304, 2001.

[132] Sergio S Makler, MI Vasilevskiy, EV Anda, DE Tuyarot, J Weberszpil, and HM Pastawski. A source of terahertz coherent phonons. *Journal of Physics: Condensed Matter*, 10(26):5905, 1998.

[133] Markus Parzefall, Áron Szabó, Takashi Taniguchi, Kenji Watanabe, Mathieu Luisier, and Lukas Novotny. Light from van der waals quantum tunneling devices. *Nature communications*, 10(1):292, 2019.

[134] Qilin Yuan, Ting Wang, Panlong Yu, Hanzhuang Zhang, Han Zhang, and Wenyu Ji. A review on the electroluminescence properties of quantum-dot light-emitting diodes. *Organic Electronics*, 90:106086, 2021.

[135] Su-Beom Song, Sangho Yoon, So Young Kim, Sera Yang, Seung-Young Seo, Soonyoung Cha, Hyeon-Woo Jeong, Kenji Watanabe, Takashi Taniguchi, Gil-Ho Lee, et al. Deep-ultraviolet electroluminescence and photocurrent generation in graphene/hbn/graphene heterostructures. *Nature Communications*, 12(1):7134, 2021.

[136] O Del Pozo-Zamudio, A Genco, S Schwarz, F Withers, PM Walker, T Godde, RC Schofield, AP Rooney, E Prestat, K Watanabe, et al. Electrically pumped wse2-based light-emitting van der waals heterostructures embedded in monolithic dielectric microcavities. *2D Materials*, 7(3):031006, 2020.

[137] Junyong Wang, Ivan Verzhbitskiy, and Goki Eda. Electroluminescent devices based on 2d semiconducting transition metal dichalcogenides. *Advanced Materials*, 30(47):1802687, 2018.

[138] RS Sundaram, M Engel, A Lombardo, R Krupke, AC Ferrari, Ph Avouris, and M Steiner. Electroluminescence in single layer mos2. *Nano letters*, 13(4):1416–1421, 2013.

[139] Lukas Dobusch, Simone Schuler, Vasili Perebeinos, and Thomas Mueller. Thermal light emission from monolayer mos2. *Advanced Materials*, 29(31):1701304, 2017.

[140] Sanghyun Jo, Nicolas Ubrig, Helmuth Berger, Alexey B Kuzmenko, and Alberto F Morpurgo. Mono- and bilayer ws2 light-emitting transistors. *Nano letters*, 14(4):2019–2025, 2014.

[141] Der-Hsien Lien, Matin Amani, Sujay B Desai, Geun Ho Ahn, Kevin Han, Jr-Hau He, Joel W Ager III, Ming C Wu, and Ali Javey. Large-area and bright pulsed electroluminescence in monolayer semiconductors. *Nature communications*, 9(1):1229, 2018.

[142] Malte Selig, Gunnar Berghäuser, Archana Raja, Philipp Nagler, Christian Schüller, Tony F Heinz, Tobias Korn, Alexey Chernikov, Ermin Malic, and Andreas Knorr. Excitonic linewidth and coherence lifetime in monolayer transition metal dichalcogenides. *Nature communications*, 7(1):13279, 2016.

[143] Maurizia Palummo, Marco Bernardi, and Jeffrey C Grossman. Exciton radiative lifetimes in two-dimensional transition metal dichalcogenides. *Nano letters*, 15(5):2794–2800, 2015.

[144] Yu Ye, Ziliang Ye, Majid Gharghi, Xiaobo Yin, Hanyu Zhu, Mervin Zhao, and Xiang Zhang. Exciton-related electroluminescence from monolayer mos2. In *CLEO: Science and Innovations*, pages STh4B–4. Optica Publishing Group, 2014.

[145] James Howarth. *Exciton Dynamics in Van der Waals Heterostructures*. The University of Manchester (United Kingdom), 2019.

[146] Leonid Keldysh et al. Diagram technique for nonequilibrium processes. *Sov. Phys. JETP*, 20(4):1018–1026, 1965.

[147] L Kadanoff and G Baym. Quantum statistical mechanics: Green's function method in equilibrium and nonequilibrium problems, 1989.

[148] H. Haug and A.P. Jauho. *Quantum Kinetics in Transport and Optics of Semiconductors*. Springer Series in Solid-State Sciences. Springer Berlin Heidelberg, 2007.

[149] G. Stefanucci and R. van Leeuwen. *Nonequilibrium Many-Body Theory of Quantum Systems: A Modern Introduction*. Cambridge University Press, 2013.

[150] Gianluca Stefanucci and Carl-Olof Almbladh. Time-dependent partition-free approach in resonant tunneling systems. *Phys. Rev. B*, 69:195318, May 2004.

[151] CNRPC Caroli, Ro Combescot, Ph Nozieres, and D Saint-James. Direct calculation of the tunneling current. *Journal of Physics C: Solid State Physics*, 4(8):916, 1971.

[152] Václav Špička, Bedřich Velický, and Anděla Kalvová. Electron systems out of equilibrium: Nonequilibrium green's function approach. *International Journal of Modern Physics B*, 28(23):1430013, 2014.

[153] R. van Leeuwen, N.E. Dahlen, G. Stefanucci, C.-O. Almbladh, and U. von Barth. *Introduction to the Keldysh Formalism*, pages 33–59. Springer Berlin Heidelberg, Berlin, Heidelberg, 2006.

[154] Michael Ridley, N Walter Talarico, Daniel Karlsson, N Lo Gullo, and Riku Tuovinen. A many-body approach to transport in quantum systems: from the transient regime to the stationary state. *Journal of Physics A: Mathematical and Theoretical*, 55(27):273001, 2022.

[155] Alex Kamenev. *Field theory of non-equilibrium systems*. Cambridge University Press, 2023.

[156] Antti-Pekka Jauho, Ned S. Wingreen, and Yigal Meir. Time-dependent transport in interacting and noninteracting resonant-tunneling systems. *Phys. Rev. B*, 50:5528–5544, Aug 1994.

[157] Rolf Landauer. Electrical resistance of disordered one-dimensional lattices. *The Philosophical Magazine: A Journal of Theoretical Experimental and Applied Physics*, 21(172):863–867, 1970.

[158] C Caroli, R Combescot, D Lederer, P Nozieres, and D Saint-James. A direct calculation of the tunnelling current. ii. free electron description. *Journal of Physics C: Solid State Physics*, 4(16):2598, 1971.

[159] R Combescot. A direct calculation of the tunnelling current. iii. effect of localized impurity states in the barrier. *Journal of Physics C: Solid State Physics*, 4(16):2611, 1971.

[160] CNRPC Caroli, R Combescot, Ph Nozières, and D Saint-James. A direct calculation of the tunnelling current: Iv. electron-phonon interaction effects. *Journal of Physics C: Solid State Physics*, 5(1):21, 1972.

[161] VJ Goldman, DC Tsui, and JE Cunningham. Evidence for lo-phonon-emission-assisted tunneling in double-barrier heterostructures. *Physical Review B*, 36(14):7635, 1987.

[162] VJ Goldman, DC Tsui, and JE Cunningham. Observation of intrinsic bistability in resonant tunneling structures. *Physical Review Letters*, 58(12):1256, 1987.

[163] SK Khanna and John Lambe. Inelastic electron tunneling spectroscopy. *Science*, 220(4604):1345–1351, 1983.

[164] Mark A Reed. Inelastic electron tunneling spectroscopy. *Materials today*, 11(11):46–50, 2008.

[165] Randall M Feenstra, Debdeep Jena, and Gong Gu. Single-particle tunneling in doped graphene-insulator-graphene junctions. *Journal of Applied Physics*, 111(4), 2012.

[166] V Enaldiev, A Bylinkin, and D Svintsov. Plasmon-assisted resonant tunneling in graphene-based heterostructures. *Physical Review B*, 96(12):125437, 2017.

[167] Luis Brey. Coherent tunneling and negative differential conductivity in a graphene/h-bn/graphene heterostructure. *Physical Review Applied*, 2(1):014003, 2014.

[168] XL Yang, SH Guo, FT Chan, KW Wong, and WY Ching. Analytic solution of a two-dimensional hydrogen atom. i. nonrelativistic theory. *Physical Review A*, 43(3):1186, 1991.

[169] Thomas Olsen, Simone Latini, Filip Rasmussen, and Kristian S Thygesen. Simple screened hydrogen model of excitons in two-dimensional materials. *Physical review letters*, 116(5):056401, 2016.

[170] Jun John Sakurai and Jim Napolitano. *Modern quantum mechanics*. Cambridge University Press, 2020.

[171] David J Griffiths. *Introduction to electrodynamics*. Cambridge University Press, 2023.

[172] Fred Jendrzejewski, Selim Jochim, and Matthias Weidemüller. Lecture 18-quantization of the electromagnetic field. *Authorea Preprints*, 2019.

[173] José Nuno S Gomes, Carlos Trallero-Giner, Nuno MR Peres, and Mikhail I Vasilevskiy. Exciton–polaritons of a 2d semiconductor layer in a cylindrical microcavity. *Journal of Applied Physics*, 127(13), 2020.

[174] EV Rut'kov, EY Afanas' eva, and NR Gall. Graphene and graphite work function depending on layer number on re. *Diamond and Related Materials*, 101:107576, 2020.

[175] C Ciuti, V Savona, C Piermarocchi, A Quattropani, and P Schwendimann. Role of the exchange of carriers in elastic exciton-exciton scattering in quantum wells. *Physical Review B*, 58(12):7926, 1998.

[176] Horia D Cornean, Valeriu Moldoveanu, and Claude A Pillet. A dyson equation for non-equilibrium green's functions in the partition-free setting. *physica status solidi (b)*, 256(7):1800447, 2019.

[177] AP Jauho. Introduction to the keldysh nonequilibrium green function technique. *Lect. notes*, 17, 2006.

[178] Bruno Amorim. Lecture notes from qmss 2022 - negf.

[179] Julian Schwinger. Brownian motion of a quantum oscillator. *Journal of Mathematical Physics*, 2(3):407–432, 1961.

[180] David C Langreth et al. Linear and nonlinear electron transport in solids, 1976.

[181] Bruno Amorim. Phonons and electrons in 2d materials and layered structures. 2016.

[182] Peter Rickhaus, Ming-Hao Liu, Marcin Kurpas, Annika Kurzmann, Yongjin Lee, Hiske Overweg, Marius Eich, Riccardo Pisoni, Takashi Taniguchi, Kenji Watanabe, et al. The electronic thickness of graphene. *Science advances*, 6(11):eaay8409, 2020.

[183] Shuichi Ogawa, Takatoshi Yamada, Ryo Kadowaki, Takashi Taniguchi, Tadashi Abukawa, and Yuji Takakuwa. Band alignment determination of bulk h-bn and graphene/h-bn laminates using photo-electron emission microscopy. *Journal of Applied Physics*, 125(14), 2019.

Appendices

Appendix A
Brief introduction to non-equilibrium Green's functions

This appendix was based on Refs. [149, 176, 148, 177, 155, 152, 153, 150, 178].

A.1 Time dependent perturbation theory and contour ordering

The aim of this section is to express the time-dependent quantum average of an operator $\hat{O}(t)$ for a system that at the time $t = t_0$ is placed out equilibrium. For that, we start by assuming that the Hamiltonian of such system can be written as

$$H(t) = H_0 + H_{\text{int}} + V(t) \tag{A.1}$$

where H_0 is the "easy" Hamiltonian of non-interacting particles, H_{int} is a many-body Hamiltonian that takes into account the interactions between particles and $V(t)$ is a time-dependent single-particle term that is switched on at the time $t = t_0$.

For $t < t_0$ the system is described by the density matrix ρ_0 for the grand-canonical ensemble, which is given by

$$\rho(t_0) = \rho_0 = \frac{1}{Z_0} e^{-\beta(H_0 - \mu N)} \tag{A.2}$$

where μ is the chemical potential, N is the number of particles and $Z_0 = \text{Tr}\left[e^{-\beta(H_0-\mu N)}\right]$ is the partition function. Since this is a density matrix for non-interacting particles, Wick's theorem applies. We have ignored the role of interactions in the initial state (although the formalism presented in this section can be adapted to if this assumption is relaxed). Therefore, for $t < t_0$ the expectation value $\langle O \rangle$ is simply given by

$$\langle O \rangle(t) = \text{Tr}\left[\rho_0 \hat{O}(t)\right] \tag{A.3}$$

However, the problem resides in calculating $\langle O \rangle$ for $t > t_0$ because in that case it is given by

$$\langle O \rangle(t) = \text{Tr}\left[\rho(t)\hat{O}\right] \tag{A.4}$$

where $\rho(t)$ is the density matrix accounting the whole Hamiltonian, which obeys

$$i\hbar\frac{d}{dt}\rho(t) = [H(t), \rho(t)] \tag{A.5}$$

In order to tackle this problem, we are going to develop a perturbation scheme in order to evaluate $\langle O \rangle$ for $t > t_0$. To do so, we treat $H_{\text{int}} + V(t)$ as a perturbation to the independent particle Hamiltonian H_0 and we write the density matrix as

$$\rho(t) = U(t, t_0)\,\rho(t_0)\,U(t_0, t) \tag{A.6}$$

where U is the time evolution operator, which satisfies $U(t, t_1)\,U(t_1, t') = U(t, t')$ and $U^{-1}(t, t') = U^{\dagger}(t, t') = U(t', t)$.

Now, it is useful to switch to the interaction picture. In this picture, the operator's time evolution is governed by H_0 and the wave-functions are governed by the so-called S-matrix, which encodes the "difficult" perturbative part of the total Hamiltonian, such that we have

$$U(t, t') = U_0(t, t_0)\,S(t, t')\,U_0(t_0, t') \tag{A.7}$$

with $U_0(t, t') = e^{-iH_0(t-t')/\hbar}$ being the time evolution operator with respect to H_0. The matrix $S(t, t')$ also obeys the following equations

$$i\hbar\frac{d}{dt}S(t, t') = W(t)\,U(t, t') \tag{A.8}$$

$$-i\hbar\frac{d}{dt'}S(t, t') = U(t, t')\,W(t') \tag{A.9}$$

with $S(t, t) = 1$, where

$$W(t) = U_0(t_0, t)\,[V(t) + H_{\text{int}}]\,U(t, t_0) \tag{A.10}$$

corresponds to the perturbation in the interaction picture. The solution of these equations can formally be written as

$$S = \begin{cases} Te^{-i/\hbar\int_{t'}^{t} dt_1 W(t_1)}, & t > t' \\ \bar{T}e^{i/\hbar\int_{t}^{t'} dt_1 W(t_1)}, & t < t' \end{cases} \tag{A.11}$$

where T is the time-ordering operator given by

$$T[A(t_1)\,B(t_2)] = \begin{cases} A(t_1)\,B(t_2), & t_1 > t_2 \\ \zeta B(t_2)\,A(t_1) & t_1 < t_2 \end{cases} \tag{A.12}$$

and $\bar{T}$ is the anti-time-ordering operator given by

$$\bar{T}\left[A\left(t_1\right)B\left(t_2\right)\right]=\begin{cases}\zeta B\left(t_2\right)A\left(t_1\right), & t_1>t_2\\ A\left(t_1\right)B\left(t_2\right) & t_1<t_2\end{cases} \tag{A.13}$$

with $\zeta=\pm1$ for fermions/bosons, respectively.

Thus, in the interaction picture we can write the operator as $O\left(t\right)=U_0\left(t_0,t\right)O\left(t\right)U_0\left(t,t_0\right)$ such that the expectation value becomes

$$\begin{aligned}\left\langle O\right\rangle\left(t\right)&=\mathrm{Tr}\left[\rho\left(t_0\right)S\left(t_0,t\right)O\left(t\right)S\left(t,t_0\right)\right]\\&=\left\langle S\left(t_0,t\right)O\left(t\right)S\left(t,t_0\right)\right\rangle_0\end{aligned} \tag{A.14}$$

where $\left\langle\cdots\right\rangle_0$ is the expectation value regarding ρ_0, that being, with respect to the "easy" Hamiltonian H_0. We remark that by expanding the S-operator in Taylor-series, it would lead to integrals over time of quantities like

$$\left\langle\bar{T}\left[W\left(t_1\right)\cdots W\left(t_n\right)\right]O\left(t\right)T\left[W\left(t_1'\right)\cdots W\left(t_n'\right)\right]\right\rangle_0 \tag{A.15}$$

(with t_i and t_i' between t_0 and t) which means that we have reduced the problem to the evaluation of a series of expectation values with respect to the "simple" density matrix ρ_0, which can be calculating using Wick's theorem. However, notice that we still have two Taylor expansions instead of a single one. We can achieve the single Taylor expansion by introducing the contour $C\equiv\left(t_0,t_{\mathrm{max}}\right)\oplus\left(t_{\mathrm{max}},t_0\right)$ (where t_{max} is greater than any other relevant time variable) that goes from t_0 to t_{max} and then back to t_0, which is shown in Fig. 32.

We remark that formally an operator $O\left(t_+\right)$ with t_+ lying in the forward going branch can be different from the operator $O\left(t_-\right)$ with t_- lying in the backward going branch. However, physical operators $O\left(t^+\right)$ and $O\left(t^-\right)$ lying in the different branches are the same, so that we define the operator $\hat{O}$ with contour arguments as

$$\hat{O}\left(s=t_\pm\right)\equiv\hat{O}\left(t\right) \tag{A.16}$$

such that $\hat{O}\left(t_+\right)=\hat{O}\left(t_-\right)=\hat{O}\left(t\right)$. This contour can be parametrized by its arc length s as

$$t_C\left(s\right)=\begin{cases}t_0+s, & s\in\left[0,t-t_0\right]\\ t-\left(s-t+t_0\right) & s\in\left[t-t_0,2\left(t-t_0\right)\right]\end{cases} \tag{A.17}$$

so that we can rewrite Eq. A.14 as

$$\begin{aligned}\left\langle O\right\rangle\left(t\right)&=\left\langle S\left(t_0,t\right)O\left(t\right)S\left(t,t_0\right)\right\rangle_0\\&=\left\langle S\left(t_0,t\right)S\left(t,t_{\mathrm{max}}\right)S\left(t_{\mathrm{max}},t\right)O\left(t\right)S\left(t,t_0\right)\right\rangle_0\\&=\left\langle T_CS_C\left(t_0,t_0\right)O\left(t\right)\right\rangle_0\end{aligned} \tag{A.18}$$

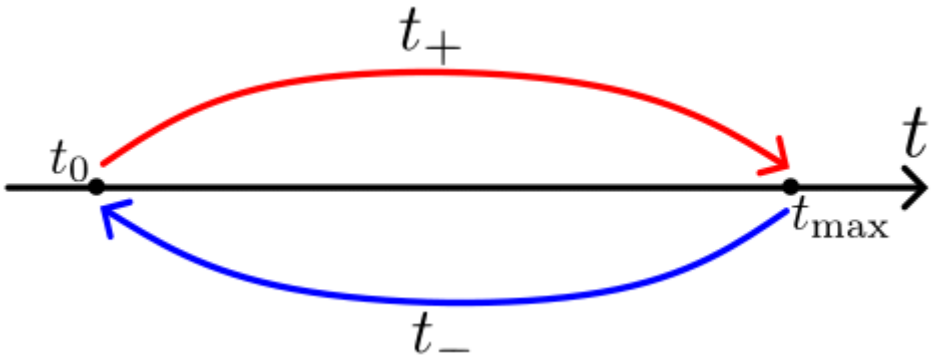


Figure 32: Scheme of the time contour C. The coloured arrows are shifted from the t axis only for visual purposes and the contour follows the real time axis (black). The contour consists in evolving t from an initial time t_0 to a time $t_{\max}$ that is larger than any other relevant time variable. This path is represented by the red arrow and is denoted by t_+. Then, we evolve t from $t_{\max}$ to t_0 again, forming a closed contour. This second path is represented by the blue arrow and is denoted by t_-. Often the variables t_0 and $t_{\max}$ are relaxed to $t_0 \to -\infty$ and $t_{\max} \to +\infty$, which is known as the Schwinger-Keldysh contour. Such choice is made when one is not interested in transient phenomena.

where we have introduced

$$S_C\left(t_0, t_0\right) = T_C e^{-i/\hbar \int_C ds W(s)} \tag{A.19}$$

with $W\left(s\right) \equiv W\left(t_C\left(s\right)\right)$ and T_C being the time-ordering operator in the contour t_C present in Eq. A.17. It is relevant to say that the operator T_C was introduced to book-keeping the operators that appear either time-ordered or anti-time-ordered. We only demand that $t_{\max}$ is greater than any time t for which we want to evalaute $\langle O\left(t\right)\rangle$. Formally, we can extend $t \to +\infty$. Also, if we are not interested in transient dynamics, one can take the limit $t_0 \to -\infty$ ending up with the so called Schwinger-Keldysh contour (developed independently by Schwinger [179] in 1961 and by Keldysh [146] in 1964). Since we are interested in steady-state quantities, we will use the Schwinger-Keldysh contour.

With the introduction of such contour ordering we obtain a single perturbative series expansion $\langle O\rangle\left(t\right)$ as follows

$$\langle O\rangle\left(t\right) = \sum_n \frac{1}{n!}\left(-\frac{i}{\hbar}\right)^n \int_C ds_1 \cdots \int_C ds_n \left\langle T_C W\left(s_1\right) \cdots W\left(s_n\right) O\left(t\right)\right\rangle_0 \tag{A.20}$$

A.2 Contour ordered Green's functions

From Eq. A.18, we can introduce a natural generalization of the real-time single-particle GFs for non-equilibrium theory, which is the contour ordered Green's function, defined as

$$G_{ab}\left(s, s'\right) = -\frac{i}{\hbar}\left\langle T_C c_a\left(s\right) c_b^\dagger\left(s'\right)\right\rangle \tag{A.21}$$

where the time evolution of the operators is now over the contour, satisfying the Heisenberg equation with the contour argument given by

$$\frac{d}{ds}\hat{O}\left(s\right)=\frac{i}{\hbar}\left[H\left(s\right),\hat{O}\left(s\right)\right], \tag{A.22}$$

the contour time evolution operator given by

$$\hat{O}\left(s\right)=U_{C}\left(s_{0},s\right)OU_{C}\left(s,s_{0}\right) \tag{A.23}$$

with $U_{C}\left(s,s'\right)$ obeying the contour Schrödinger equation

$$i\hbar\frac{d}{ds}U_{C}\left(s,s'\right)=H\left(s\right)U\left(s,s'\right) \tag{A.24}$$

$$-i\hbar\frac{d}{ds'}U_{C}\left(s,s'\right)=U\left(s,s'\right)H\left(s'\right) \tag{A.25}$$

where $H\left(s\right)=H\left(t_{C}\left(s\right)\right)$. Such GF with contour ordered arguments can also be perturbatively expanded as in Eq. A.20.

Depending on the position of its arguments (if they lie in the C^{+} or the C^{-} contour), the contour ordered GF reduces to the following real-time GFs : the time ordered GF if both arguments lie in the C^{+} contour

$$G_{ab}\left(t_{+},t'_{+}\right)=-\frac{i}{\hbar}\left\langle T_{C}c_{a}\left(t_{+}\right)c_{b}^{\dagger}\left(t'_{+}\right)\right\rangle =-\frac{i}{\hbar}\left\langle Tc_{a}\left(t\right)c_{b}^{\dagger}\left(t'\right)\right\rangle \equiv G_{ab}^{T}\left(t,t'\right), \tag{A.26}$$

the lesser GF if t is in the C^{+} contour and t' in the C^{-} contour

$$G_{ab}\left(t_{+},t'_{-}\right)=-\frac{i}{\hbar}\left\langle T_{C}c_{a}\left(t_{+}\right)c_{b}^{\dagger}\left(t'_{-}\right)\right\rangle =-\zeta\frac{i}{\hbar}\left\langle c_{b}^{\dagger}\left(t'_{-}\right)c_{a}\left(t_{+}\right)\right\rangle \equiv G_{ab}^{<}\left(t,t'\right), \tag{A.27}$$

the greater GF if t is in the C^{-} contour and t' in the C^{+} contour

$$G_{ab}\left(t_{-},t'_{+}\right)=-\frac{i}{\hbar}\left\langle T_{C}c_{a}\left(t_{-}\right)c_{b}^{\dagger}\left(t'_{+}\right)\right\rangle =-\frac{i}{\hbar}\left\langle c_{a}\left(t_{-}\right)c_{b}^{\dagger}\left(t'_{+}\right)\right\rangle \equiv G_{ab}^{>}\left(t,t'\right) \tag{A.28}$$

and the anti-time ordered GF if both arguments lie in the C^{-} contour

$$G_{ab}\left(t_{-},t'_{-}\right)=-\frac{i}{\hbar}\left\langle T_{C}c_{a}\left(t_{-}\right)c_{b}^{\dagger}\left(t'_{-}\right)\right\rangle =-\frac{i}{\hbar}\left\langle \bar{T}c_{a}\left(t\right)c_{b}^{\dagger}\left(t'\right)\right\rangle \equiv G_{ab}^{\bar{T}}\left(t,t'\right). \tag{A.29}$$

We can cast all these GF's in matrix form where the matrix indices indicate the branch of the contour the time variables are, such as

$$\begin{bmatrix} G_{ab}\left(t_{+},t'_{+}\right) & G_{ab}\left(t_{+},t'_{-}\right)\\ G_{ab}\left(t_{-},t'_{+}\right) & G_{ab}\left(t_{-},t'_{-}\right)\end{bmatrix}=\begin{bmatrix} G_{ab}^{T}\left(t,t'\right) & G_{ab}^{<}\left(t,t'\right)\\ G_{ab}^{>}\left(t,t'\right) & G_{ab}^{\bar{T}}\left(t,t'\right)\end{bmatrix} \tag{A.30}$$

Additionally, all these quantities are also related with each other by the following equation

$$G^{>}_{ab}(t,t') + G^{<}_{ab}(t,t') = G^{T}_{ab}(t,t') + G^{\bar{T}}_{ab}(t,t') \tag{A.31}$$

meaning that there are only three linearly independent GFs, allowing one to choose the most adequate ones for each case. This leads to the use of different conventions throughout the literature. Other two commonly used GFs that we are interested in are the retarded and advanced GFs, defined as

$$G^{R}_{ab}(t,t') \equiv -\frac{i}{\hbar}\Theta(t-t')\left\langle \left[c_a(t), c^{\dagger}_b(t')\right]_{\zeta}\right\rangle \tag{A.32}$$

$$G^{A}_{ab}(t,t') \equiv \frac{i}{\hbar}\Theta(t'-t)\left\langle \left[c_a(t), c^{\dagger}_b(t')\right]_{\zeta}\right\rangle \tag{A.33}$$

For our purposes, we focus on $G^{>}$, $G^{<}$, G^{R} and G^{A}, which are also related by the following equation

$$G^{R}_{ab}(t,t') - G^{A}_{ab}(t,t') = G^{>}_{ab}(t,t') - G^{<}_{ab}(t,t') \tag{A.34}$$

Since the real-time GF's are not all linearly independent, we can eliminate one of them by applying a linear transformation such as

$$\begin{bmatrix} G^{T}_{ab}(t,t') & G^{<}_{ab}(t,t') \\ G^{>}_{ab}(t,t') & G^{\bar{T}}_{ab}(t,t') \end{bmatrix} \rightarrow L^{-1}\cdot \begin{bmatrix} G^{T}_{ab}(t,t') & G^{<}_{ab}(t,t') \\ G^{>}_{ab}(t,t') & G^{\bar{T}}_{ab}(t,t') \end{bmatrix} \cdot Q^{-1} \tag{A.35}$$

where one of those GFs is eliminated by choosing the appropriate L and Q matrix. Since we are interested in working with G^{R}, G^{A} and $G^{<}$, also known as the *RAL* representation, we choose L and Q to be

$$L = \begin{bmatrix} 1 & 0 \\ 1 & -1 \end{bmatrix},\ Q = \begin{bmatrix} 1 & 0 \\ 1 & 1 \end{bmatrix} \tag{A.36}$$

such that

$$L^{-1}\cdot \begin{bmatrix} G^{T}_{ab}(t,t') & G^{<}_{ab}(t,t') \\ G^{>}_{ab}(t,t') & G^{\bar{T}}_{ab}(t,t') \end{bmatrix} \cdot Q^{-1} = \begin{bmatrix} G^{R}_{ab}(t,t') & G^{<}_{ab}(t,t') \\ 0 & G^{A}_{ab}(t,t') \end{bmatrix} \tag{A.37}$$

The contour-ordered GF also obey the Dyson equation, which for a system with interactions and subjected to an external potential reads

$$\begin{aligned} G_{ab}(s,s') = g_{ab}(s,s') &+ \sum_{cd}\int_{C} ds_1 g_{ac}(s,s_1) V_{cd}(s_1) G_{db}(s_1,s') \\ &+ \sum_{cd}\int_{C} ds_1 \int_{C} ds_2 g_{ac}(s,s_1)\Sigma_{cd}(s_1,s_2) G_{db}(s_2,s') \end{aligned} \tag{A.38}$$

We can transform this equation back into the real-time domain by using the matrix representation shown above, which leads to

$$\begin{aligned}
&\begin{bmatrix} G^{T}_{ab}(t,t') & G^{<}_{ab}(t,t') \\ G^{>}_{ab}(t,t') & G^{\bar{T}}_{ab}(t,t') \end{bmatrix} = \begin{bmatrix} g^{T}_{ab}(t,t') & g^{<}_{ab}(t,t') \\ g^{>}_{ab}(t,t') & g^{\bar{T}}_{ab}(t,t') \end{bmatrix} + \\
&+ \sum_{cd} \int dt_1 \begin{bmatrix} g^{T}_{ac}(t,t_1) & g^{<}_{ac}(t,t_1) \\ g^{>}_{ac}(t,t_1) & g^{\bar{T}}_{ac}(t,t_1) \end{bmatrix} V_{cd}(t_1)\,\sigma_z \begin{bmatrix} G^{T}_{db}(t_1,t') & G^{<}_{db}(t_1,t') \\ G^{>}_{db}(t_1,t') & G^{\bar{T}}_{db}(t_1,t') \end{bmatrix} + \\
&+ \sum_{cd} \int dt_1 \int_C dt_2 \begin{bmatrix} g^{T}_{ac}(t,t_1) & g^{<}_{ac}(t,t_1) \\ g^{>}_{ac}(t,t_1) & g^{\bar{T}}_{ac}(t,t_1) \end{bmatrix} \sigma_z \begin{bmatrix} \Sigma^{T}_{cd}(t_1,t_2) & \Sigma^{<}_{cd}(t_1,t_2) \\ \Sigma^{>}_{cd}(t_1,t_2) & \Sigma^{\bar{T}}_{cd}(t_1,t_2) \end{bmatrix} \sigma_z \begin{bmatrix} G^{T}_{db}(t_2,t') & G^{<}_{db}(t_2,t') \\ G^{>}_{db}(t_2,t') & G^{\bar{T}}_{db}(t_2,t') \end{bmatrix}
\end{aligned} \tag{A.39}$$

and by changing to the *RAL* representation we obtain

$$\begin{aligned}
&\begin{bmatrix} G^{R}_{ab}(t,t') & G^{<}_{ab}(t,t') \\ 0 & G^{A}_{ab}(t,t') \end{bmatrix} = \begin{bmatrix} g^{R}_{ab}(t,t') & g^{<}_{ab}(t,t') \\ 0 & g^{A}_{ab}(t,t') \end{bmatrix} + \\
&+ \sum_{cd} \int dt_1 \begin{bmatrix} g^{R}_{ac}(t,t_1) & g^{<}_{ac}(t,t_1) \\ 0 & g^{A}_{ac}(t,t_1) \end{bmatrix} V_{cd}(t_1) \begin{bmatrix} G^{R}_{db}(t_1,t') & G^{<}_{db}(t_1,t') \\ 0 & G^{A}_{db}(t_1,t') \end{bmatrix} + \\
&+ \sum_{cd} \int dt_1 \int dt_2 \begin{bmatrix} g^{R}_{ac}(t,t_1) & g^{<}_{ac}(t,t_1) \\ 0 & g^{A}_{ac}(t,t_1) \end{bmatrix} \begin{bmatrix} \Sigma^{R}_{cd}(t_1,t_2) & \Sigma^{<}_{cd}(t_1,t_2) \\ 0 & \Sigma^{A}_{cd}(t_1,t_2) \end{bmatrix} \begin{bmatrix} G^{R}_{db}(t_2,t') & G^{<}_{db}(t_2,t') \\ 0 & G^{A}_{db}(t_2,t') \end{bmatrix}
\end{aligned} \tag{A.40}$$

From this last equation we can extract the Dyson equation for the retarded/advanced GFs

$$G^{R/A} = g^{R/A} + g^{R/A} \cdot V \cdot G^{R/A} + g^{R/A} \cdot \Sigma^{R/A} \cdot G^{R/A} \tag{A.41}$$

with the " $\cdot$ " encoding the integration over time and the summation over the indices. As for the lesser GF, we have

$$\begin{aligned}
G^{<} = {} & g^{<} + g^{R} \cdot V \cdot G^{<} + g^{<} \cdot V \cdot G^{A} + \\
& + g^{R} \cdot \Sigma^{R} \cdot G^{<} + g^{R} \cdot \Sigma^{<} \cdot G^{A} + g^{<} \cdot \Sigma^{A} \cdot G^{A}
\end{aligned} \tag{A.42}$$

and by acting with the operator $i\hbar\partial_t - H_0$ on this equation and manipulating we obtain

$$\begin{aligned}
G^{<}(t,t') = {} & G^{R}(t,t_0) \cdot G^{<}(t_0,t_0) \cdot G^{A}(t_0,t') \\
& + \int dt_1 \int dt_2 G^{R}(t,t_1) \cdot \Sigma^{<}(t_1,t_2) \cdot G^{A}(t_2,t')
\end{aligned} \tag{A.43}$$

Assuming that the system loses memory of its initial state, that being, $\lim_{t\to\infty} G^R(t,t_0) = \lim_{t\to\infty} G^A(t_0,t) = 0$, we obtain

$$G^<(t,t') = \int dt_1 \int dt_2 G^R(t,t_1)\cdot\Sigma^<(t_1,t_2)\cdot G^A(t_2,t') \tag{A.44}$$

which is known as the Keldysh equation.

A.3 Langreth's rules

As seen in the previous section, it is straightforward to obtain the real-time counter-parts of a single contour-ordered GF, being only a question of determining in which branch of the contour are its arguments. However, for more complicated expressions involving contour-ordered GF's, such as products or convolutions of many contour-ordered GFs, one needs to employ the so-called Langreth's rules in order to obtain its real-time correspondents. We state below, without derivation, some of the more useful ones. For a derivation, an interested reader can check Refs. [180, 148].

For the case of finding a convolution of the type

$$C(s,s') = \int_C ds_1 A(s,s_1) B(s_1,s') \tag{A.45}$$

which is found in the Dyson equation, the lesser/greater components are then given by

$$C^{\lessgtr}(t,t') = \int_C dt_1 \left[A^R(t,t_1) B^{\lessgtr}(t_1,t') + A^{\lessgtr}(t,t_1) B^A(t_1,t')\right] \tag{A.46}$$

and for the retarded/advanced components we have

$$C^{R/A}(t,t') = \int_C dt_1 A^{R/A}(t,t_1) B^{R/A}(t_1,t') \tag{A.47}$$

For a parallel product of the type

$$C(s,s') = A(s,s') B(s,s') \tag{A.48}$$

we have

$$C^{\lessgtr}(t,t') = A^{\lessgtr}(t,t') B^{\lessgtr}(t,t') \tag{A.49}$$

and

$$C^{R/A}(t,t') = A^<(t,t') B^{R/A}(t,t') + A^{R/A}(t,t') B^>(t,t') \tag{A.50}$$

Finally, it is also common to find the anti-parallel product of the form

$$C(s,s') = A(s,s') B(s',s) \tag{A.51}$$

that leads to

$$C^{\lessgtr}(t,t') = A^{\lessgtr}(t,t')\, B^{\gtrless}(t',t) \tag{A.52}$$

and to

$$C^{R/A}(t,t') = A^{<}(t,t')\, B^{R/A}(t',t) + A^{R/A}(t,t')\, B^{<}(t',t) \tag{A.53}$$

A.4 Fock diagram for the electron-boson interaction

In this section we focus on obtaining the Fock diagram for the electron-boson interaction. When interactions are introduced, the electrons feel the presence of the bosons and this leads to a renormalization of their energy or other properties, which alters the potential created by the electrons. On the other hand, the bosons feel this change in the electronic potential, which leads to a change of their properties and the potential created by them, which in turn is felt by the electrons and so forth. We can notice that such interaction creates a loop of renormalizations between the electrons and bosons. In order to arrive to a feasible solution, one needs to truncate this loop up to some degree. For our particular case, we choose to approximate it up to second order. This means that the electrons feel the presence of the bosons, but, because the bosons are in great number or the influence that the electrons have on them is sufficiently small, the bosons do not feel the presence of the electrons, ending here the cause-effect relation between these two entities.

With this being said, we start with the contour ordered electronic GF $G(s,s')$ given by

$$\begin{aligned} G_{ab}(s,s') &= -i\left\langle T_C c_a(s)\, c_b^{\dagger}(s')\right\rangle \\ &= -i\left\langle T_C c_a(s)\, c_b^{\dagger}(s')\, e^{-i\int_C ds_1 H_{\text{int}}(s_1)}\right\rangle_0 \end{aligned} \tag{A.54}$$

where the unperturbed or "easy" Hamiltonian for the free electrons/bosons is given by

$$H_0 = \sum_n \varepsilon_n c_n^{\dagger} c_n + \sum_\lambda \hbar\omega_\lambda a_\lambda^{\dagger} a_\lambda \tag{A.55}$$

and the perturbative interaction Hamiltonian reads

$$H_{\text{int}} = \sum_{\alpha\beta\lambda} M_{\alpha\beta}(\lambda)\, c_\alpha^{\dagger} c_\beta \phi_\lambda \tag{A.56}$$

where all those appearing quantities were previously defined in the main text and the operators are in the interaction picture.

Now, we expand the factor $e^{-i\int_C ds_1 H_{\text{int}}(s_1)}$ in the expression for $G_{ab}(s,s')$, up to second order in

$M(\lambda)$, so that

$$G_{ab}(s,s') = -i\left\langle T_C c_a(s)\, c_b^\dagger(s')\left(1 - i\int_C ds_1 H_{\text{int}}(s_1) + \frac{1}{2}\left(-i\int_C ds_1 H_{\text{int}}(s_1)\right)^2\right)\right\rangle_0$$
$$= -i\left\langle T_C c_a(s)\, c_b^\dagger(s')\left(1 - i\int_C ds_1 H_{\text{int}}(s_1) - \frac{1}{2}\int_C ds_1\int_C ds_2 H_{\text{int}}(s_1) H_{\text{int}}(s_2)\right)\right\rangle_0 \tag{A.57}$$

and by substituting H_{int} by its expression we have

$$G_{ab}(s,s') = -i\left\langle T_C c_a(s)\, c_b^\dagger(s')\right\rangle_0 - \sum_{\alpha\beta\lambda}\int_C ds_1 M_{\alpha\beta}(\lambda)\left\langle T_C c_a(s)\, c_b^\dagger(s')\, c_\alpha^\dagger(s_1)\, c_\beta(s_1)\,\phi_\lambda(s_1)\right\rangle_0$$
$$+\frac{i}{2}\sum_{\alpha_1\beta_1\lambda_1}\sum_{\alpha_2\beta_2\lambda_2} M_{\alpha_1\beta_1}(\lambda_1) M_{\alpha_2\beta_2}(\lambda_2)\cdot$$
$$\cdot\int_C ds_1\int_C ds_2\left\langle T_C c_a(s)\, c_b^\dagger(s')\, c_{\alpha_1}^\dagger(s_1)\, c_{\beta_1}(s_1)\,\phi_{\lambda_1}(s_1)\, c_{\alpha_2}^\dagger(s_2)\, c_{\beta_2}(s_2)\,\phi_{\lambda_2}(s_2)\right\rangle_0 \tag{A.58}$$

We arrived at a point where we need to employ Wick's theorem to write the average of the product as a product of averages of pairs of operators. Notice that in the first order term there is only one bosonic operator, leading to the cancelation of this term. Additionally, we can write the first term as a free-electron GF $g_{ab}(s,s')$ so that we arrive to

$$G_{ab}(s,s') = g_{ab}(s,s')$$
$$+\frac{i}{2}\sum_{\alpha_1\beta_1\lambda_1}\sum_{\alpha_2\beta_2\lambda_2} M_{\alpha_1\beta_1}(\lambda_1) M_{\alpha_2\beta_2}(\lambda_2)\cdot$$
$$\cdot\int_C ds_1\int_C ds_2\left\langle T_C c_a(s)\, c_b^\dagger(s')\, c_{\alpha_1}^\dagger(s_1)\, c_{\beta_1}(s_1)\,\phi_{\lambda_1}(s_1)\, c_{\alpha_2}^\dagger(s_2)\, c_{\beta_2}(s_2)\,\phi_{\lambda_2}(s_2)\right\rangle_0 \tag{A.59}$$

Wick's theorem allows us to write this average as

$$\left\langle T_C c_a(s)\, c_b^\dagger(s')\, c_{\alpha_1}^\dagger(s_1)\, c_{\beta_1}(s_1)\,\phi_{\lambda_1}(s_1)\, c_{\alpha_2}^\dagger(s_2)\, c_{\beta_2}(s_2)\,\phi_{\lambda_2}(s_2)\right\rangle_0$$
$$= \left\langle T_C c_a(s)\, c_b^\dagger(s')\right\rangle_0\left\langle T_C c_{\alpha_1}^\dagger(s_1)\, c_{\beta_1}(s_1)\right\rangle_0\left\langle T_C\phi_{\lambda_1}(s_1)\,\phi_{\lambda_2}(s_2)\right\rangle_0\left\langle T_C c_{\alpha_2}^\dagger(s_2)\, c_{\beta_2}(s_2)\right\rangle_0$$
$$+2\left\langle T_C c_a(s)\, c_{\alpha_1}^\dagger(s_1)\right\rangle_0\left\langle T_C c_{\beta_1}(s_1)\, c_b^\dagger(s')\right\rangle_0\left\langle T_C c_{\beta_2}(s_2)\, c_{\alpha_2}^\dagger(s_2)\right\rangle_0\left\langle T_C\phi_{\lambda_1}(s_1)\,\phi_{\lambda_2}(s_2)\right\rangle_0$$
$$-2\left\langle T_C c_a(s)\, c_{\alpha_1}^\dagger(s_1)\right\rangle_0\left\langle T_C c_{\beta_2}(s_2)\, c_b^\dagger(s')\right\rangle_0\left\langle T_C c_{\beta_1}(s_1)\, c_{\alpha_2}^\dagger(s_2)\right\rangle_0\left\langle T_C\phi_{\lambda_1}(s_1)\,\phi_{\lambda_2}(s_2)\right\rangle_0 \tag{A.60}$$

where the first term corresponds to a disconnected diagram that cancel out. Writing the averages of pairs of operators as GFs we have

$$\left\langle T_C c_a(s)\, c_b^\dagger(s')\, c_{\alpha_1}^\dagger(s_1)\, c_{\beta_1}(s_1)\,\phi_{\lambda_1}(s_1)\, c_{\alpha_2}^\dagger(s_2)\, c_{\beta_2}(s_2)\,\phi_{\lambda_2}(s_2)\right\rangle_0$$
$$= 2g_{a\alpha_1}(s,s_1)\, g_{\beta_1 b}(s_1,s')\, g_{\beta_2\alpha_2}(s_2,s_2)\, d_{\lambda_1\lambda_2}(s_1,s_2)$$
$$-2g_{a\alpha_1}(s,s_1)\, g_{\beta_2 b}(s_2,s')\, g_{\beta_1\alpha_2}(s_1,s_2)\, d_{\lambda_1\lambda_2}(s_1,s_2) \tag{A.61}$$

Plugging this expression into Eq. A.59 we obtain

$$
\begin{aligned}
&G_{ab}(s,s') = g_{ab}(s,s') \\
&+ i \sum_{\alpha_1\beta_1\lambda_1} \sum_{\alpha_2\beta_2\lambda_2} M_{\alpha_1\beta_1}(\lambda_1) M_{\alpha_2\beta_2}(\lambda_2) \int_C ds_1 \int_C ds_2 g_{a\alpha_1}(s,s_1) g_{\beta_1 b}(s_1,s') g_{\beta_2\alpha_2}(s_2,s_2) d_{\lambda_1\lambda_2}(s_1,s_2) \\
&- i \sum_{\alpha_1\beta_1\lambda_1} \sum_{\alpha_2\beta_2\lambda_2} M_{\alpha_1\beta_1}(\lambda_1) M_{\alpha_2\beta_2}(\lambda_2) \int_C ds_1 \int_C ds_2 g_{a\alpha_1}(s,s_1) g_{\beta_2 b}(s_2,s') g_{\beta_1\alpha_2}(s_1,s_2) d_{\lambda_1\lambda_2}(s_1,s_2)
\end{aligned}
\tag{A.62}
$$

where we can ascribe to the second term the so-called Hartree self-energy

$$
\Sigma^H(s_1,s_2) = i \sum_{\alpha_1\beta_1\lambda_1} \sum_{\alpha_2\beta_2\lambda_2} M_{\alpha_1\beta_1}(\lambda_1) M_{\alpha_2\beta_2}(\lambda_2) g_{\beta_2\alpha_2}(s_2,s_2) d_{\lambda_1\lambda_2}(s_1,s_2) \tag{A.63}
$$

and to the third term the Fock self-energy that is given by

$$
\Sigma^F(s_1,s_2) = -i \sum_{\alpha_1\beta_1\lambda_1} \sum_{\alpha_2\beta_2\lambda_2} M_{\alpha_1\beta_1}(\lambda_1) M_{\alpha_2\beta_2}(\lambda_2) g_{\beta_1\alpha_2}(s_1,s_2) d_{\lambda_1\lambda_2}(s_1,s_2) \tag{A.64}
$$

where the diagrams for both contributions are depicted in Fig. 33.

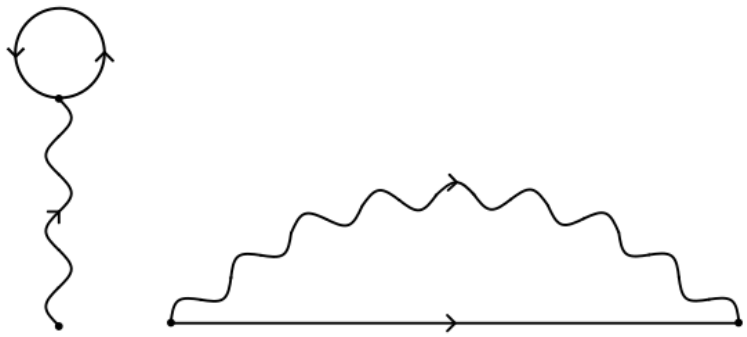


Figure 33: Hartree (left) and Fock (right) diagrams that arise in second order perturbation theory. The curly lines represent the bosonic GF $d_{\lambda_1\lambda_2}(s_1,s_2)$ and the straight lines the electron bare GF $g_{\beta\alpha}$. Notice that in the Hartree contribution, the boson line touches the electron line in just one point, meaning that this interaction is local in time. It can be seen just as a external potential that modifies the electronic energies. As for the Fock contribution, the bosonic line touches the electron line in two points, meaning that the interaction that occurred in one instant will affect the particle in another instant. This diagram has implications in time-dependent observables such as currents, which is the relevant observable in our main discussion.

Notice that the Hartree contribution is local in time (the arguments of the GF in Σ^H are the same), which means that it gives no contribution to time dependent quantities such as currents. This term can rather be understood as a contribution to the external potential of the electron.

$$
\Sigma_{\text{int}}(s_1,s_2) = -i \sum_{\lambda_1\lambda_2} \boldsymbol{M}(\lambda_1) \cdot \boldsymbol{g}(s_1,s_2) \cdot \boldsymbol{M}(\lambda_2) d_{\lambda_1\lambda_2}(s_1,s_2) \tag{A.65}
$$

Therefore, we neglect the Hartree term and we work with the Fock contribution as our main interacting self-energy, which can be written as Additionally, it is customary to adopt the non-crossing approximation, which consists in a summation over all possible diagrams where the bosonic lines do not cross with each other. In practice, it yields a similar expression as the Fock contribution, where we replace $\boldsymbol{g} \rightarrow \boldsymbol{G}$,

$$\Sigma_{\text{int}}\left(s_1, s_2\right) = -i \sum_{\lambda_1 \lambda_2} \boldsymbol{M}\left(\lambda_1\right) \cdot \boldsymbol{G}\left(s_1, s_2\right) \cdot \boldsymbol{M}\left(\lambda_2\right) d_{\lambda_1 \lambda_2}\left(s_1, s_2\right) \tag{A.66}$$

which is the expression that we adopt in the main text.

Appendix B
Electronic wave-function in graphene

We aim to obtain the electronic wave-function in graphene, both the in-plane and out-of-plane components.

As discussed in the introduction, graphene is a 2D material simply composed by carbon atoms covalently bound in a honeycomb structure (shown in Fig. 34 a)) with the nearest neighbor vectors being

$$\boldsymbol{\tau}_1 = \frac{a_g}{\sqrt{3}}\left(\frac{\sqrt{3}}{2}, -\frac{1}{2}\right), \tag{B.1}$$

$$\boldsymbol{\tau}_2 = \frac{a_g}{\sqrt{3}}(0, 1), \tag{B.2}$$

$$\boldsymbol{\tau}_3 = \frac{a_g}{\sqrt{3}}\left(-\frac{\sqrt{3}}{2}, -\frac{1}{2}\right). \tag{B.3}$$

Graphene's Bravais lattice is characterized by having a triangular shape and its basis vectors are

$$\boldsymbol{a}_1 = a_g\left(\frac{1}{2}, \frac{\sqrt{3}}{2}\right) \tag{B.4}$$

and

$$\boldsymbol{a}_2 = a_g\left(-\frac{1}{2}, \frac{\sqrt{3}}{2}\right), \tag{B.5}$$

where graphene's lattice parameter is $a_g \simeq 2.46\text{Å}$. Each unit cell has two atoms, labeled as the A and B sites, and an area of $A_{\text{cell}} = \sqrt{3}a_g^2/2 \simeq 5.2\text{Å}^2$. Its first Brillouin zone (1BZ) has the shape of an hexagon (Fig. 34 b)) and the reciprocal lattice basis vectors are

$$\boldsymbol{b}_1 = \frac{4\pi}{\sqrt{3}a_g}\left(\frac{\sqrt{3}}{2}, \frac{1}{2}\right), \tag{B.6}$$

$$\boldsymbol{b}_1 = \frac{4\pi}{\sqrt{3}a_g}\left(\frac{\sqrt{3}}{2}, \frac{1}{2}\right). \tag{B.7}$$

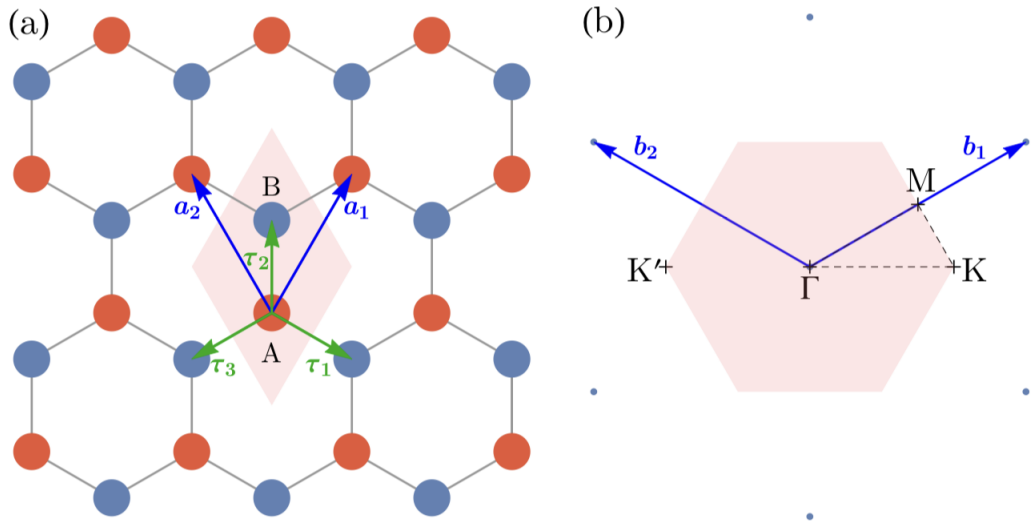


Figure 34: Graphene's crystalline structure and reciprocal lattice. (a) Graphene's crystalline structure. The unit cell is represented by the pink shaded rhombus and the A and B carbon sites are represented by the blue and red disks, respectively. The Bravais lattice basis vectors $\{\boldsymbol{a}_1, \boldsymbol{a}_2\}$ are represented by blue arrows and the nearest neighbours vectors $\boldsymbol{\tau}_a$ (with $a = 1, 2, 3$) are represented by green arrows. (b) Graphene's reciprocal lattice. The 1BZ is represented by the pink shaded hexagon. The reciprocal lattice basis vectors $\{\boldsymbol{b}_1, \boldsymbol{b}_2\}$ are represented by the blue arrows and the blue dots represent reciprocal lattice sites. The positions of the high symmetry points Γ, K, $K' = -K$ and M are also shown. (Reproduced with permission from the PhD thesis of Bruno Amorim [181])

B.1 In-plane wave-function

In order to obtain the wave-function of electrons in graphene, we employ a tight-binding (TB) model with nearest-neighbor (NN) interactions, which is proved to be an excellent approach since its electronic properties are dominated by the gapless linear dispersion relation around the corners of the 1BZ, with its low energy states (energetically closer to the Fermi level of neutral graphene) being located close to the $\boldsymbol{K}$ and $\boldsymbol{K}' = -\boldsymbol{K}$ points, with

$$\boldsymbol{K} = \frac{\boldsymbol{b}_1 - \boldsymbol{b}_2}{3} = \frac{4\pi}{3a_g}(1, 0)\,. \tag{B.8}$$

Using the TB approach, the second quantized Hamiltonian of graphene (which has very weak spin-orbit effects, thus neglecting spin) is then

$$H_{\text{gr}}^{\text{TB}} = -t \sum_{n,a} \left[\psi^\dagger_{\boldsymbol{R}_n, A} \psi_{\boldsymbol{R}_n + \boldsymbol{\tau}_a, B} + \psi^\dagger_{\boldsymbol{R}_n + \boldsymbol{\tau}_a, B} \psi_{\boldsymbol{R}_n, A} \right] \tag{B.9}$$

with $t \simeq 2.8$eV[23] being the nearest-neighbor hopping, $\psi^\dagger_{\boldsymbol{R}_n, A/B}$ $\left(\psi_{\boldsymbol{R}_n, A/B}\right)$ the creation (annihilation) operator for an electron located in the atom in the position $\boldsymbol{R}_n$ of the A/B sub-lattice.

The creation (annihilation) operators written as a Fourier expansion are

$$\psi^\dagger_{\boldsymbol{R}_n, A} = \frac{1}{\sqrt{N}} \sum_{\boldsymbol{k}} e^{-i\boldsymbol{k}\cdot\boldsymbol{R}_n} \psi^\dagger_{\boldsymbol{k}, A}, \tag{B.10}$$

$$\psi_{\boldsymbol{R}_n,A} = \frac{1}{\sqrt{N}} \sum_{\boldsymbol{k}} e^{i\boldsymbol{k}\cdot\boldsymbol{R}_n} \psi_{\boldsymbol{k},A}, \tag{B.11}$$

$$\psi^{\dagger}_{\boldsymbol{R}_n+\boldsymbol{\tau}_2,B} = \frac{1}{\sqrt{N}} \sum_{\boldsymbol{k}} e^{-i\boldsymbol{k}\cdot(\boldsymbol{R}_n+\boldsymbol{\tau}_2)} \psi^{\dagger}_{\boldsymbol{k},B}, \tag{B.12}$$

$$\psi_{\boldsymbol{R}_n+\boldsymbol{\tau}_2,B} = \frac{1}{\sqrt{N}} \sum_{\boldsymbol{k}} e^{i\boldsymbol{k}\cdot(\boldsymbol{R}_n+\boldsymbol{\tau}_2)} \psi_{\boldsymbol{k},B}, \tag{B.13}$$

with N being the number of unit cells in the crystal.

Thus, Eq.B.9 can be rewritten as

$$H^{\mathsf{TB}}_{\mathsf{gr}} = -t \sum_{\boldsymbol{k},a} \left[e^{i\boldsymbol{k}'\cdot\boldsymbol{\tau}_a} \psi^{\dagger}_{\boldsymbol{k},A} \psi_{\boldsymbol{k},B} + e^{-i\boldsymbol{k}\cdot\boldsymbol{\tau}_a} \psi^{\dagger}_{\boldsymbol{k},B} \psi_{\boldsymbol{k},A} \right], \tag{B.14}$$

By introducing the following vector

$$\boldsymbol{\psi}^{\dagger}_{\boldsymbol{k}} = \left[\psi^{\dagger}_{\boldsymbol{k},A}, \psi^{\dagger}_{\boldsymbol{k},B} \right], \tag{B.15}$$

with the positions encoding the sub-lattice, and introducing

$$\begin{aligned} \gamma_{\boldsymbol{k}} &= \sum_{a} e^{i\boldsymbol{k}\cdot\boldsymbol{\tau}_a} \\ &= |\gamma_{\boldsymbol{k}}| \, e^{i\theta(\boldsymbol{k})} \end{aligned} \tag{B.16}$$

with $\theta(\boldsymbol{k}) = \arg(\gamma_{\boldsymbol{k}})$, we can simplify the Hamiltonian in Eq.B.14 as

$$H^{\mathsf{TB}}_{\mathsf{gr}} = \sum_{\boldsymbol{k}} \boldsymbol{\psi}^{\dagger}_{\boldsymbol{k}} \cdot \boldsymbol{H}_{\boldsymbol{k}} \cdot \boldsymbol{\psi}_{\boldsymbol{k}} \tag{B.17}$$

where

$$\boldsymbol{H}_{\boldsymbol{k}} = \begin{bmatrix} 0 & -t\gamma_{\boldsymbol{k}} \\ -t\gamma^{*}_{\boldsymbol{k}} & 0 \end{bmatrix} \tag{B.18}$$

Notice that the dimension of this Hamiltonian comes from the fact that each unit cell has two carbon atoms, hence being a 2×2 matrix. Its spectrum, which is given by

$$\begin{aligned} \epsilon_{\boldsymbol{k},\lambda} &= \lambda t \, |\gamma_{\boldsymbol{k}}| \\ &= \lambda t \sqrt{3 + 2\cos(k_x a_g) + 4\cos\left(\frac{k_x a_g}{2}\right)\cos\left(\frac{\sqrt{3}k_y a_g}{2}\right)} \end{aligned} \tag{B.19}$$

has two bands, conduction and valence, corresponding to $\lambda = \pm 1$, and is plotted in Fig. 35.

If the graphene is not doped, only the valence band $(\lambda = -1)$ is occupied.

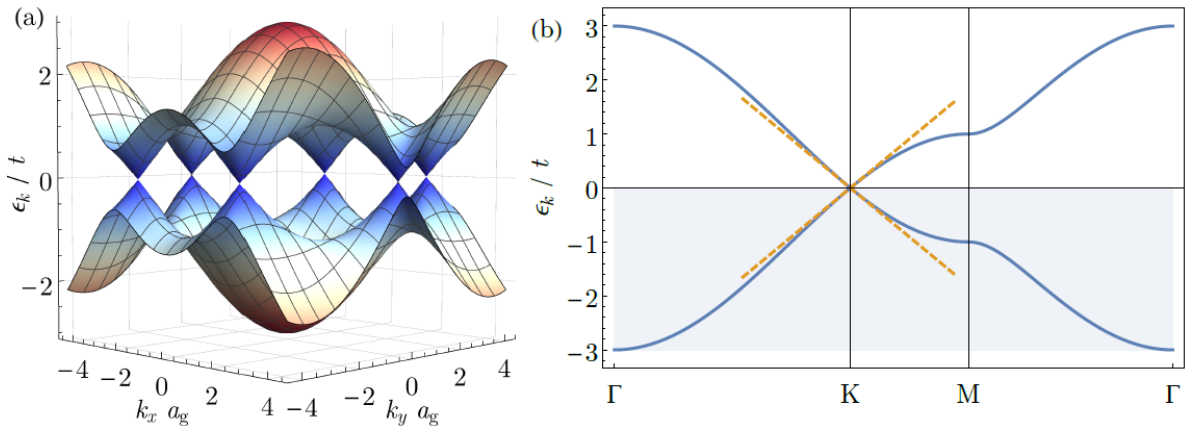


Figure 35: Electronic band structure of graphene. (a) 3D visualization of graphene dispersion relation. (b) Dispersion relation of graphene along the $\boldsymbol{\Gamma K M \Gamma}$ path represented in Fig. 34 (b). The dashed line represents the linearized dispersion relation around the $\boldsymbol{K}$ point. The shaded region represents the states that are occupied in neutral graphene. (Reproduced with permission from the PhD thesis of Bruno Amorim [181])

Finally, the eigenstates of the tight binding Hamiltonian in Eq.B.18 are then

$$\begin{aligned} \left|\chi_{\boldsymbol{k}}^{\lambda}\right\rangle &= \frac{1}{\sqrt{2}} \begin{bmatrix} 1 \\ \lambda \gamma_{\boldsymbol{k}}^{*} / \left|\gamma_{\boldsymbol{k}}\right| \end{bmatrix} \\ &= \frac{1}{\sqrt{2}} \begin{bmatrix} 1 \\ \lambda e^{i\theta(\boldsymbol{k})} \end{bmatrix} \end{aligned} \tag{B.20}$$

so that the full 2D wave-function for the electron's in graphene around the $\boldsymbol{K}$ points in a tight-binding approach is then

$$\left|\boldsymbol{k}, \lambda\right\rangle = \frac{1}{\sqrt{A_{\text{gr}}}} \sum_{n} \left|\chi_{\boldsymbol{k}}^{\lambda}\right\rangle e^{i\boldsymbol{k}\cdot\boldsymbol{R}_n} \tag{B.21}$$

with A_{gr} the area of the graphene sample.

B.2 Out-of-plane wave-function

Notice that the wave-vector $\boldsymbol{k}$ in Eq. B.21 is a 2D in-plane vector. In order to obtain the 3D eigenstates, we need to include a modulation factor $\phi(z)$ in the z direction, so that the 3D electronic eigenstates in graphene become

$$\begin{aligned} \left|\boldsymbol{K}\right\rangle &= \left|\boldsymbol{k}\right\rangle \left|\phi(z)\right\rangle \\ &= \frac{1}{\sqrt{A_{\text{gr}}}} \sum_{n} \left|\chi_{\boldsymbol{k}}\right\rangle e^{i\boldsymbol{k}\cdot\boldsymbol{R}_n} \left|\phi(z)\right\rangle \end{aligned} \tag{B.22}$$

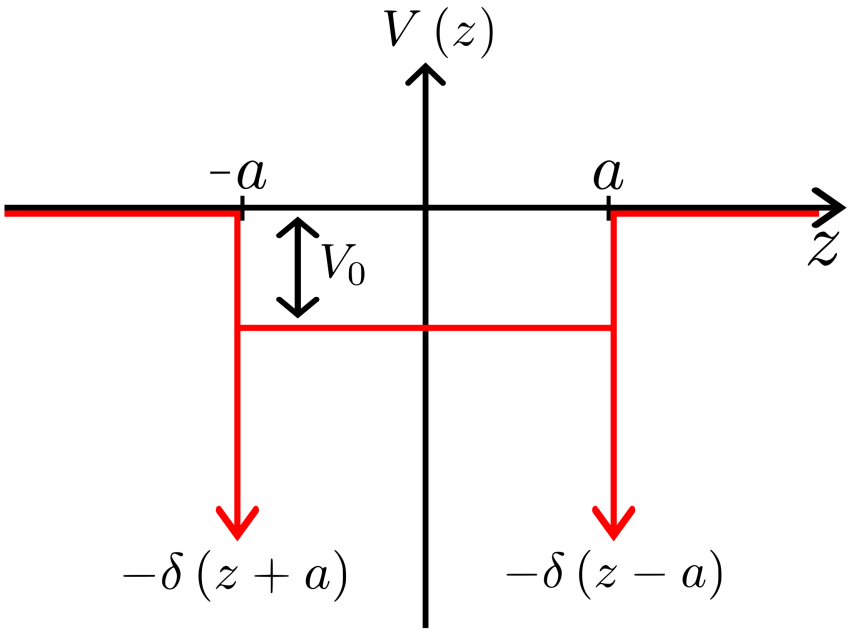


Figure 36: Electrostatic potential landscape in the z direction felt by the electrons in the gr-hBN-gr structure. The graphene sheets, located at $z = \pm a$ confine the electrons into the $x - y$ plane. Such confinement potential can be modeled as a Dirac delta function. In between the graphene sheets is placed a slab of hBN, which electrostatic potential is accounted by the introduction of V_0 in this region.

where we have dropped the notation λ for the bands, because in practice we will always assume that the valence band is completely filled, which means that the hopping electrons will be always in the conduction band $(\lambda = +1)$.

The electrons in graphene are confined to a very narrow region in the out-of-plane direction, about the size of a single atom, which for graphene is around $3\mathring{A}$ [182]. With such a small length, we can approximate the potential that confines the electrons in the z direction as a Dirac delta. Such potential landscape is depicted in Fig. 36.

The solution of the Schrödinger equation for such potential landscape in the region between the graphene sheets would be expressed as a hyperbolic cosine, which takes into account the overlap between the evanescent wave functions of each sheet. However, since the distance between the two graphene sheets is of the order of a few nanometers (much larger than the extension of the wavefunction), we can say that this overlap is week enough so that we can write the wave-function for each graphene as just the solution for a single Dirac delta, which is given as

$$|\phi(z)\rangle = \sqrt{\kappa} e^{-\kappa|z|}$$

with $\kappa = \sqrt{2mE/\hbar^2}$.

Therefore, we have

$$|\phi_L(z)\rangle = \begin{cases} \sqrt{\kappa_1} e^{\kappa_1 (z+a)}, & z < -a \\ \sqrt{\kappa_2} e^{-\kappa_2 (z+a)}, & z > -a \end{cases}$$

and

$$|\phi_R(z)\rangle = \begin{cases} \sqrt{\kappa_2} e^{\kappa_2 (z-a)}, & z < a \\ \sqrt{\kappa_1} e^{-\kappa_1 (z-a)}, & z > a \end{cases}$$

with $\kappa_1 = \sqrt{2mE_{\text{w}}/\hbar^2}$ where E_{w} is the extraction energy of graphene, which in the order of 4.3 eV [174], and $\kappa_2 = \sqrt{2m\left(E_{\text{w}} - V_0\right)/\hbar^2}$, where V_0 is taken to be the bottom of the conduction band of hBN. It can be experimentally measured (relative to vacuum) as the electron affinity, which was reported to be -0.5eV [183].

This work was supported by Fundação para a Ciência e a Tecnologia, I.P., (FCT-Portugal) thought project EXPL/FIS-MAC/0953/2021.